COMPARISON OF ROTOR INFLOW MODELS FOR FLIGHT SIMULATION FIDELITY

A THESIS SUBMITTED TO
THE GRADUATE SCHOOL OF NATURAL AND APPLIED SCIENCES
OF
MIDDLE EAST TECHNICAL UNIVERSITY

BY

FEYYAZ GÜNER

IN PARTIAL FULFILLMENT OF THE REQUIREMENTS
FOR
THE DEGREE OF MASTER OF SCIENCE
IN
AEROSPACE ENGINEERING

SEPTEMBER 2016

Approval of the thesis:

COMPARISON OF ROTOR INFLOW MODELS FOR FLIGHT SIMULATION FIDELITY

submitted by **FEYYAZ GÜNER** in partial fulfillment of the requirements for the degree of **Master of Science in Aerospace Engineering Department, Middle East Technical University** by,

Prof. Dr. Gülbin Dural Ünver _____
Dean, Graduate School of **Natural and Applied Sciences**

Prof. Dr. Ozan Tekinalp _____
Head of Department, **Aerospace Engineering**

Assoc. Prof. Dr. İlkay Yavrucuk _____
Supervisor, **Aerospace Engineering Department, METU**

Examining Committee Members:

Prof. Dr. Yusuf Özyörük
Aerospace Engineering Department, METU _____

Assoc. Prof. Dr. İlkay Yavrucuk
Aerospace Engineering Department, METU _____

Assoc. Prof. Dr. Eray Uzgören
Mechanical Engineering Program, METU NCC _____

Assist. Prof. Dr. Ali Türkey Kutay
Aerospace Engineering Department, METU _____

Assist. Prof. Dr. Nilay Sezer Uzol
Aerospace Engineering Department, METU _____

Date: _____

I hereby declare that all information in this document has been obtained and presented in accordance with academic rules and ethical conduct. I also declare that, as required by these rules and conduct, I have fully cited and referenced all material and results that are not original to this work.

Name, Last Name: FEYYAZ GÜNER

Signature :

ABSTRACT

COMPARISON OF ROTOR INFLOW MODELS FOR FLIGHT SIMULATION FIDELITY

Güner, Feyyaz

M.S., Department of Aerospace Engineering

Supervisor : Assoc. Prof. Dr. İlkay Yavrucuk

September 2016, 116 pages

In real-time rotorcraft simulations, there are various dynamic inflow models to chose from. Although dynamic inflow models are well documented in literature, a comparisons of them are not commonly available.

In this thesis, dynamic inflow models commonly used in flight simulators are, namely uniform inflow, extesion of uniform inflow with Payne's coefficients, Pitt-Peters inflow and Peters-He inflow model with higher harmonics, integrated to a well-known blade element model. A theoretical background for dynamic inflow models are given. Blade element model and trimming methods are explained. The considered dynamic inflow models are compared with three different sets of experimental data. First, computed induced flow field for tapered and rectangular blade configurations are compared with the measured inflow. Secondly, the effects of induced flow variation over the flapping dynamics is examined. Finally, the dynamic inflow models are compared in terms of steady-state performance predictions. In all comparisons, inflow distributions on the rotor disk are given and related observations are presented. The fidelity of the dynamic inflow models are summarized and recommendations are given.

Keywords: dynamic inflow, flight simulation fidelity, Pitt-Peters, Peters-He, uniform inflow, low advance ratio flapping, rotor performance

ÖZ

ROTOR İÇ-AKIŞ MODELLERİNİN UÇUŞ SİMÜLATÖRÜ DOĞRULUĞU İÇİN KARŞILAŞTIRILMASI

Güner, Feyyaz
Yüksek Lisans, Havacılık ve Uzay Mühendisliği Bölümü
Tez Yöneticisi : Doç. Dr. İlkay Yavrucuk

Eylül 2016 , 116 sayfa

Gerçek zamanlı döner kanat simülasyonlarında, seçim yapılabilecek birçok dinamik iç-akış modeli bulunmaktadır. Dinamik iç-akış modelleri literatürde iyi belgelenmesine karşın, modellerin karşılaştırılması genellikle mevcut değildir.

Bu tezde, uçuş simülatörlerinde yaygın olarak kullanılan eşdağılımlı iç-akış, Payne'nin katsayılarıyla genişletilmiş eşdağılımlı iç-akış, Pitt-Peters iç-akış ve yüksek harmonikli Peters-He iç-akış modelleri iyi bilinen bir pal elemanı modeline entegre edilmiştir. Dinamik iç-akış modellerinin dayandığı teorik altyapı verilmiştir. Pal elemanı modeli ve trim metodu açıklanmıştır. Dikkate alınan dinamik iç-akış modelleri üç farklı gruptaki deneylesel verilerle karşılaştırılmıştır. İlk olarak, konik ve diktörgen palli konfigurasyon için hesaplanan iç-akış alanı, deneysel iç-akış ölçümleriyle karşılaştırılmıştır. İkinci olarak, iç-akış varyasyonunun flaplama dinamiğine etkisi incelenmiştir. Son olarak, dinamik iç-akış modellerinin kararlı durumdaki performans tahminleri karşılaştırılmıştır. Tüm karşılaştırmalarda, rotor diski üzerindeki iç-akış dağılımı verilmiş ve ilgili gözlemler sunulmuştur. Dinamik iç-akış modellerinin doğruluğu özetlenmiş ve modellerin kullanımı için tavsiyeler verilmiştir.

Anahtar Kelimeler: dinamik iç-akış, uçuş simulasyonu doğruluğu, Pitt-Peters, Peters-He, eşdağılımlı iç-akış, düşük hız oranlı flaplama, rotor performansı

To my family

ACKNOWLEDGMENTS

I would like to express my heartfelt gratitude to my supervisor, Dr. İlkay Yavrucuk, for his guidance, support and encouragement during preparation of this thesis.

I would like thank my colleges and friends from Aerotim Engineering LLC, Dr. Gönenç Gürsoy, Onur Tarımcı, Mert Türkal, Serdar Üşenmez, Ercan Özgönül, Nil Ercan, Figen Kılıç, Emre Aksoy and Anıl Konaç, for providing an excellent working environment. I'm especially grateful to Dr. Gönenç Gürsoy for our thoughtful discussions over my thesis study.

I need to thank my friends, Abdullah Kaplan, Gökçe Kırbaş, Alican Aygün, Vahit Kurt, Ezgi Çabuk and Demet Cin for their long-lasting friendship. I also want to thank my friends in Ankara, Zeynep İlkay Bostancı, Barış Nasır, Nazlı Ece Ataoğlu and Ezgi Selin Akdemir for making my life enjoyable. I'm grateful to my home mate Buğra Can Babaoğlu for providing warm and relaxing environment in the home.

Special thanks to Diana Dermann and Zeynep İlkay Bostancı for reading and editing my thesis.

I would like to express my profound gratitude to my parents, Turgut and Nuran Güner, for their invaluable love and support throughout my life. I'm also grateful to my sisters, Tuğba, Seda, Eda, and brothers, Sergen & Alican Güner, for their continuous support and encouragement.

Lastly, I would like to express my sincere appreciation to my fiancée, Ezgi Melis Doğan for her unparalleled love, support and caring.

TABLE OF CONTENTS

LIST OF TABLES

TABLES

LIST OF FIGURES

FIGURES

NOMENCLATURE

Latin Symbols

$a,\ Cl_\alpha$	lift curve slope
A	rotor disk area, ft^2
c	blade chord, ft
C_L	roll moment coefficient
C_M	pitch moment coefficient
C_T	thrust coefficient
C_P	power coefficient
C_X	drag force coefficient, shaft axis
C_Y	side force coefficient, shaft axis
I_β	flapping inertia, $slug - ft^2$
k	effective radius gain
k_β	flapping spring constant
L'	sectional lift, N/m
L	influence coefficient matrix
$m,\ r$	harmonic number
$n,\ j$	polynomial number
M	apparent mass or time-filter matrix
p	non-dimensional rotating flapping frequency, $p = \sqrt{1 + \frac{k_\beta}{\Omega^2 I_\beta}}$
Q	number of rotor blades
R	rotor radius, ft
r	non-dimensional radial location of a blade element
$\bar{t}$	non-dimensional time, Ωt
V	flow parameter matrix
v_i	induced flow, ft/s
V_{climb}	climb velocity, $V_{climb} = -V_\infty sin(\alpha_s)$, ft/s
$V_{inplane}$	inplane velocity, $V_{inplane} = V_\infty cos(\alpha_s)$, ft/s
V_T	non-dimensional total average velocity passing the rotor

V_{tip}	tip speed, ΩR, ft/s
V_∞	freestream velocity, ft/s

Greek Symbols

$\alpha_j^r,\ \beta_j^r$	inflow coefficients
α	angle of attack, rad
α_s	shaft angle, positive aft of vertical
α_{tpp}	tip-path plane angle, positive aft of vertical
λ	total inflow divided by ΩR
λ_f	inflow due to freestream divided by ΩR
λ_i	induced flow divided by ΩR
μ	advance ratio defined in the experiments, $\mu = \frac{V_\infty}{\Omega R}$
μ_r	advance ratio defined in the inflow theories, $\mu_r = \frac{V_{inplane}}{\Omega R}$
Ω	rotor rotational speed, rad/s
ϕ_j^r	radial shape function
ψ	rotor azimuth angle
ρ	air density, $slug - ft^3$
σ	rotor solidity, $\sigma = \frac{Qc}{\pi R}$
χ	wake skew angle, $\chi = \frac{\pi}{2} - \tan^- 1(\mid \frac{\lambda}{\mu_r} \mid)$
X	wake skew function, $X = \tan(\mid \frac{\chi}{2} \mid)$
τ	inflow time constant
θ_0	collective pitch
θ_{1c}	lateral cyclic pitch
θ_{1s}	longitudinal cyclic pitch
θ	blade total pitch angle, $\theta = \theta_0 - \theta_{1c}\cos(\psi) - \theta_{1s}\sin(\psi)$
$\beta_0,\ a_0$	coning angle
$\beta_{1c},\ a_1$	longitudinal flapping angle
$\beta_{1s},\ b_1$	lateral flapping angle
β	total flapping angle, $\beta = \beta_0 - \beta_{1c}\cos(\psi) - \beta_{1s}\sin(\psi)$

Superscripts

$(\ )^c$	cosine element
$(\ )^s$	sine element
$(\ )'$	sectional element
$\dot{(\ )}$	derivative respect to time, $(\ )/dt$
$(\ )^*$	derivative respect to non-dimensional time, $(\ )/d\bar{t}$
$\bar{(\ )}$	non-dimensional quantity or reference parameter

Subscripts

$(\ )_0$	mean element
$(\ )_c$	cosine element
$(\ )_s$	sine element
$(\ )_q$	element of q^{th} blade
$(\ )_{aero}$	only related to aerodynamics

CHAPTER 1

INTRODUCTION

Real-time helicopter simulations are extensively used in pilot training. Building a real-time simulator is a challenge due to the complex aerodynamic flow around the helicopter. Especially the helicopter main rotor contributes the complex flow field. Theories such as free-wake, momentum, blade element-momentum and dynamic inflow are generally used in the calculation of the induced flow field in a rotor. In real-time simulations, usage of dynamic inflows theory is popular.

Helicopters are controlled by forces and moments mainly created at the rotor hub. Blade element rotor theory is coupled with a dynamic inflow theory to predict these forces and moments for given control inputs. When different dynamic inflow models with the same control inputs are used, predicted forces and moments exhibit differences. Therefore, the contribution of dynamic inflow models to the fidelity of the helicopter arises. In this thesis, some of the dynamic inflow models commonly used in flight simulators are compared with the wind tunnel tests and then, a fidelity assessments of the inflow models is given.

1.1 Literature Review

Dynamic inflow models represents the unsteady behaviour of air and incorporate its effect into the inflow models in a dynamic fashion. These dynamic wake models use rotor loads as forcing functions. These dynamic models introduce additional degrees of freedom to helicopter simulation. In dynamic inflow theory, rotor unsteady aerodynamics such as the wake and lift are treated separately [1]. Thus, various lift

models can be used in the calculation of the rotor aerodynamics forces. Dynamic inflow formulations are powerful tools in rotorcraft simulation due to its flexibility in choosing the lift model. Also, the state-space formulation of the dynamic inflow models allows both theoretical and empirical modifications to the simulation model.

A simple inflow is the uniform inflow model [2]. This inflow model is based on momentum theory. The uniform inflow is fairly good in hover calculations due to symmetry in the relative airspeeds seen by the local blade elements. In forward flight the symmetric flow conditions are no longer applicable. Thus, induced flow over the rotor disk becomes non-uniform. In order to improve the uniform inflow solution, Glauert [3] proposed a linear inflow distribution along the longitudinal axis for forward flight. Similar to Glauert's proposition, series of experiments on measuring the time-averaged-induced velocities on rotor disk were conducted by Brotherhood [4]. Using results from experiments, Brotherhood concluded that inflow distribution can be approximated as a linear function along the rotor longitudinal axis. In later years, linear distribution of the inflow was suggested by scientists such as Coleman [5], Dress [6] and Payne [7]. In these studies, the inflow distribution on the rotor is expressed as a function of static harmonic coefficients. Often, harmonic coefficients are related to the wake skew angle or/and advance ratio.

Although empirical formulation can represent the inflow distribution in steady-state flight, an accurate distribution in maneuvering flight requires dynamic inflow coefficients. Carpenter and Friedovich [8] monitored rapid change in the blade pitch and corresponding thrust response. From measurements, they established a physical relation between perturbed thrust and the unsteady flow of the air. According to Carpenter and Friedovich [8], the mean inflow and rotor thrust create inertia effects on the airflow, thus the settling time of the air is delayed. To have a dynamic representation, they introduced an apparent mass term into the blade element-momentum theory equation. This apparent mass term accounts the acceleration of the stagnant fluid.

Based on the classical momentum theory [3], Sissingh [9] worked on the instantaneous excitation of thrust and induced flow. He established induced flow and lift distributions on the rotor disk by using first harmonic sine and cosine terms of the Fourier series. Sissingh's model is instantaneous and does not consider the delay of

the induced flow after the perturbation. Thus, the induced flow model is a quasi-steady model.

Curtiss and Shupe [10] perturbed the rolling and pitching moments for the hingeless rotors. Using perturbation, an inflow model for hovering flight in quasi-steady form is achieved. In their model, Curtiss and Shupe modified the Lock number to include dynamic inflow effects into the calculation of rotor control derivatives. After Curtiss and Shupe, the equivalent Lock number and dynamic inflow models were compared with wind tunnel measurements by Banarjee et al. [11, 12]. Banarjee et al. concluded that the dynamic inflow model has better response when advance ratio is below 0.4 [11].

Work on the dynamic inflow models was continued by Ormiston and Peters [13] and they expressed the dynamic inflow model in state-space form. In the developed model, induced flow is distributed by Fourier series and lift is associated with this flow. The model has improved correlation with the hingeless rotor experiment. Although the dynamic inflow model uses a complex circulation theory, some elements of inflow gain matrices are constant or assumed to be zero. In this model, the wake skew and other flight parameters are not taken into the consideration and coupling effects between the variables are neglected.

Peters [14] extended the dynamic inflow model by including the apparent mass effects. In the development, curve fitting of the test data (empirical formulas) is used. In the model, differential forces on the rotor disk consist of two parts. One part is due to the acceleration of induced flow, the other part is due to change in the air flow which passes through the rotor. Although Peters's model shows good responses in hover, it is not appropriate for forward flight as a result of missing terms in inflow gain matrix. Peters's model has only diagonal elements, in other words, he neglected the coupling effects arising in forward flight.

Pitt and Peters [15, 16] extended dynamic inflow model for forward flight by using the actuator disk theory of Mangler [17]. Pitt and Peters' dynamic inflow model is an unsteady aerodynamic model which works in time domain. This dynamic inflow model is widely used in stability and control analysis applications and real-time simulations. In Pitt-Peters inflow model only low frequency aerodynamics are considered. Thus,

it is only a low-order approximation to the induced flow field. Considering only low frequencies is inadequate in the investigation of the higher frequency dynamics such as vibration, higher harmonic controls and aeroelastic applications. Consequently, a more general model is needed for higher frequency dynamics.

Using the solution of acceleration potential on elliptic domain, and assuming rotor has skewed cylindrical wakes, Peters and He [18, 19] developed a new inflow model which considers the higher frequency of wake dynamics. In previous models, inflow on the rotor disk was limited to only uniform inflow or first static harmonic coefficients. In this model, higher harmonics, hence, higher order dynamics (frequencies) are included. This new model is called Peters-He inflow model, and inflow states are calculated using first order differential equations. In this model, the blade lift is used as the forcing function in the equations. Also a complete closed form solution of the equations are derived. In this approach, inflow states are expressed azimuthally by Fourier series and radially by Legendre functions [18, 19].

Following the Peters-He model, Peters and Morillo [20, 21] developed an inflow model based on velocity potential (Galerkin approach) rather than the acceleration potential. Here, Peters-He model was extended to get a solution off the rotor disk.

1.2 Objective of the Thesis

This research is focused on the fidelity assessment of the dynamic inflow theories commonly used in flight simulators. Although each inflow model is well documented in literature, detailed comparison of the models is not common.

The rotor inflow has a major influence on the fidelity and accuracy of a main rotor model on a different inflow models have various characteristics. Some inflow models are more accurate in hover, yet they have comparably large errors in forward flight. In some conditions, simple inflow models exhibit relatively close results when compared with complex models. Moreover, some inflow models might provide better estimation in blade angle trim, while other models might predict better hub loadings.

In this thesis, dynamic inflow models are compared with various wind tunnel tests.

Firstly, estimated induced flow fields on the rotor disk are compared with an experimental flow fields [22, 23]. Secondly, the effects of the inflow distribution on low advance ratio flapping dynamics are investigated [24]. Finally, the S-76 helicopter's main rotor steady-state performance data is compared with the numerous inflow models [25].

In the thesis, dynamic uniform inflow, linearly distributed inflow with Payne's coefficients, Pitt-Peters inflow and Peters-He inflow model with higher harmonics are used. In Peters-He inflow model 3, 6, 10, 15 and 21 inflow states are selected.

1.3 Organization of this Thesis

In Chapter 1, literature review on dynamic inflow models are given. Pitt-Peters and Peters-He inflow models are reviewed. Also, some characteristic features of the dynamic inflow models are shown.

In Chapter 2, theory of the selected inflow models are explained. Here, the closed form of Pitt-Peters and Peters-He inflow equations are presented. In addition, the used of blade element rotor model and the trimming method are shown.

In Chapter 3, estimated induced flow fields on the rotor disk are compared with the wind tunnel measurements. In this chapter, inflow models are compared at the advance ratio of 0.15 with rectangular and tapered blade configurations. Predicted flow fields on the rotor are presented in the form of 3-D and contour plots. For some cases, induced flow variation along longitudinal and lateral axes are presented.

In Chapter 4, low advance ratio flapping dynamics are examined with inflow models in consideration. Change in the lateral flapping angle, longitudinal flapping angle and coning angle are provided for three set of experiments. In the wind tunnel tests, advance ratio, collective pitch angle and shaft tilt angle are treated as sweeping parameters.

In Chapter 5, steady-state performance data of the S-76 main rotor is compared with the studied inflow models. In both hover and forward flight tests, trimmed blade angles and power estimations are considered. In forward flight cases, hub drag and side

forces are additionally given. For some specific test points, inflow distribution and angle of attack distribution on the rotor disk are shown in terms of 3-D and contour plots.

In Chapter 6, presented results are summarized and important points are outlined. Finally, recommendations on future research are given.

CHAPTER 2

TECHNICAL BACKGROUND

In this chapter, theory behind the inflow models commonly used in flight simulations are presented. Formulation of the inflow starts with the basic uniform inflow theory. Then, uniform inflow is extended with linear coefficients to create an inflow distribution on the rotor disk. Subsequently, closed form of the Pitt-Peters inflow model and Generalized Dynamic Wake Theory (Peters-He) are explained. After the considered inflow models, blade element rotor model and trimming approach used in this thesis are given in the last two sections, respectively.

2.1 Dynamic Uniform Inflow

According to [2] and [3], thrust, T, is a function of uniform induced flow, v_i, and at the rotor hub, momentum theory thrust is given as follow:

$$T = 2\rho A|V_T|v_i \tag{2.1}$$

where, V_T represents the total average air velocity passing from the rotor disk. In equation (2.1), V_T depends on the v_i and relationship between v_i and V_T are given in equation (2.2).

$$|V_T| = \sqrt{V_{inplane}^2 + (v_i + V_{climb})^2} \tag{2.2}$$

Here, $V_{inplane}$ and V_{climb} are the inplane and climb velocities defined on the rotor plane, respectively. In the section of blade element rotor model, velocities required

by the inflow models are shown in Figure 2.2. In equation (2.1), T and v_i are unknowns, therefore V_T become also unknown due to its dependence on v_i. In order to solve equation (2.1), iterative schemes and root finding algorithms are introduced in [26, 27]. Generally, in these solution methods, blade element theory is used as a thrust source for momentum theory. The solution converges when blade element and momentum theory thrust or inflow values are matched.

When rotor is placed in a sphere and perturbed from its steady-state condition, some portion of the air in the sphere is accelerated [28]. Because of the unaccelerated air around the rotor, air-mass cannot settle down immediately. When this effect is introduced into the equation (2.1), inflow dynamics become unsteady and iterative solution can be avoided as,

$$T = 2\rho A|\boldsymbol{V_T}|v_i + \frac{4}{3}\pi(kR)^3\rho\dot{v_i} \tag{2.3}$$

where the acceleration of air is represented by the last term. In literature, this last term is known as apparent mass or time-lag filter term. In this equation, k represents the effective radius gain and it has a value between $0.74 - 0.86$ [28]. In this thesis, k is assumed as equal to 0.8. For convenience, equation (2.3) is put in a dimensionless form by normalizing it with $\rho A(\Omega R)^2$. Then, newly formed first order differential equation can be solved for derivative of non-dimensional inflow, λ_i. The new equation is established as follows:

$$\tau\dot{\lambda_i} = -2\frac{|\boldsymbol{V_T}|}{\Omega R}\lambda_i + C_T. \tag{2.4}$$

Here, time-lag filter, τ and derivative of induced flow, $\dot{\lambda_i}$, are given by,

$$\begin{aligned} \tau &= \frac{4}{3}k^3 \\ \dot{\lambda_i} &= \frac{\dot{v_i}}{\Omega^2 R} \end{aligned} \tag{2.5}$$

In equation (2.4), uniform inflow dynamics are defined by a first order differential

equation. In this equation, thrust coefficient, C_T, can be calculated using blade element theory [26, 27].

2.2 Extension of Uniform Inflow Theory with Glauert Coefficients

The uniform inflow at the rotor disk can be distributed along the longitudinal and lateral axes by adding static linear coefficients. At first, only longitudinal axis variation is taken into consideration [3]:

$$\lambda_i(\bar{r}, \psi) = \lambda_0(1 + k_c \bar{r} \cos\psi) \tag{2.6}$$

where, ψ and $\bar{r}$ are the azimuth angle and non-dimensional radial position of the rotor element, respectively. Here, distribution of induced flow in longitudinal axis is provided by k_c term. When variation along the lateral axis is concerned equation (2.6) can be extended by the similar approach. The following form can be used for this case,

$$\lambda_i(\bar{r}, \psi) = \lambda_0(1 + k_c \bar{r} \cos\psi + k_s \bar{r} \sin\psi) \tag{2.7}$$

Induced flow measurements are used for k_c and k_s correlations. Some of the k_c and k_s (based on empirical formulas) are given in [5, 6, 7]. Additionally, in [29] linear inflow coefficients, k_c and k_s, are well summarized. Table 2.1 presents the related coefficients [29].

In this thesis, Payne's k_c and k_s coefficients are selected. These coefficients are expressed as follows:

$$k_c = \frac{4/3 \tan(\chi)}{1.2 + \tan(\chi)} \qquad k_s = 0. \tag{2.8}$$

here, χ is called as the wake skew angle. When equations (2.7) and (2.8) are used, variation along the longitudinal and lateral axes can be obtained. The uniform inflow used in equation (2.7) is calculated from equation (2.4). In this thesis, linearly

distributed inflow model is named as *Payne's inflow model* due to selection of coefficients given in equation (2.8)

Table 2.1: First Harmonic Inflow Model Coefficients

Year	**Author(s)**	k_c	k_s
1945	Coleman et al.	$\tan(\chi/2)$	0
1949	Dress	$(4/3)(1-1.8\mu_r^2\tan(\chi/2)$	$-2\mu_r$
1959	Payne	$\frac{4/3\ \tan(\chi)}{1.2+\tan(\chi)}$	0
1979	Blake and White	$\sqrt{2}\sin(\chi)$	0
1981	Pitt and Peters	$(15\pi/32)\tan(\chi/2)$	0
1981	Howlett	$\sin^2(\chi)$	0

2.3 Pitt-Peters Inflow

The Pitt-Peters inflow model is constructed using actuator-disk theory and the model consists of both unsteady and quasi-steady parts. Unsteady part of the theory is included in the apparent mass term and this term is obtained from delayed reaction of the accelareted impermeable disk [30]. The quasi-steady part of the equation is related to solution of the pressure discontinuity at a circular disk [30].

According to [15, 16, 31], induced flow variation on the rotor disk can be shown as follows:

$$\lambda_i(\bar{r},\psi) = \lambda_0 + \lambda_s \bar{r}\sin\psi + \lambda_c \bar{r}\cos\psi \tag{2.9}$$

where, $\lambda_0,\ \lambda_s,\ \lambda_c$ are the inflow states. Here, $\bar{r}$ represents the non-dimensional radial location and ψ is the azimuth angle. Distribution defined in equation (2.9) is similar to the previous distribution given in equation (2.7). In the newly defined distribution, linear coefficients (k_c & k_s) are replaced with the λ_c, λ_s and they become new states of the equation (2.9). Through these states (λ_c and λ_s) a relation between inflow variation and aerodynamic hub moments is established.

In Pitt-Peters inflow model, states are obtained after solving a first order differential equation given in matrix form. Here, aerodynamic hub thrust, roll moment and pitch moment coefficients are used as forcing terms of dynamic equation. The governing equation of Pitt-Peters inflow is expressed as follow [15, 31]:

$$[M]\begin{Bmatrix}\lambda_0\\ \lambda_s\\ \lambda_c\end{Bmatrix}^{*} + [V][L]^{-1}\begin{Bmatrix}\lambda_0\\ \lambda_s\\ \lambda_c\end{Bmatrix} = \begin{Bmatrix}C_T\\ -C_L\\ -C_M\end{Bmatrix}_{aero} \tag{2.10}$$

where, M, V and L are known to be as mass (time filter), flow parameter and influence coefficient matrices of Pitt-Peters inflow model. These matrices are defined in [15, 31] and can be obtained from the following equations (2.11-2.15).

$$[M] = \frac{1}{\pi}\begin{bmatrix}\frac{128}{75} & 0 & 0\\ 0 & \frac{16}{45} & 0\\ 0 & 0 & \frac{16}{45}\end{bmatrix} \tag{2.11}$$

$$[V] = \begin{bmatrix}V_T & 0 & 0\\ 0 & V & 0\\ 0 & 0 & V\end{bmatrix} \tag{2.12}$$

$$[L] = \begin{bmatrix}0.5 & 0 & -\frac{15}{64}\pi\sqrt{\frac{1-sin\alpha^*}{1+sin\alpha^*}}\\ 0 & \frac{4}{1+sin\alpha^*} & 0\\ \frac{15}{64}\pi\sqrt{\frac{1-sin\alpha^*}{1+sin\alpha^*}} & 0 & \frac{4sin\alpha^*}{1+sin\alpha^*}\end{bmatrix} \tag{2.13}$$

where, the parameters α^*, V_T and V are defined as,

$$\begin{aligned}\alpha^* &= tan^{-1}\frac{|\lambda|}{\mu_r}\\ V_T &= \sqrt{\mu_r^2+\lambda^2}\\ V &= \frac{\mu_r^2+(\lambda+\lambda_0)\lambda}{V_T}\\ \lambda &= \lambda_0+\lambda_f\end{aligned} \tag{2.14}$$

where, μ_r is expressed as,

$$\mu_r = \frac{V_{inplane}}{\Omega R} \tag{2.15}$$

Forcing terms of the Pitt-Peters inflow model are the aerodynamic thrust (C_T), roll moment (C_L) and pitch moment (C_M) coefficients. In the model, these terms are defined on a reference frame placed at the rotor center [31]. Following [15], forcing terms (C_T, C_L, C_M) of Pitt-Peters inflow model can be calculated:

$$\begin{aligned} C_T &= \frac{1}{\rho\pi\Omega^2 R^4} \int_0^{2\pi} \int_0^R L' dr d\psi \\ C_L &= -\frac{1}{\rho\pi\Omega^2 R^5} \int_0^{2\pi} \int_0^R L' r \sin(\psi) dr d\psi \\ C_M &= -\frac{1}{\rho\pi\Omega^2 R^5} \int_0^{2\pi} \int_0^R L' r \cos(\psi) dr d\psi \end{aligned} \tag{2.16}$$

In equation (2.16), L' represents the sectional blade lift.

2.4 Generalized Dynamic Wake Theory (Peters-He)

The Generalized Dynamic Wake Theory (Peters-He) is established by solving the potential flow equation in elliptic domain. In this theory, induced flow on the rotor plane is azimuthally expressed by Fourier series and radially by Legendre functions. In the Peters-He inflow model, inflow states are generalized and higher inflow states can be added to the model by a systematic approach. Therefore, it is of often considered an extension of Pitt-Peters inflow model. This inflow model implicitly includes dynamic inflow theory, Theodersen theory and the Prandtl/Goldstein static inflow distribution [18]. The forcing functions of the model are the radial integrals of the blade loadings.

In this thesis, the closed form of the Peters-He inflow model is summarized. Derivation of the theory is given in [18, 19]. Closed form Peters-He inflow equations are in

the form of state-space matrix equation, which makes it suitable for real-time simulations. This form also allows modifications such as vortex ring state, ground effect, wake distortion, etc.

In Peters-He inflow model [18, 19], induced flow on the rotor disk is expressed in the following general form:

$$\lambda_i(\bar{r},\psi,\bar{t}) = \sum_{r=0}^{\infty}\sum_{j=r+z}^{\infty} \phi_j^r(\bar{r})[\alpha_j^r(\bar{t})\cos(r\psi) + \beta_j^r(\bar{t})\sin(r\psi)], \quad z = 1,3,5,... \tag{2.17}$$

where, α_j^r and β_j^r are the inflow expansion coefficients. Here, ϕ_j^r represents the radial shape function for a given harmonic number, r, and order of the polynomial, j. For any harmonic and polynomial number, the radial shape function, ϕ_j^r, depends on factorial ratios, H_j^r and they are given in the following equations (2.18 & 2.19).

$$\phi_j^r(\bar{r}) = \sqrt{(2j+1)H_j^r} \sum_{q=r,r+2,...}^{j-1} \bar{r}^q \frac{(-1)^{\frac{q-r}{2}}(j+q)!!}{(q-r)!!(q+r)!!(j-q-1)!!} \tag{2.18}$$

$$H_j^r = \frac{(j+r-1)!!(j-r-1)!!}{(j+r)!!(j-r)!!}. \tag{2.19}$$

Here, double factorials are defined as follow:

$$n!! = \begin{cases} n(n-2)(n-4)....3.1 & \text{if } n \text{ is odd} \\ n(n-2)(n-4)....2 & \text{if } n \text{ is even} \\ 1 & \text{if } n \text{ is equal to } 0 \\ 1 & \text{if } n \text{ is equal to } -1 \\ -1 & \text{if } n \text{ is equal to } -3 \end{cases}$$

In Peters-He inflow model, the governing equation is expressed as a first order differential matrix equation [18, 19]. In this model, the cosine and sine part of the inflow

model is decoupled. Thus, they can be treated as two independent equations.

$$[M^c]\{\alpha_j^r\}^* + [\tilde{L}^c]^{-1}[V^c]\{\alpha_j^r\} = \frac{1}{2}\{\tau_j^{rc}\}. \tag{2.20}$$

$$[M^s]\{\beta_j^r\}^* + [\tilde{L}^s]^{-1}[V^s]\{\beta_j^r\} = \frac{1}{2}\{\tau_j^{rs}\} \tag{2.21}$$

where, (M^c, M^s), (V^c, V^s) and ($\tilde{L}^c$, $\tilde{L}^s$) are apparent mass, mass flow parameter, and inflow gain matrices, respectively. Calculation of these matrices are given in the following equations (2.22 - 2.27).

Apparent mass matrix is a purely diagonal matrix which shows no coupling between the states. Sine and cosine mass matrices are identical except when $r = 0$. In this case, sine term vanishes ($\sin(0) = 0$).

$$[M]^{c,s} = \frac{2}{\pi}\begin{bmatrix} \ddots & & \\ & H_j^r & \\ & & \ddots \end{bmatrix} \tag{2.22}$$

In Peters-He inflow model, calculation of flow parameter matrix is similar to the one defined in Pitt-Peters model. Likewise the mass matrix; cosine and sine parts of the flow parameter matrix is equal unless $r = 0$. In flow paramer matrix, when $r = 0$ and $j = 1$, V_1^0 become equal to V_T. For any other r and j, elements of V_j^r become equivalent to V.

$$[V]^{c,s} = \begin{bmatrix} \ddots & & \\ & V_j^r & \\ & & \ddots \end{bmatrix} \tag{2.23}$$

$$\begin{aligned} V_T &= \sqrt{\mu_r^2 + \lambda^2} \\ V &= \frac{\mu_r^2 + (\lambda + \lambda_m)\lambda}{V_T} \\ \lambda &= \lambda_m + \lambda_f \end{aligned} \tag{2.24}$$

where, λ_m is the mean inflow of the Peters-He inflow model. When $\lambda_m = \sqrt{3}\alpha_1^0$ is used as mean inflow, coupling between α_1^0 and V_T make the theory non-linear [18].

Inflow gain matrix, L, depends on the wake skew angle. This dependence varies according to polynomial number, r, cosine and sine part of the matrix.

$$\begin{aligned}
[\tilde{L_{jn}^{0m}}]^c &= X^m[\Gamma_{jn}^{0m}] \quad \text{if } r = 0 \\
[\tilde{L_{jn}^{rm}}]^c &= [X^{|m-r|} + (-1)^l X^{|m+r|}][\Gamma_{jn}^{rm}] \quad \text{if } r \neq 0 \\
[\tilde{L_{jn}^{rm}}]^s &= [X^{|m-r|} - (-1)^l X^{|m+r|}][\Gamma_{jn}^{rm}] \quad \text{if } r \neq 0
\end{aligned} \tag{2.25}$$

where, l and X are defined as follows:

$$\begin{aligned}
l &= min(r, m) \\
X &= \tan(|\ \frac{\chi}{2}\ |) \\
\chi &= \frac{\pi}{2} - \tan^- 1(|\ \frac{\lambda}{\mu_r}\ |)
\end{aligned} \tag{2.26}$$

Finally, Γ elements of L matrix are given in the next equation.

$$\begin{aligned}
[T_{jn}^{rm}] = \frac{(-1)^{\frac{n+j-2r}{2}}}{\sqrt{H_m^n H_r^j}} \frac{2\sqrt{(2n+1)(2j+1)}}{(j+n)(j+n+2)[(j-n)^2-1]} \quad &\text{if } r+m \text{ is even} \\
[T_{jn}^{rm}] = \frac{\pi}{2\sqrt{H_m^n H_r^j}} \frac{sign(r-m)}{\sqrt{(2n+1)(2j+1)}} \quad &\text{if } r+m \text{ is odd, } |j-n| = 1 \\
[T_{jn}^{rm}] = 0 \quad &\text{if } r+m \text{ is odd, } |j-n| \neq 1
\end{aligned} \tag{2.27}$$

Forcing terms in the governing equations (2.20, 2.21), (τ_j^{0c}, τ_j^{rc}, τ_j^{rs}) relate blade lift to the pressure coefficients through radial shape functions. Pressure coefficients can

be expressed as [19]:

$$\begin{aligned}
\tau_j^{0c} &= \frac{1}{2\pi}\sum_{q=1}^{Q}[\int_0^1 \frac{L'_q}{\rho\Omega^2 R^3}\phi_j^0(\bar{r})d\bar{r}] \\
\tau_j^{rc} &= \frac{1}{\pi}\sum_{q=1}^{Q}[\int_0^1 \frac{L'_q}{\rho\Omega^2 R^3}\phi_j^r(\bar{r})d\bar{r}]\cos(r\psi_q) \\
\tau_j^{rs} &= \frac{1}{\pi}\sum_{q=1}^{Q}[\int_0^1 \frac{L'_q}{\rho\Omega^2 R^3}\phi_j^r(\bar{r})d\bar{r}]\sin(r\psi_q)
\end{aligned} \tag{2.28}$$

Here, L'_q represents blade sectional lift of the q^{th} blade. In Peters-He inflow theory, inflow and blade lift are individually treated, thus any blade lift theory can be integrated to the model. Throughout the thesis, lifting line theory is applied in the calculation of blade lift.

In this thesis, equation (2.17) is expanded to obtain 3, 6, 10, 15 and 21 inflow states. The expansion is performed using the table given in [19]. Using the table, the maximum required indices of the parameters, r and j, hence, inflow models with desired number of states are obtained.

2.5 Blade Element Rotor Model

The blade element rotor model used in this thesis is based on [32]. This well-known rotor model is commonly used in real-time flight simulators. Here, the default inflow model is replaced by the inflow models explained in the previous sections. Coupling between dynamic inflow models and blade dynamics [18] are expressed in the Figure 2.1.

In blade element theory, the rotor blade is discretized into differential elements radially and azimuthally on the rotor plane with a number of virtual blades. Selection of the virtual blade number depends on parameters such as rotor rotational speed, simulation step-size and magnitude of the numerical oscillations, etc. There should be enough virtual blades number to allow the main rotor to represent the dynamics of the main rotor flapping.

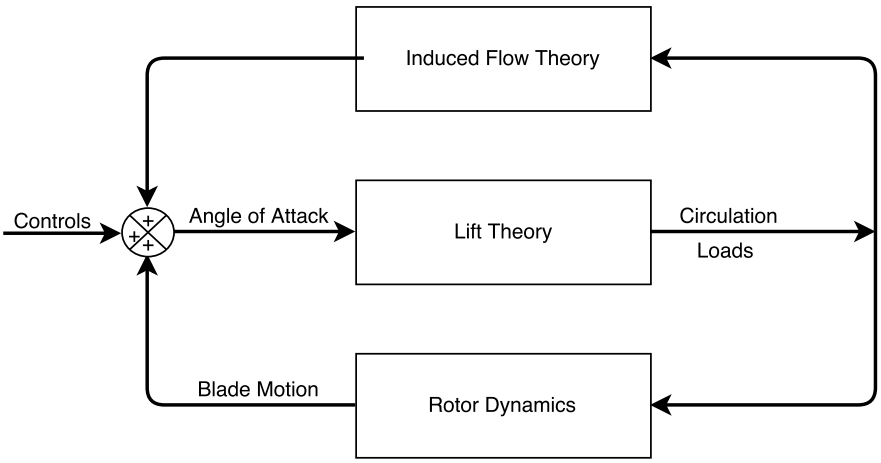

Figure 2.1: Relation between Dynamic Inflow and Rotor Dynamics

This blade element main rotor code uses detailed rotor parameters and geometry information. The model takes rotational speed, blade number, radius, twist, mass, chord and flapping inertia as input. It also uses hinge offset, hub spring, pitch-flap coupling angle and pre-cone angle when available. In order to increase fidelity, blade twist and chord geometries can be given in the form of look up tables. These tables are created as a function of non-dimensional radial blade location.

The inflow has a complex distribution on the rotor disk and it changes the angle of attack of the blade element on the rotor disk. Because of this change, the calculated differential forces and moments at the given location also changes. Thus, induced flow distribution plays important role in the estimation of the rotor forces and moments.

The collective motion is directly related to the loading on the blade, which causes the coning. Cyclic movements change the flapping angles to adjust the load distribution on the hub. Therefore, the solution of the flapping dynamics plays a major role in helicopter's steady-state performance and its transient response. The flapping angle acceleration is expressed in terms of a second order differential equation and this equation consists of aerodynamic and inertial forces. The flapping rate and flapping angle are found by integration. The integration of this equation is a major challenge since the rotor flapping dynamics is much faster than the total helicopter dynamics. The method for the integration technique can be found at [32].

In the blade element main rotor code, the net air velocity vector are calculated at every azimuth angle and radial location (all elements in the hub). The net perpendicular velocity of the blade element is used in the calculation of the corresponding (local) angle of attack. The net perpendicular velocity consists of a free-stream velocity component, induced flow contribution and velocity created by the flapping motion. After attaining angle of attack; lift and drag coefficients are determined from 2-D look up tables, which are functions of angle of attack and Mach number when available. Then, sectional lift and drag forces are calculated at the considered blade element. In the force calculation, tip loss is neglected. Also, reverse flow region is not included in the model whenever a linear lift curve slope is used instead of lookup tables. In reverse flow region, while angle of attack is high, the dynamic pressure seen by the blade is low. Thus, overall force contribution is small and can be neglected. According to [33], the reverse flow effects can be ignored when advance ratio is below 0.5.

In this thesis, isolated blade element rotor models with different inflow theories are investigated. In the calculations of the induced flow theories, some velocities are defined such as climb and inplane. Figure 2.2 presents these velocities and related coordinate system. Free-stream velocity, V_∞ and advance ratio, μ, are aligned with a reference line. Shaft tilt angle, α_S, is defined positive to aft of the vertical line. In Figure 2.2, shaft is tilted forward; thus has a negative value. Since free-stream velocity is parallel to the reference line, velocities parallel ($V_{inplane}$, μ_r) and perpendicular (V_{climb}, λ_f) to rotor (hub) plane can be calculated as follow:

$$\begin{aligned} V_{inplane} &= V_\infty cos(\alpha_s) \qquad \mu_r = \frac{V_{inplane}}{\Omega R} \\ V_{climb} &= -V_\infty sin(\alpha_s) \qquad \lambda_f = \frac{V_{climb}}{\Omega R} \end{aligned} \tag{2.29}$$

In the inflow theories, induced flow (v_i, λ_0, λ_m or λ_i) is defined perpendicular to the rotor plane and it has a positive value when flow is towards the negative z-axis direction. In blade element rotor model, angle of attack is calculated at the local blade element which has a flapping motion. Therefore, induced flow is transformed to the flapped blade frame and the component of the inflow perpendicular to local blade element is used in the calculation of angle of attack.

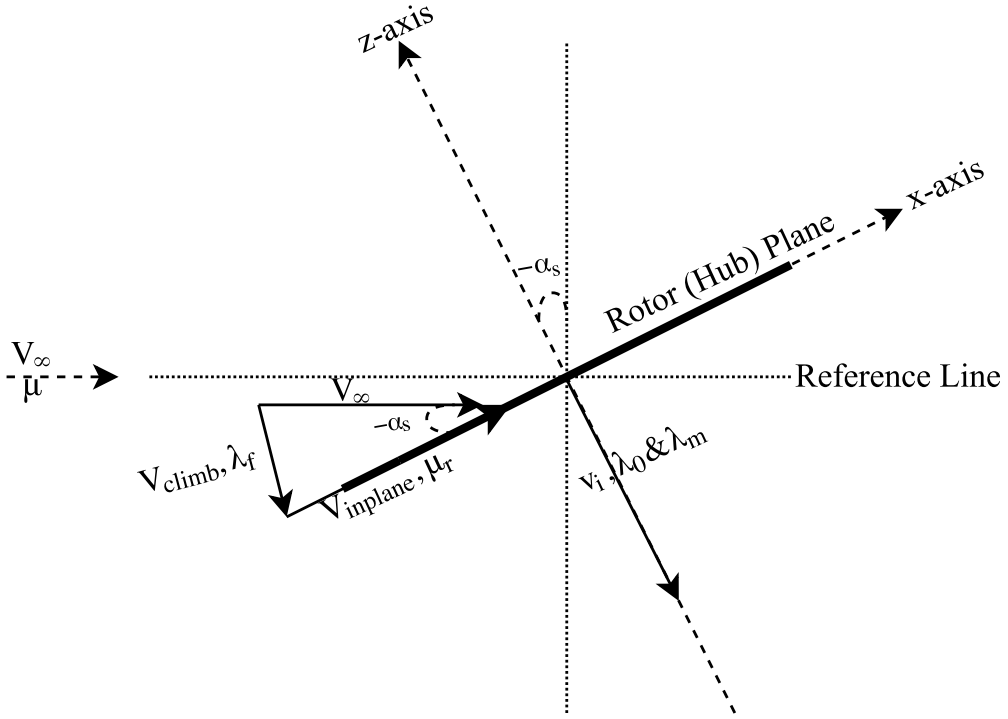

Figure 2.2: Velocities on a Rotor Plane

2.6 Trim using an Automatic Controller

The helicopter rotors are tested in the wind tunnel [22, 23, 24, 25] at various conditions. In order to do comparisons with the experimental data, simulations must be trimmed to appropriate test conditions. In this thesis, models are trimmed with the auto-pilot algorithm [1, 34]. Figure 2.3 shows the implementation of the trim scheme.

In this trim scheme, blade cyclic inputs are connected to rotor hub thrust and moments or first harmonic flapping angles through a second order differential matrix equation. Thus, when experimental hub thrust ($\bar{C}_T$), roll ($\bar{C}_L$) and pitch moment ($\bar{C}_M$) values are known, corresponding blade inputs (θ_0, θ_{1s}, θ_{1c}) can be found by integrating the differential equation. The trimming algorithm block in Figure 2.3 has the following differential equation [1]:

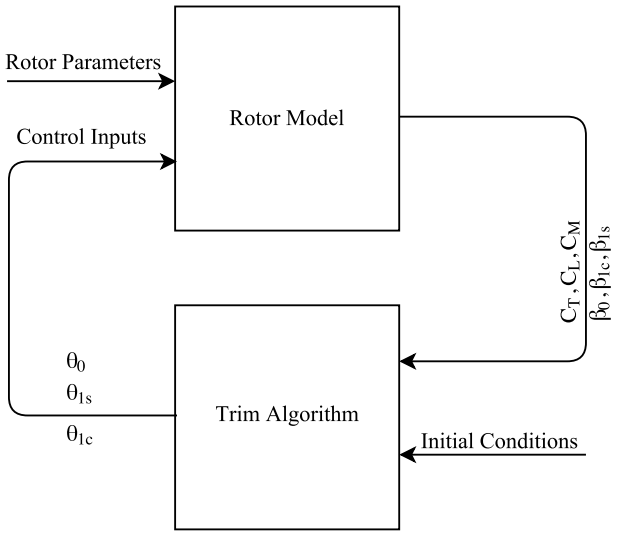

Figure 2.3: Schematic of the Trim Method

$$\begin{bmatrix} \tau_0 & 0 & 0 \\ 0 & \tau_1 & 0 \\ 0 & 0 & \tau_1 \end{bmatrix} \left\{ \begin{array}{c} \theta_0 \\ \theta_{1s} \\ \theta_{1c} \end{array} \right\}^{**} + \left\{ \begin{array}{c} \theta_0 \\ \theta_{1s} \\ \theta_{1c} \end{array} \right\}^{*} = \\ \begin{bmatrix} K_0 & 0 & 0 \\ 0 & K_1 & 0 \\ 0 & 0 & K_1 \end{bmatrix} \begin{bmatrix} \frac{6}{a\sigma} & 0 & 0 \\ 0 & -\frac{16}{a\sigma} & \frac{2\gamma}{a\sigma(p^2-1)} \\ 0 & -\frac{2\gamma}{a\sigma(p^2-1)} & -\frac{16}{a\sigma} \end{bmatrix} \left\{ \begin{array}{c} \bar{C_T} - C_T \\ \bar{C_L} - C_L \\ \bar{C_M} - C_M \end{array} \right\} \tag{2.30}$$

where, τ_0 and τ_1 are the time constants for the collective and cyclic channels, respectively. Parameters, K_0 and K_1 represent the collective and cyclic pitch gains. Typical values for the time constants (τ_0, τ_1) and cyclic gains (K_0, K_1) are given in the [1, 34]. In equation (2.30), a stands for the lift curve slope, σ is the solidity, p is non-dimensional rotating frequency and γ represents the Lock number. The superscript bar, ($\bar{}$), shows the reference parameters where the model is to be trimmed.

In equation (2.30), the far right term at the right hand side defines the errors between the desired hub loadings and simulation outputs. For robustness of the solution, time filter constants are introduced for the non-dimensional second derivatives of the control inputs [34]. In order to find converged control inputs, equation (2.30) is integrated in time. The initial conditions of $[\theta_0\ \theta_{1s}\ \theta_{1c}]^*$ and $[\theta_0\ \theta_{1s}\ \theta_{1c}]$ are taken as zero vectors. Rotor parameters can be initialized to any meaningful values. For Pitt-Peters inflow

model, typical convergence of the control inputs are given in Figure 2.4 and errors are presented in Figure 2.5.

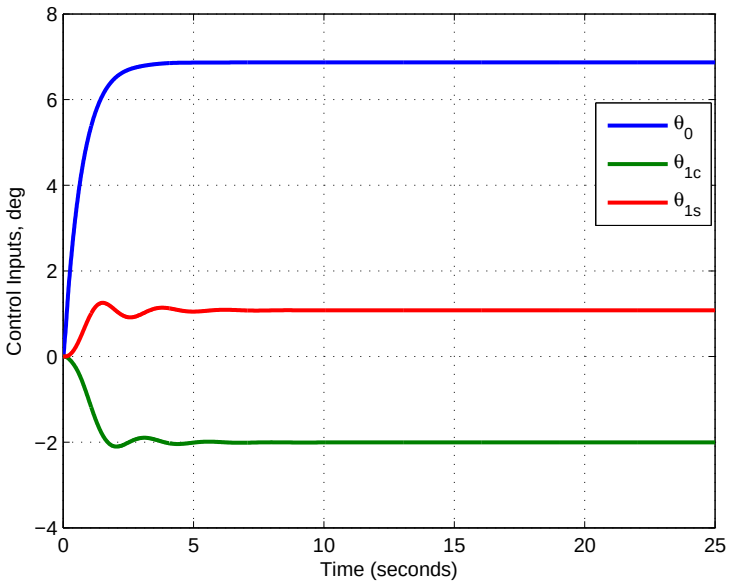

Figure 2.4: Convergence of the Control Inputs

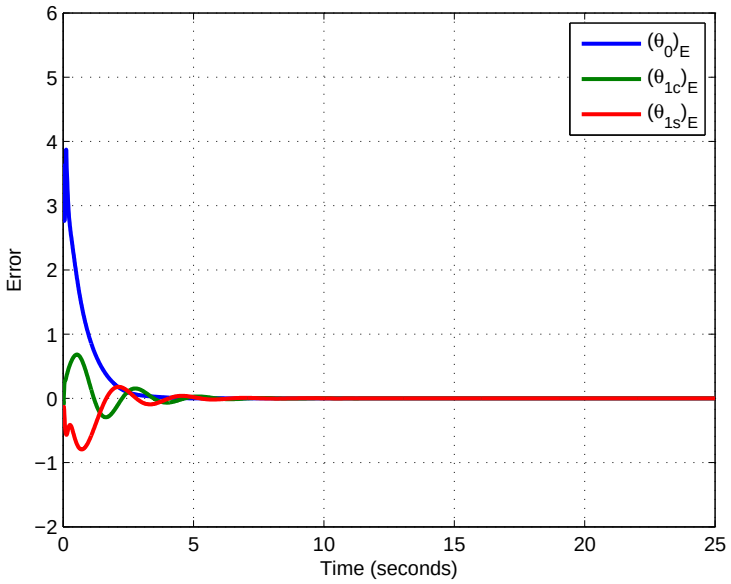

Figure 2.5: Error of the Control Inputs

When flapping angles are used instead of thrust and moments, some part of the equation is changed. The new trimming algorithm for this case is expressed in [1].

CHAPTER 3

COMPARISON OF INFLOW THEORIES

3.1 Introduction

In this chapter, induced flow field estimation of considered inflow models are compared with the experimental measurements [22, 23]. In literature, higher state Peters-He models are already validated [1, 18, 19]. Here, inflow models used in flight simulations (models with relatively less states) are compared with the experimental flow field. Also, by analysing the flow field, accuracy of the blade element code is double checked.

In this chapter, induced flow measurement and implementation of the theories are described. Then, theoretical flow field computations are compared when advance ratio is equal 0.15. In the comparison, both rectangular blade and tapered blade configurations are used and predictions are given in the form of 3-D and contour plots. Moreover, inflow along the longitudinal and lateral axes are presented.

3.2 Induced Flow Measurement

Induced inflow experiments [22, 23] are conducted in NASA Langley Research Center to measure induced flow on the rotor disk, in various forward flight conditions. Measurements are taken one chord above from the rotor tip path plane using the Laser Velocimeter technique. In experiments, measurements are taken in time-accurate and time-averaged form. In the experiment, sensors are placed at 9 azimuthal positions ($\psi = 0, 30, 60, 90, 150, 180, 210, 240, 330$ degrees) and 15 radial blade loca-

tions. Measurements inherently include the interaction with the fuselage.

In this thesis, time-averaged induced flow data is selected in the comparison of theoretical induced flow predictions. Series of experiments are considered at advance ratio of 0.15 and 0.23 with two blade configuration (rectangular & tapered blades). In this thesis, experiments at advance ratio 0.15 with rectangular and tapered blades are concerned. Experiments are carried out such a way that tip path plane of the rotor is held constant at $-3°$, likewise shaft angle is arranged to $-3°$ to make flapping angles, β_{1c} and β_{1s}, equal to zero. Also, steady-state thrust coefficient is set to 0.0064 during the experiments.

3.3 Implementation

The isolated rotor model explained in Chapter 2 is configured according the rotor parameters given in Table 3.1. Model compares time-averaged induced inflow data rather than time-instantaneous ones. Although the resized test rotor has exceptionally fast dynamics (rotational speed is high), model provide enough robustness in the both flapping and inflow dynamics. In this chapter, the isolated rotor model has 64 azimuthal and 100 radial positions. Also, the model takes into account the root cut-out and hinge offset location when defining the blade geometry. Shape of the used rectangular and tapered blades are shown at Appendix A. For comparison, the isolated rotor models must have the same conditions with the experiment for each inflow model. The isolated rotor model is trimmed using the method explained in Chapter 2.

Isolated rotor model is constructed with the following assumptions:

- Angle of attack is small, linear lift curve slope is used
- Reverse flow region is not modelled
- Elasticity of the blade is neglected
- Flow is incompressible and inviscid
- Lag and feathering dynamics are not considered
- Fuselage interaction on the rotor is neglected

- Hub drag is not considered

Table 3.1: Rotor Parameters used in Model

Parameter	**Rectangular**	**Tapered**
Number of blades	4	4
Airfoil	NACA 0012, $Cl_\alpha = 5.73$	NACA 0012, $Cl_\alpha = 5.73$
Hinge offset, in	2.0	2.0
Root cutout, in	8.25	8.25
δ_3, deg	0.0	0.0
Linear twist, deg	-8.0	-13.0
Radius, in	33.88	32.5
Root chord, in	2.6	3.2
Taper ratio	-	3:1 to 0.75R
Solidity	0.0977	0.0977
Blade weight, grams	259.3	222.0
Shaft tilt, deg	-3.0	-3.0
$\bar{C_T}$	0.0064	0.0064
V_∞, knots	55.4	55.7
V_{tip}, ft/s	624.3	624.0

3.4 Simulation Results and Discussion

3.4.1 Rectangular Blade

In this case, induced inflow at each 64 azimuth and 100 radial positions are calculated and saved until the desired steady-state condition is reached. This data on the rotor disk is shown as 3-D and 2-D (contour) plots. In addition, induced flow along longitudinal axis and lateral axis are presented.

3.4.1.1 3-D Plots

In this section, visualization in 3-D is employed. In uniform inflow theory (Figure 3.1(a)), a disk parallel on the rotor plane is constructed and it does not show any variation. Starting with Payne's inflow model, Pitt-Peters and Peters-He 3-State inflow models have linear variation and magnitude of the flows are biased towards aft

of the rotor. Although Pitt-Peters and Payne models show similar linear variation, Peters-He 3-State inflow model exhibit comparably larger variation (Figure 3.1(d)). Figure 3.2 presents non-linear inflow distribution on the rotor plane. Peters-He 6-state inflow model anticipates greater induced flow values near the blade tip. From Figures 3.2(b) and 3.2(c), it is seen that Peters-He 15 & 21-State inflow models show the most resemblance with the measured flow field. Yet, Peters-He 15 & 21-State models still have discrepancy near the blade tip. According to [18, 19], this discrepancy is alleviated when inflow state is increased to higher values.

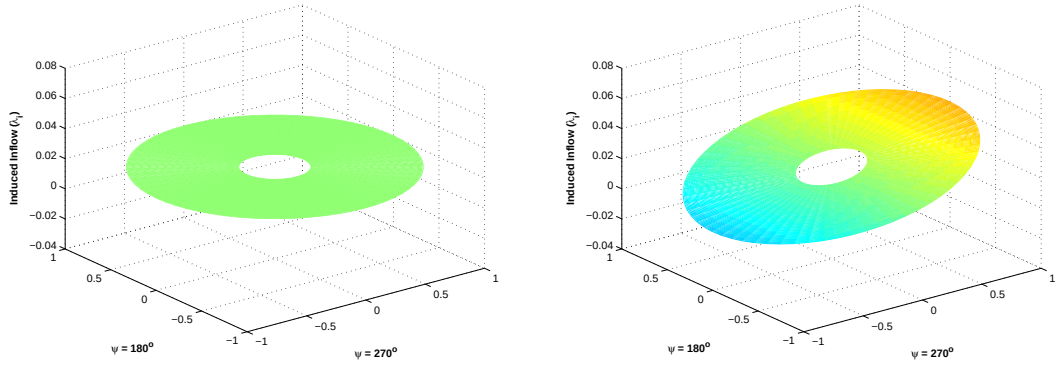

(a) Dynamic Uniform Induced Flow

(b) Payne Induced Flow

(c) Pitt-Peters Induced Flow

(d) Pe-He 3-State Induced Flow

Figure 3.1: Uniform, Payne, Pitt-Peters and Peters-He 3-State Induced Flow 3-D Plots, Rectangular Blade, $\mu = 0.15$

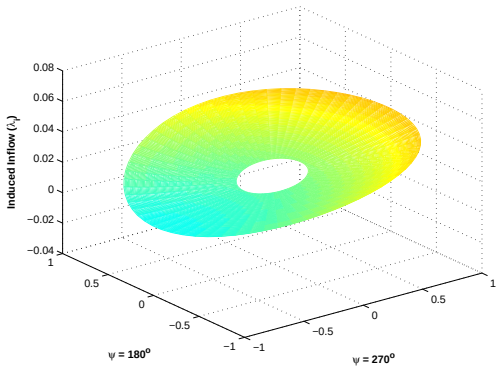

(a) Peters-He 6-State Induced Flow

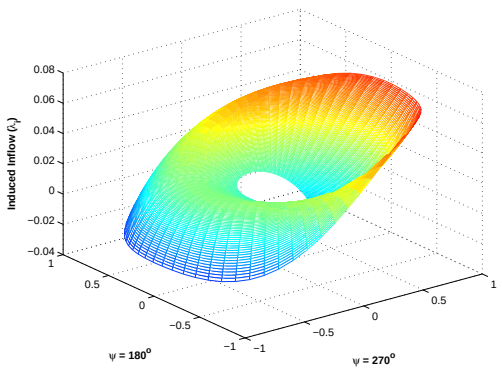

(b) Peters-He 15-State Induced Flow

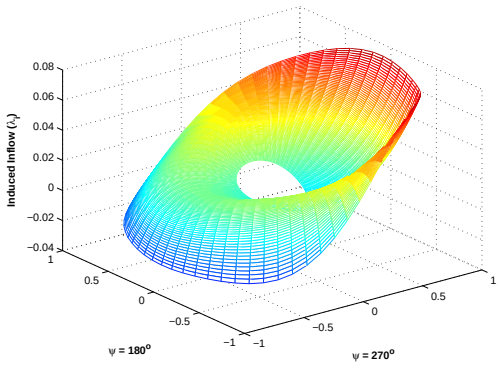

(c) Peters-He 21-State Induced Flow

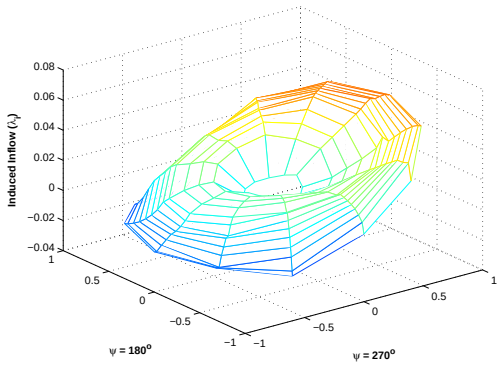

(d) Measured Induced Flow

Figure 3.2: Peters-He 6, 15, 21-State and Measured Induced Flow 3-D Plots, Rectangular Blade, $\mu = 0.15$

3.4.1.2 Contour Plots

Another approach to visualize induced flow distribution on the rotor disk are the contour plots. These plots are established by equipotential lines covering the rotor disk. From figure 3.3(a), it is seen that uniform inflow does not have any equipotential line since it consist of a single value. Similar to 3-D plots, contour plots display upwash at the front ($\psi = 180°$) and downwash at the back ($\psi = 0°$). Payne, Pitt-Peters and Peters-He 3-State inflow models have similar flow variation over disk (Figure 3.3). At the front tip of the longitudinal axis, Peters-He 3-State model (3.3(d)) predicts slightly larger upwash. Also this model has relatively greater downwash towards the rear side of the helicopter. Along lateral axis, Payne, Pitt-Peters and Peters-He 3-State models does not show any variation in this trimmed simulation.

When number of states are increased from 3 to 6, the induced flow variations on the rotor disk become non-linear (Figure 3.4(a)). Although Peters-He 6-State inflow does not have upwash at the front tip of the rotor, it clearly has longitudinal variation with comparably lesser slope. Moreover, this variation is not linear, instead longitudinal variation is in the form of a second order polynomial. Also, the Peters-He 6-State inflow model shows lateral variation. As inflow flow states increase from 6 to 15 and 21, the computed flow fields become similar to measured induced flow (Figure 3.4). Figures 3.4(b) & 3.4(c) show that increase in the state number changes the flow field on rotor disk such that characteristic double S-shaped lines become apparent. It is stated in [18, 19] that for a 4-bladed rotor, at least four harmonic numbers (15 inflow state) should be selected to capture the most fundamental characteristics of the induced flow. Indeed, Figure 3.4(c) presents the fundamental shape of the experimental flow. Although higher state inflow models have promising estimations without considering fuselage and hub drag effects, these models are still not enough for predicting the small upwash region at the tip of the advancing side (Figure 3.4(d)).

In a 4 rectangular bladed rotor configuration, predictions at the root and tip region become sufficiently well when 51 or greater inflow states are used [19]. However, inflow models with comparatively high states will add additional complexity to flight mechanics simulations. Also, they are computationally more demanding than the lower state models.

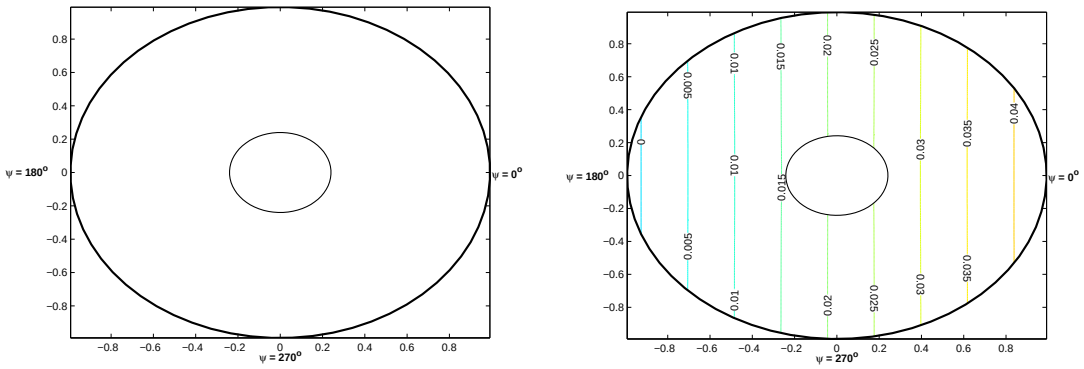

(a) Dynamic Uniform Induced Flow

(b) Payne Induced Flow

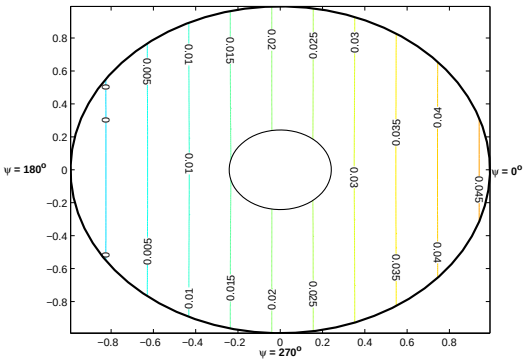

(c) Pitt-Peters Induced Flow

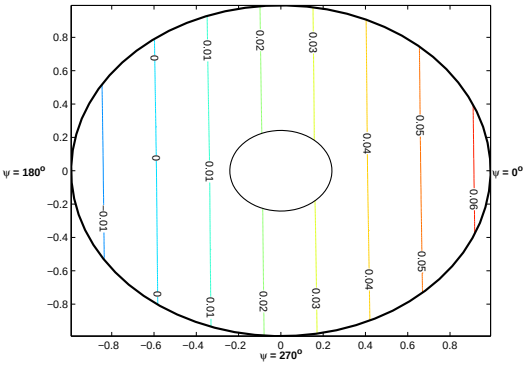

(d) Pe-He 3-State Induced Flow

Figure 3.3: Uniform, Payne, Pitt-Peters and Peters-He 3-State Induced Flow Contour Plots, Rectangular Blade, $\mu = 0.15$

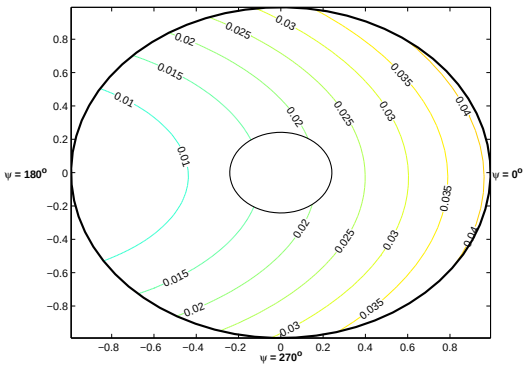

(a) Pe-He 6 State Induced Flow

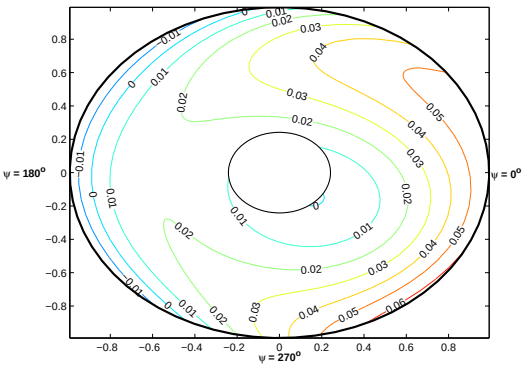

(b) Pe-He 15-State Induced Flow

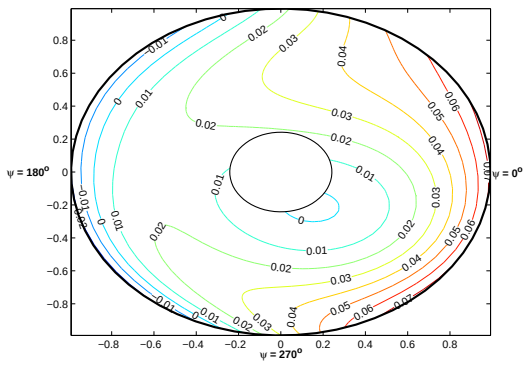

(c) Pe-He 21-State Induced Flow

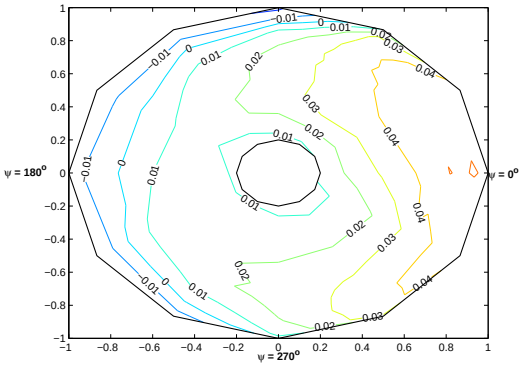

(d) Measured Induced Flow

Figure 3.4: Peters-He 6, 15, 21-State and Measured Induced Flow Contour Plots, Rectangular Blade, $\mu = 0.15$

3.4.1.3 Induced Flow along Longitudinal and Lateral Axes

In simulation, all sectional forces and moments on rotor plane are summed, and moved to the hub. Components of the these forces and moments on the hub plane become parallel to longitudinal and lateral axes at the hub. From the hub, these forces and moments are transformed to the body reference system and they are finally carried to center of gravity for 6-DOF calculations.

Figure 3.5 presents the inflow estimations along the lateral axis. Obviously, uniform inflow does not have any variation. In this trimmed condition, Payne, Pitt-Peters and Peters-He 3-State inflow models have uniform flow in lateral axis. Peters-He 15 & 21-State inflow follow the experimental trend at the advancing side near blade tip. Compared to 15 & 21 state models, Peters-He 6-State inflow model has opposite trend. However, their inflow estimations are relatively worse when inflow along the retreating side is concerned.

Longitudinal inflow variation displays better correlations with respect to the lateral axis (Figure 3.6). While uniform inflow consist of a single value, Payne, Pitt-Peters and Peters-He 3-State inflow models have linear distribution along longitudinal axis. In addition to these models, Peters-He 6-State inflow model also presents linear variation. Although Payne, Pitt-Peters and Peter-He 6-State are relatively close to each other, Peters-He 3-State model demonstrates excessive linear variation compared to others. Figure 3.6 shows that higher state inflow models have better correlation towards the root, however they still have discrepancies, especially at the aft of rotor in predicting the inflow near the blade tip. According to [19], rectangular blades require higher inflow states in order to achieve improved correlation around the tip region. In a rectangular blade, pressure becomes relatively larger towards the blade tip when compared to tapered blade. Thus, models with rectangular blades converge slowly near the tip and because of that they need more inflow states for better correlation. In Figure 3.6, Peters-He 15 & 21-State inflow models closely follow the inflow trend from hub center to front of the rotor. At the front tip, they calculate slightly more upwash than the measured flow. Around the center, these high state models overpredict the measured inflow.

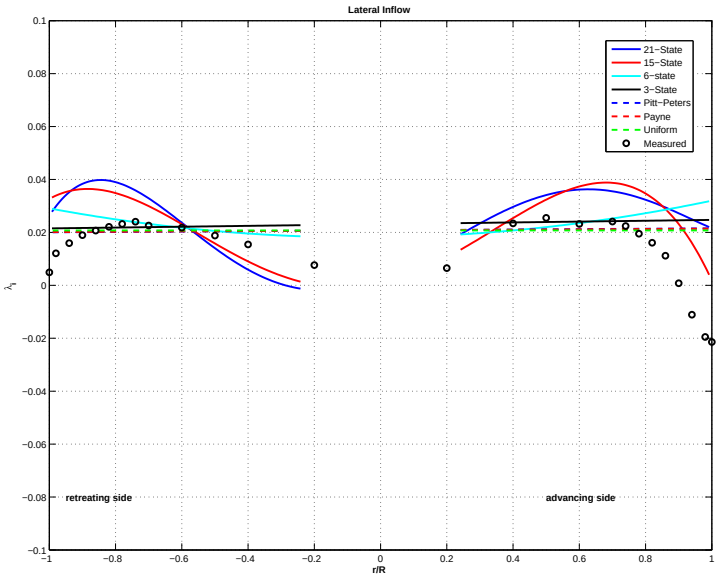

Figure 3.5: Induced Flow along Lateral Axis, Rectangular Blade, $\mu = 0.15$

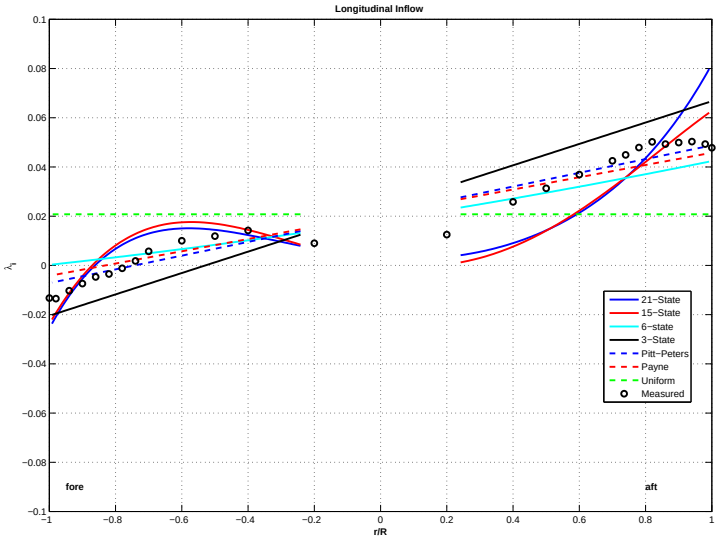

Figure 3.6: Induced Flow Along Longitudinal Axis, Rectangular Blade, $\mu = 0.15$

3.4.2 Tapered Blade

In tapered blade configuration, model construction is similar to the rectangular blade configuration. In this section, addition to the rectangular blade model, steady-state control settings are given.

3.4.2.1 3-D Plots

In tapered blade case, considered inflow models are plotted through Figures 3.7 and figure 3.8. Uniform inflow has a single value on the entire rotor as shown in Figure 3.7(a). Models with linear variation along longitudinal axis such as Payne, Pitt-Peters and Peters-He 3-State inflow models are displayed in Figures 3.7(b), 3.7(c) and 3.7(d), respectively. These models have less downwash or upwash towards the fore of rotor ($\psi = 180°$) and they have greater downwash towards to aft ($\psi = 0°$). Here, Peters-He 3-State inflow model has larger slope than other models. Due to this large slope, the Peters-He 3-State model has more upwash and more downwash along longitudinal axis. In steady-state condition with minimal longitudinal and lateral flapping angle, Payne, Pitt-Peters and Peters-He 3-State inflow models do not show any variation along lateral axis.

Unlike the models with longitudinal distribution, the Peters-He 6-State inflow model (Figure 3.8(a)) demonstrates a non-linear variation from the retreating side to the advancing side. The Peters-He 6-State, the magnitude of inflow become less towards the tip along lateral axis. Figures 3.8(b) and 3.8(c) shows that higher state inflow models can capture the fundamental characteristics of the measured inflow. Peters-He 15-State inflow model exhibits good correlation except near the blade tip. In order to have better prediction in the tip region, the increase in the selected harmonic numbers (i.e state number) are suggested. When 6 or more states are added to the Peters-He 15 State inflow model, improvement on estimation of the induced flow are seen (Figure 3.8(c)). The Peters-He 21-State inflow model, estimation of downwash towards the aft of the rotor is improved compared to Peters-He 15-State model. Also, the magnitude of the Peters-He 21-State induced flow at the retreating side ($\psi = 270°$) is reduced and become closer to the experiment.

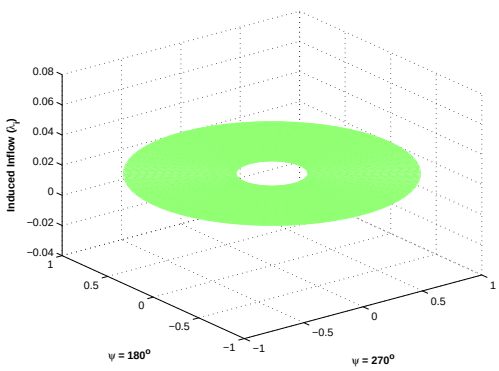

(a) Dynamic Uniform Induced Flow

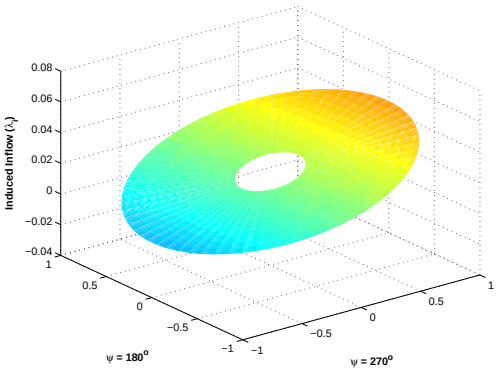

(b) Payne Induced Flow

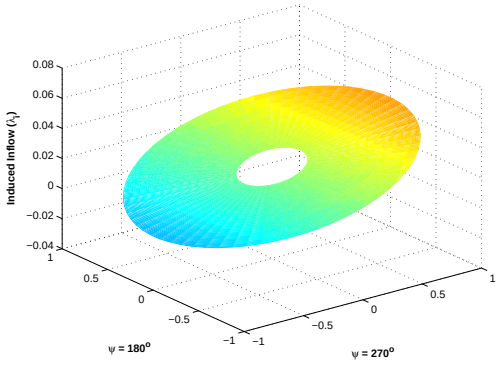

(c) Pitt-Peters Induced Flow

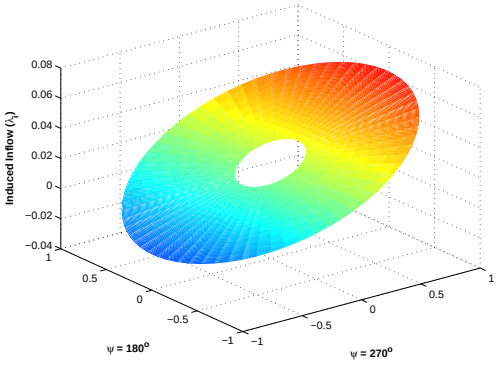

(d) Pe-He 3-State Induced Flow

Figure 3.7: Uniform, Payne, Pitt-Peters and Peters-He 3-State Induced Flow 3-D Plots, Tapered Blade, $\mu = 0.15$

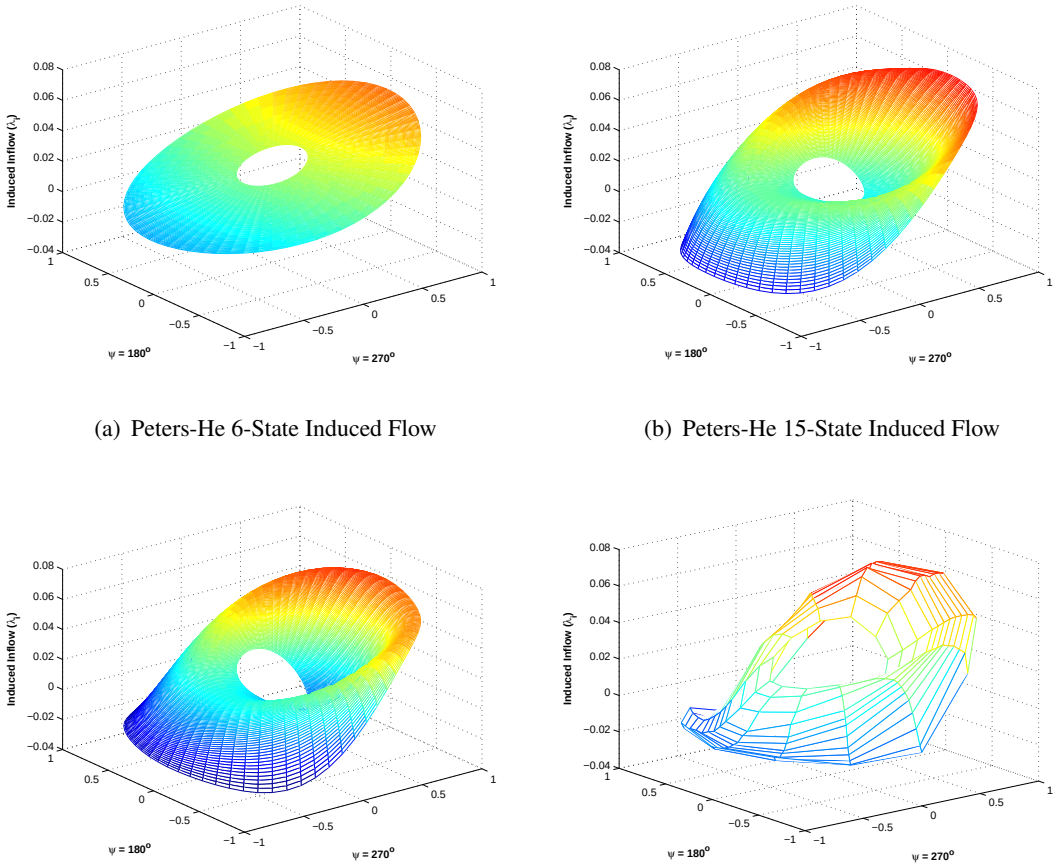

(a) Peters-He 6-State Induced Flow

(b) Peters-He 15-State Induced Flow

(c) Peters-He 21-State Induced Flow

(d) Measured Induced Flow

Figure 3.8: Peters-He 6, 15, 21-State and Measured Induced Flow 3-D Plots, Tapered Blade, $\mu = 0.15$

3.4.2.2 Contour Plots

In this section, contour plots for the tapered blade configuration are plotted. Similar to previous results, uniform inflow does not have equi-potential lines. Contour plots of Payne, Pitt-Peters and Peters-He 3 State inflow models are given in Figure 3.9. While these inflow theories have variations along the longitudinal axis, magnitude of the induced flow is constant in a selected line parallel to lateral axis. Figure 3.9(d) shows that Peters-He 3-state inflow model predicts greater upwash at the front and greater downash at the aft of the rotor compared to Payne and Pitt-Peters.

Measured inflow and higher state inflow approximations are presented in Figure 3.10. Peters-He 6-State model's contour plot (Figure 3.10(a)) has non-linear variation along lateral axis and this variation is in the reverse direction compared to rectangular blade shown previously in Figure 3.4(a). In Peters-He 6-State inflow model, when a line is selected along the lateral axis, the magnitude of induced inflow near the tip become relatively less than flow induced at the center. In the rectangular blade configuration, the magnitude of the inflow is comparatively larger near the tip. Figures 3.10(b)-3.10(c) show a characteristic "double S" shaped lines for Peters-He 15 & 21-State models. Peters-He 15-State model has more upwash than measured induced flow at the front edge. The Peters-He 21-State inflow model presents a better correlation at the front since it has better flow converges at the front edge compared to Peters-He 15-State model. The Peters-He 15-State model has better predictions towards the aft of the rotor. Along the lateral axis, both Peters-He 15-State and 21-State predictions show the correct trend (upwash) near the tip of the advancing blade. However, they have comparably worse predictions near the tip of retreating blade. These higher order models predict upwash from azimuthal position of 90° to about 240°. However, Figure 3.10(d) shows that measured inflow have upwash from 90° to 270°.

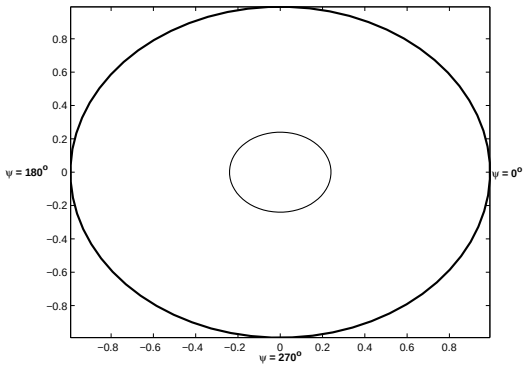

(a) Dynamic Uniform Induced Flow

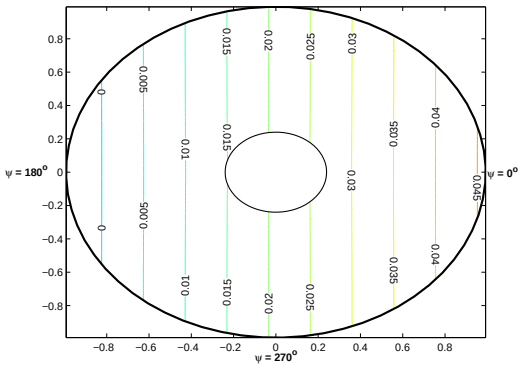

(b) Payne Induced Flow

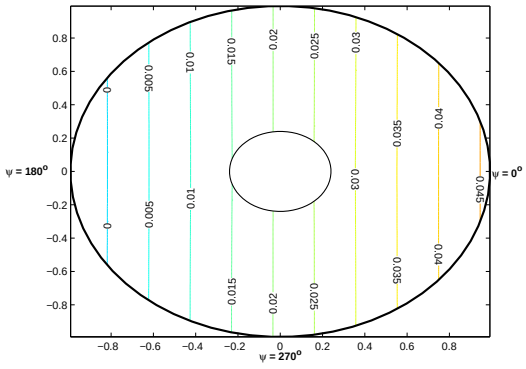

(c) Pitt-Peters Induced Flow

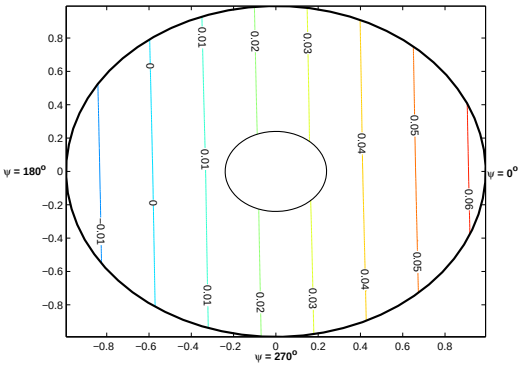

(d) Pe-He 3-State Induced Flow

Figure 3.9: Uniform, Payne, Pitt-Peters and Peters-He 3-State Induced Flow Contour Plots, Tapered Blade, $\mu = 0.15$

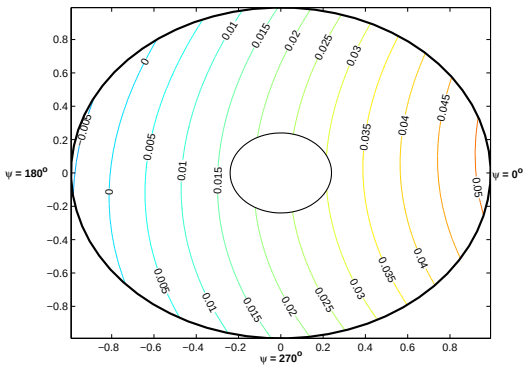

(a) Pe-He 6 State Induced Flow

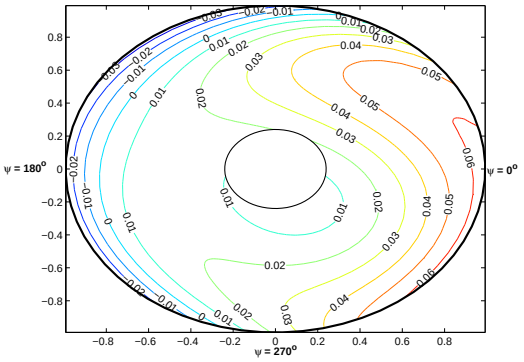

(b) Pe-He 15-State Induced Flow

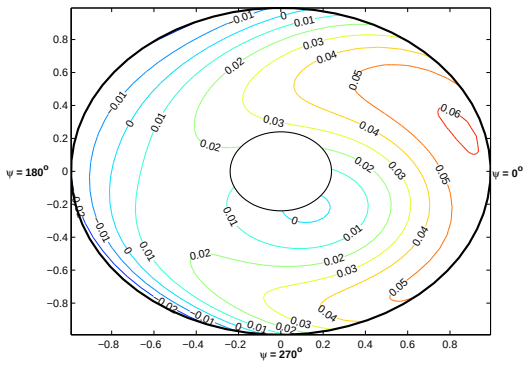

(c) Pe-He 21-State Induced Flow

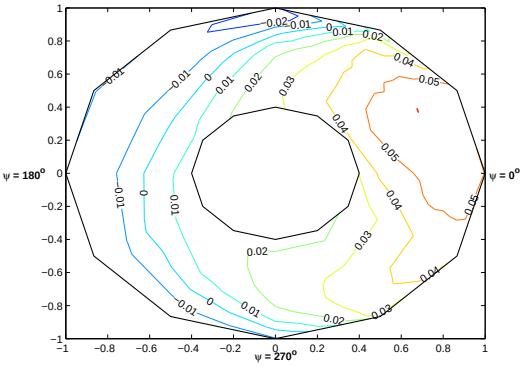

(d) Measured Induced Flow

Figure 3.10: Peters-He 6, 15, 21-State and Measured Induced Flow Contour Plots, Tapered Blade, $\mu = 0.15$

3.4.2.3 Induced Flow along Longitudinal and Lateral Axes

In this section, the induced flow predictions of tapered bladed models are closely examined along lateral and longitudinal axes. Figures 3.11 & 3.12 present inflow variation along lateral axis and longitudinal axis, respectively.

Along the lateral axis, uniform inflow and Payne, Pitt-Peters and Peters-He 3-State models do not exhibit any variation. Similar to the rectangular blade case, the Peters-He 6-State inflow model displays less variation along the lateral axis, but in this case the direction of the variation is reserved. This reversed flow makes Peters-He 6-State inflow estimation closer to the experimental results. Similar to the Peters-He 6-State inflow case, Peters-He 15-State and 21-State inflow predictions become closer to the data near the blade tip compared to rectangular case.

Along the longitudinal axis, Payne, Pitt-Peters and Peters-He 3-State models show linear distribution. Addition to these low state models, Peters-He 6-State model also exhibit linear variation and its variation is close to the Payne and Pitt-Peters. Higher order induced flow models estimate the induced flow at the tip of rotor aft well, yet they have discrepancy in the upwash estimations near the front tip.

3.4.2.4 Control Positions

Control positions in trimmed condition are collected for the tapered blade models and are compared with the experimental settings. Control positions are given in Table 3.2. All models generate a relatively close collective (θ_0) pitch angle position and a longitudinal cyclic setting (θ_{1s}) compared to the experiments. However, inflow models show differences on the lateral cyclic control position (θ_{1c}). While the Peters-He 3-State model overpredicts the lateral cyclic, Payne and Pitt-Peters inflow models underpredict the lateral cyclic. Higher state models such as Peters-He 15 and 21-State show competitively better correlation with the data. However, in lateral cyclic estimation uniform inflow has poor prediction compared the other models. The effect of the inflow variation over the flapping angle (flapping angle changes the control settings) is discussed in Chapter 4.

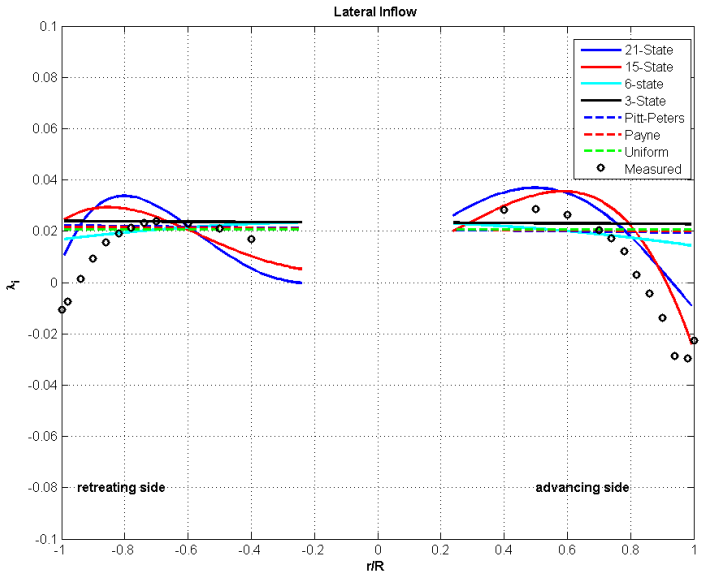

Figure 3.11: Induced Flows in Lateral Axis, Tapered Blade, $\mu = 0.15$

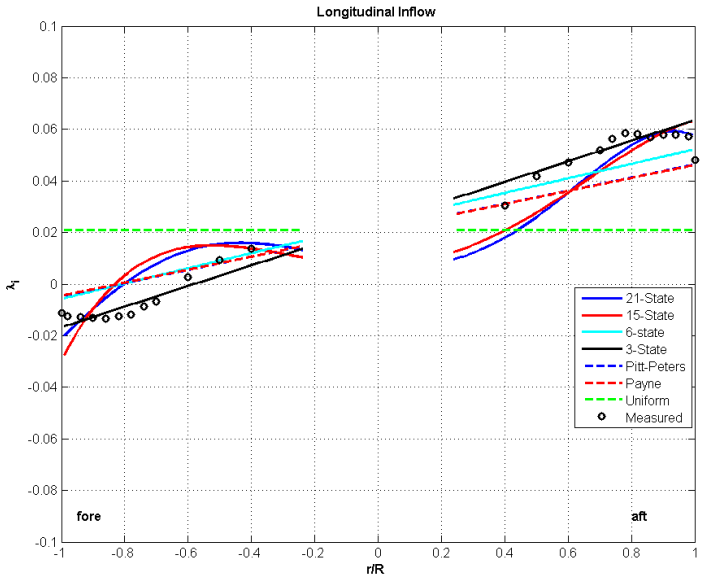

Figure 3.12: Induced Flows in Longitudinal Axis, Tapered Blade, $\mu = 0.15$

Table 3.2: Controller Settings of Inflow Models, Tapered Blade Configuration, $\mu = 0.15$

	Measured	**Uniform**	**Payne**	**Pitt-Pe**	**Pe-He 3**	**Pe-He 6**	**Pe-He 15**	**Pe-He 21**
$\boldsymbol{\theta_0}$	6.260	5.943	5.941	5.935	6.148	5.999	6.130	6.140
$\boldsymbol{\theta_{1c}}$	-2.080	-0.295	-1.714	-1.719	-2.545	-1.920	-2.206	-2.193
$\boldsymbol{\theta_{1s}}$	1.960	1.846	1.850	1.842	1.846	1.895	1.905	1.850

3.5 Observations

In this chapter, inflow models with rectangular and tapered blade configurations are examined. 3-D plots are used to visualize the inflow on rotor disk, and these plots clearly show the magnitude of the induced flow on the rotor disk. In literature, contour plots are more common and they are better at the presenting trend. Together with the 3-D and contour plots, the inflow along the lateral and longitudinal axes are displayed for comparison with [35]. Finally, the control positions of the tapered bladed models are collected and compared with the measured settings. The following observations are made using the results in this chapter:

- Models such as Payne, Pitt-Peters and Peters-He 3-State have only linear variation along longitudinal axis when they are trimmed to zero tip path plane angle.
- Peters-He 3-State inflow model has a steeper linear inflow variation than the Payne and Pitt-Peters inflow models along the longitudinal axis.
- Visible variation along lateral axis starts with Peters-He 6-State, but it is small compared to higher state models.
- Higher order models have better flow patterns when compared with the measured flow.
- Tapered bladed models have better correlation compared to rectangular ones, especially near the blade tip.
- Excluding the uniform inflow, estimated controller settings are in good agreement with measured ones.

By redoing the same simulations with [18, 19, 35] and having similar results, it is concluded that constructed blade element model with different inflow theories are validated for future use.

CHAPTER 4

EFFECT OF INFLOW DISTRIBUTION ON FLAPPING ANGLE

4.1 Introduction

Helicopter flapping has utmost importance in flight simulations due to its strong effect on handling qualities. Rotor inflow has substantial contribution to the simulation of the blade motion and therefore to the flapping motion ([24]). The non-uniform rotor inflow affects the prediction of the blade loads, rotor performance, handling qualities, vibration and noise, etc. Moreover, at low advance ratios the blade motion is influenced by integrated effects of non-uniform inflow [24]. Therefore the effect of rotor inflow becomes particularly important at low speeds.

In this chapter, the flapping angles of the rotor with various inflow models and the experimental setup are compared. The analytical solution based on harmonic balance approach is discussed and solution is compared with the experimental data. After that, dynamic inflow theory flapping angles estimations are compared with the experiment. Finally, observations regarding simulation results are pointed out.

4.2 Experimental Setup and Implementation

Helicopters show relatively larger lateral flapping angle at the low advance ratio flight. This large lateral flapping angle is mainly caused by the longitudinal inflow variation. In order to investigate this effect, an experiment [24] on the model rotor of the CH-

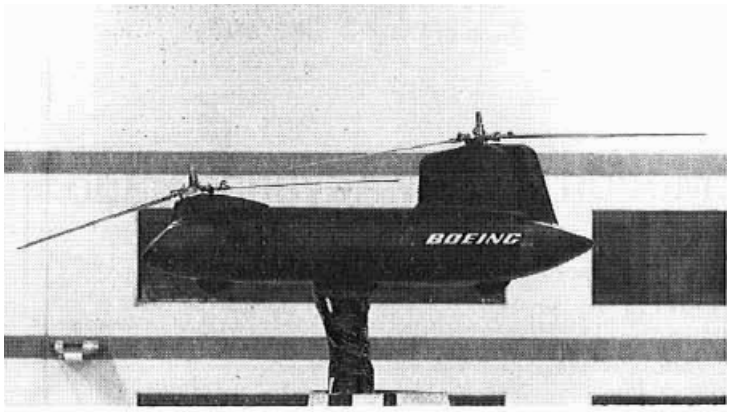

Figure 4.1: CH-47C Model Rotor

47C is conducted in the Boeing V/STOL Wind Tunnel. Figure 4.1 shows the resized rotor [24]. This rotor has tandem configuration and its forward rotor was removed to eliminate front rotor's wash on the rear rotor. Removing the front rotor also minimizes the fuselage and rear rotor interaction. Therefore, the rear rotor can be treated as an isolated rotor model with insignificant component interaction [24].

The rotor model explained in Chapter 2.6 is a well-known blade element rotor model which uses second order rigid blade flapping solution. Here, the default inflow model is replaced with the inflow models previously explained in Chapter 2.

The blade element model uses 16 virtual blades to calculate hub forces and moments on the rotor disk. Each rotor blade is divided into 40 elements and elements become denser towards the blade tip. In the calculations of the angle of attack, the inflow is taken to be perpendicular to each blade element. Due to fast dynamics of the rotor model used (resized, faster RPM), the time increment is reduced and is about 1/600 seconds. After calculating the rotor forces and moments on the hub, these forces are averaged based on the actual blade number. The parameters of [24] are used and tabulated in Table 4.1.

In this chapter, the isolated rotor model is always trimmed to a desired thrust condition for a given advance ratio, shaft tilt, longitudinal and lateral cyclic. The result of the trim routine then are the lateral and longitudinal flapping angles, coning angle and the collective input angle.

Table 4.1: CH-47C Resized Rotor Parameters

Parameter	Value
Radius	2.73 ft
Chord	0.191 ft
Linear Twist	-9.14 deg
Lift Curve Slope	5.73 /rad
Blade Number	4
Hinge Offset	0.0625 ft
Root Cut-out	0.525 ft
Weight Moment	0.49 ft-lbs
Flapping Inertia	0.0248 slug-ft^2
Nominal RPM	1574

4.3 Harmonic Balance Solution

In steady state, the flapping equation can be solved analytically. In the analytical solution, the flapping is approximated with a Fourier series expansion. If this series is truncated after the first cosine and sine terms, then flapping angle can be expressed as follows:

$$\beta = a_0 - a_1 \cos\psi - b_1 \sin\psi \tag{4.1}$$

Using the flapping expression given in equation 4.1 and its first and second derivatives, a second order flapping equation can be analytically solved. The analytical flapping solution is not shown here, since it is a classic solution already given in [36, 27, 26, 28]. Moreover, the same wind tunnel test results and analytical solution are analyzed in [36]. Findings from [36] are presented in Figures 4.2 and 4.3. Longitudinal flapping angles, a_1, show excellent agreement with the measurement. On the other hand, analytical estimations of the lateral flapping angles, b_1, have large errors compared to the experiment. In order to improve these estimations, one can use a more complex lateral flapping equation with correction factors [36]. These analytical expressions implicitly include inflow variation along longitudinal axis. In the next section, effect of the inflow on the numerical solution of the flapping angles is examined.

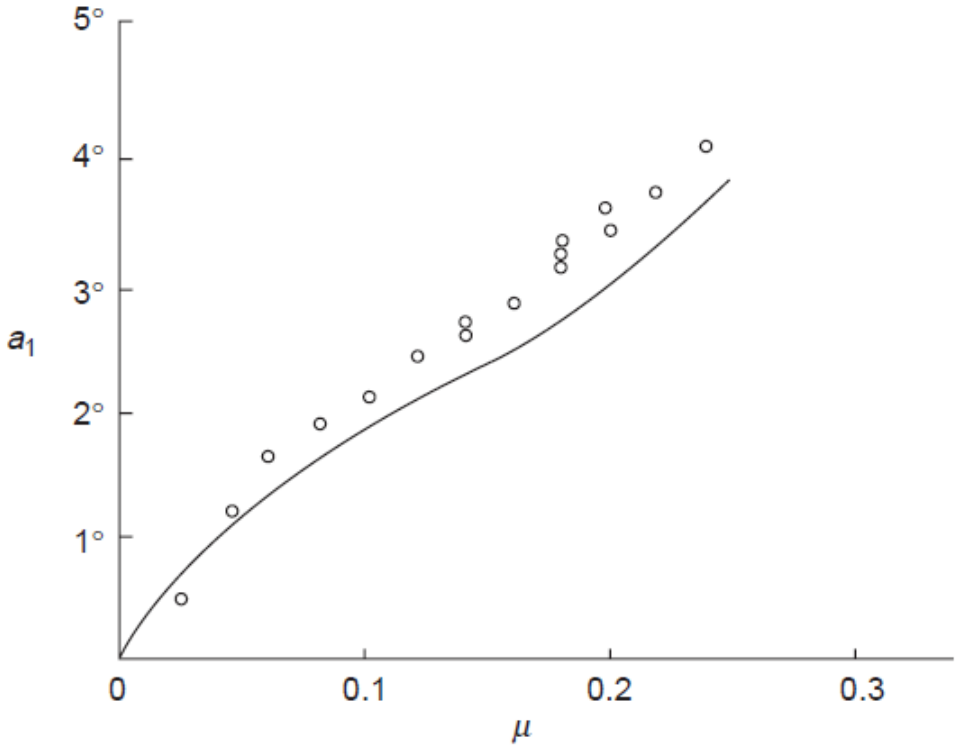

Figure 4.2: Longitudinal Flapping Angle, a_1, Measured and Analytical Solution

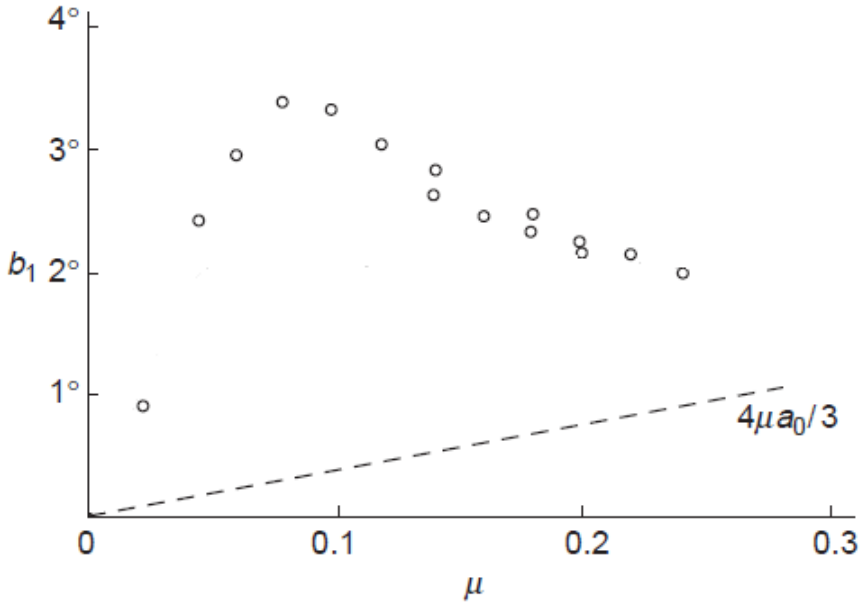

Figure 4.3: Lateral Flapping Angle, b_1, Measured and Analytical Solution

4.4 Simulation Results and Discussion

In [24] the resized CH-47C rotor is tested in the wind tunnel using three sweeping parameters. Those parameters are a sweep in the advance ratio, shaft tilt and collective position. In all three experiments, the lateral cyclic and longitudinal cyclic input positions are set to 0 and 0.73 degrees, respectively.

4.4.1 Advance Ratio Sweep, $\mathbf{C_T/\sigma = 0.08}$, $\alpha_{\mathbf{tpp}} = +1^\circ$ Aft

In the first experiment, the advance ratio is swept from 0 (hover) to 0.24. In this test, the normalized rotor thrust coefficient, C_T/σ, is fixed to 0.08 and the rotor tip path plane angle, α_{tpp}, is held around 1 degree towards the aft rotor.

The variation in the lateral flapping angle in steady-state with respect to the advance ratio is presented in Figure 4.4. Results are similar to [24] for uniform inflow. Throughout the advance ratio sweep, the uniform inflow model has a relatively large error in predicting the lateral flapping angle. Pitt-Peters and Payne's inflow models correctly predict the point of the maximum lateral flapping angle ($\mu = 0.08$). Whereas the Peters-He inflow model estimates the maximum flapping to be at an advance ratio of 0.14.

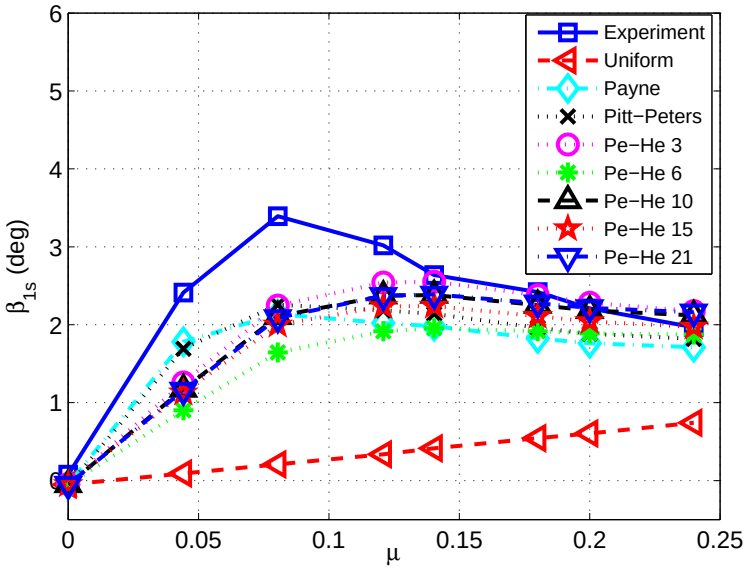

Figure 4.4: Lateral Flapping Angle vs. Advance Ratio

The advance ratio ($\mu = 0.080$) where the lateral flapping angle reaches a maximum, is of particular interest since the modelling error is also the largest at this point. Therefore, the inflow distributions along the longitudinal and lateral axes at $\mu = 0.08$ are presented in Figures 4.5 and 4.7, respectively. Additionally, the inflow distributions over the rotor disks are given in the Figure 4.8.

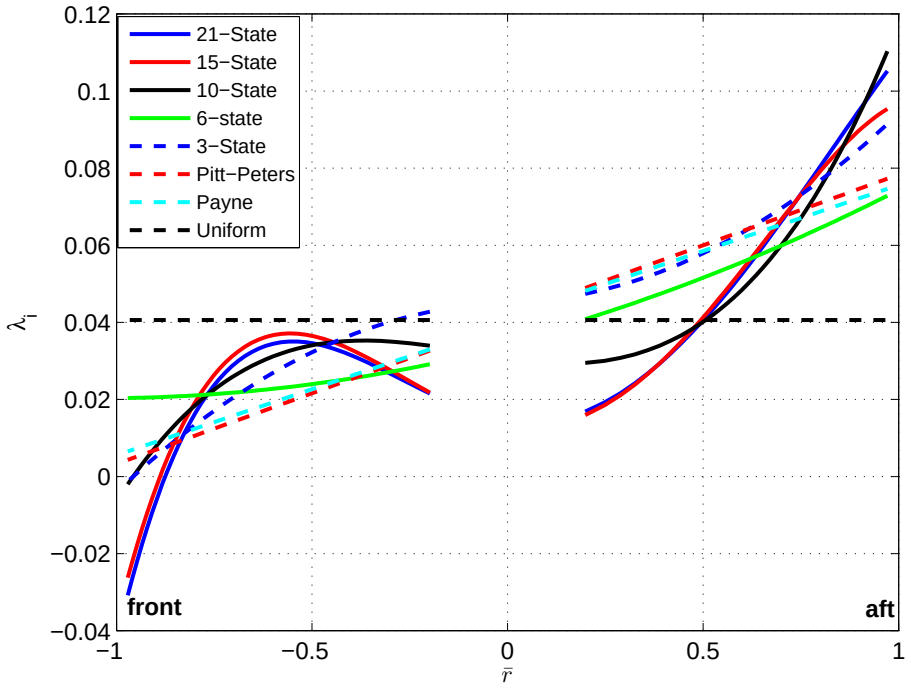

Figure 4.5: Induced Flow along Longitudinal Axis, $C_T/\sigma = 0.08$, $\mu = 0.08$

Figure 4.5 shows that the inflow distributions of Payne and Pitt-Peters Inflow models are almost identical along the longitudinal axis. As a result, the lateral flapping angle estimation of these two models are close to each other.

The Peters-He 6-State Inflow model has the lowest longitudinal inflow variation. This is a result that is obtained when the pressure coefficients of [18] are used. Therefore, the Peters-He 6-State inflow model has the lowest lateral flapping angle at this advance ratio.

Figure 4.6 shows the steady-state longitudinal flapping angle predictions with respect to advance ratio. Models have similar trends throughout the velocity range, that agrees with the experiments. However, the Peters-He 15-State inflow model seems to have the least correlation for advance ratios higher than 0.08. That is because the

Peters-He 15-State inflow model starts to predict upwash compared to other considered models around the blade tip at the advancing side (Figure 4.7). At advance ratios below 0.08, the Peters-He 15-State inflow model is closer to the Peters-He 21-State.

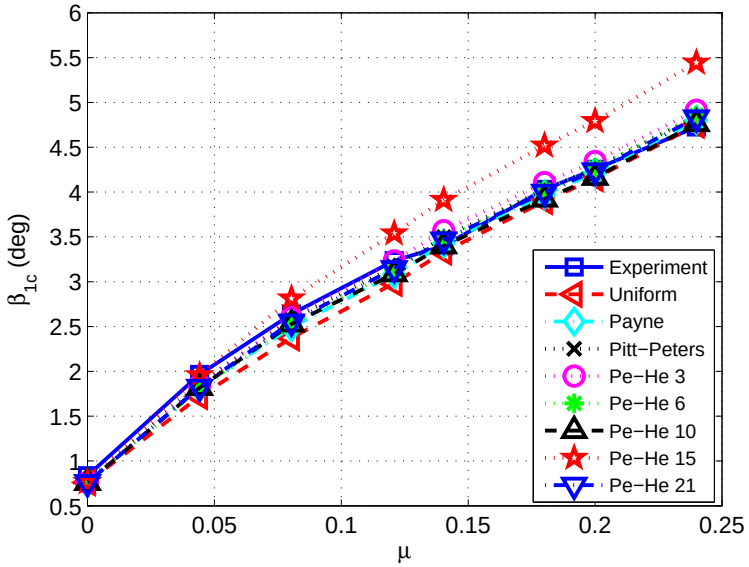

Figure 4.6: Longitudinal Flapping Angle vs. Advance Ratio

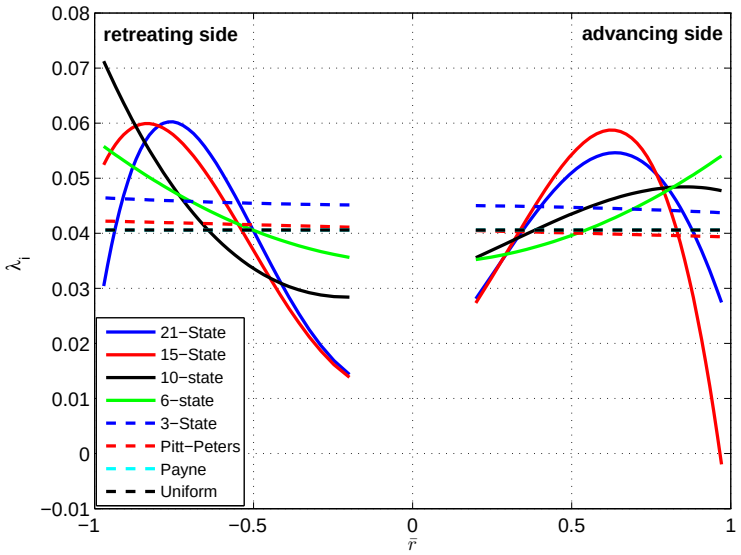

Figure 4.7: Induced Flow along Lateral Axis, $C_T/\sigma = 0.08$, $\mu = 0.08$

The results of Figure 4.6 agree with [24], in the sense that the non-uniformity in the lateral axis has a minor effect on the longitudinal flapping angle. The results of the Peters-He 15-State inflow model is an exception due to the reasons explained above. In fact, the inflow variation in the lateral axis for this model is so large (Figure 4.7) that the lateral axis inflow distribution effects the longitudinal flapping angle response.

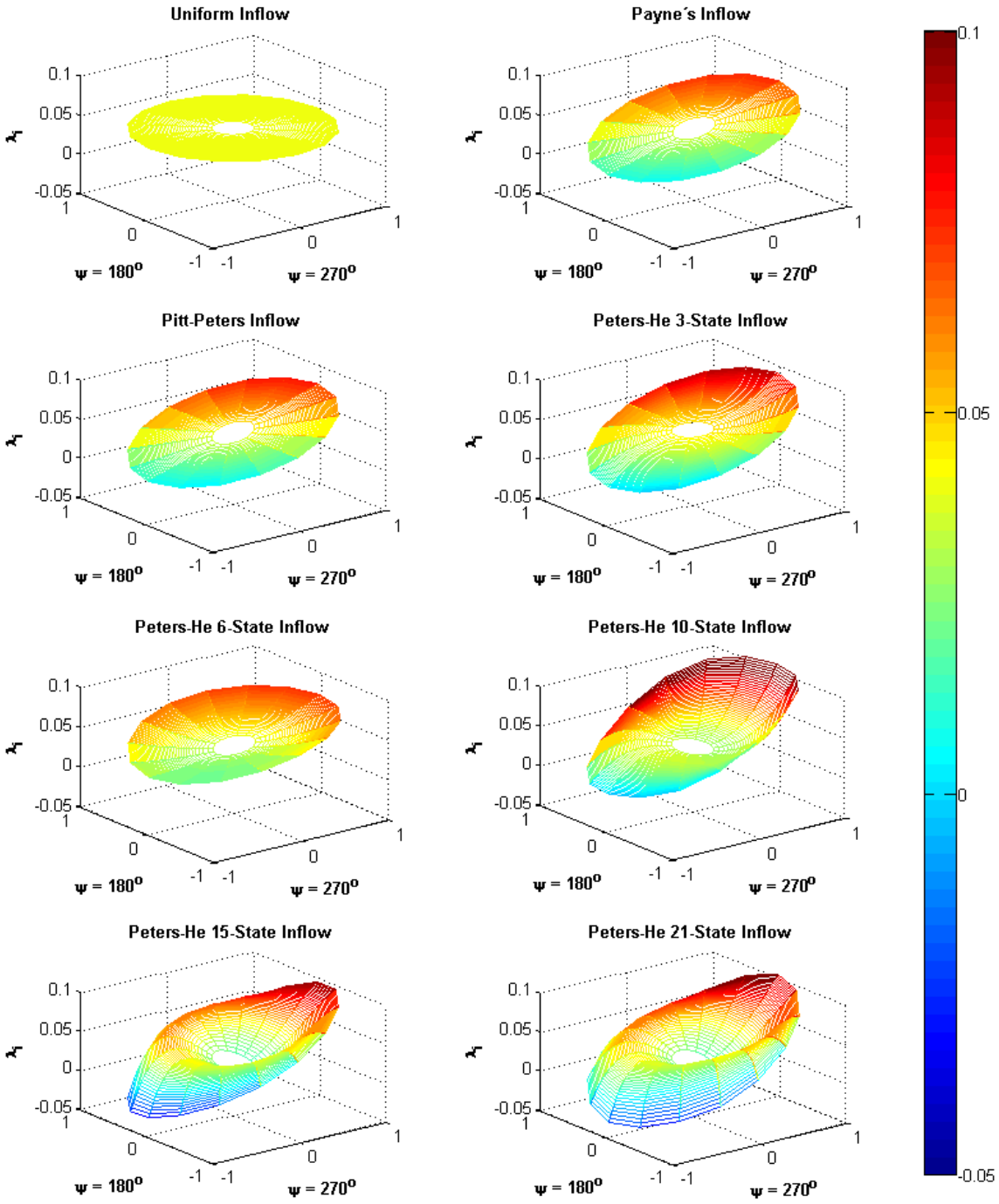

Figure 4.8: Inflow Distributions over Rotor Disk, $C_T/\sigma = 0.08$, $\mu = 0.08$

In these set of experiments, the coning angles are fixed to 3.3 degree. Estimated coning angles are compared with the experimental results in Figure 4.9. Overall, the coning angle estimations are close to the results obtained in the experiments.

The modelling error increases with the advance ratio and is always less than 0.4 degree. At low speeds, the coning angle predictions are closer to experimental data. However, as speed increases they slightly deviate. Unlike in the wind tunnel experiments, the coning angle is a function of the advance ratio in simulation.

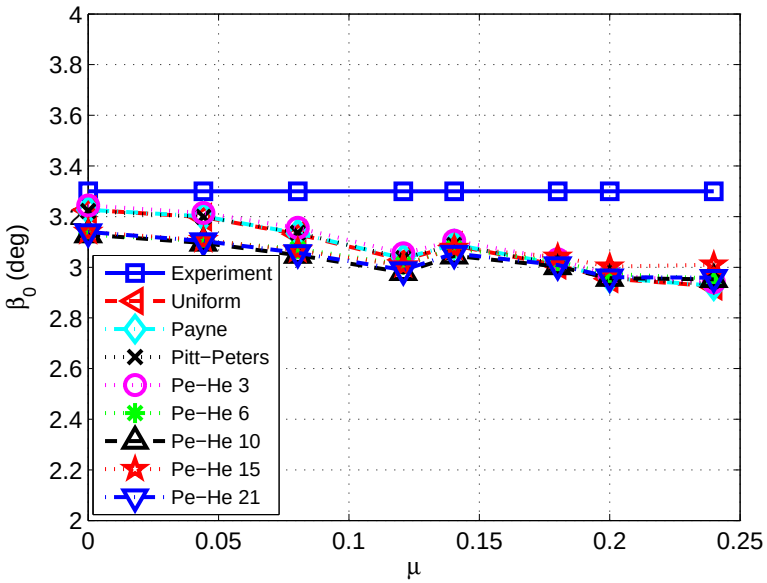

Figure 4.9: Coning Angle vs. Advance Ratio

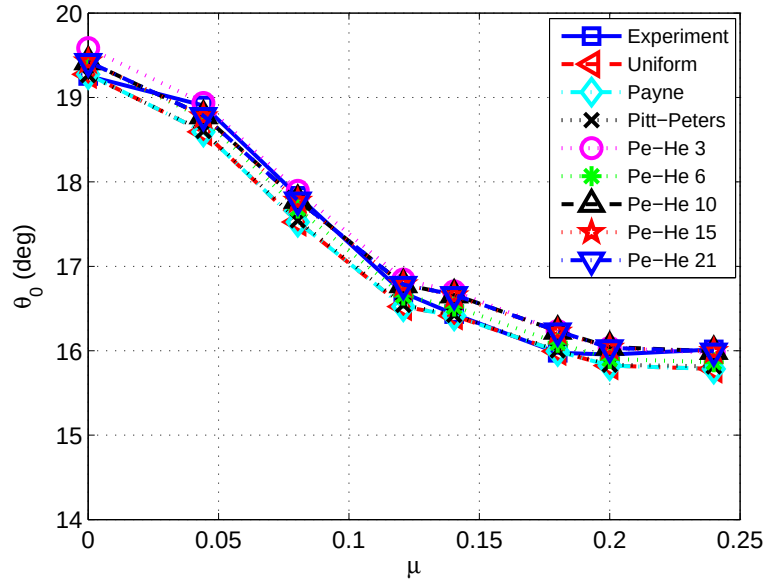

Figure 4.10: Collective Pitch Angle vs. Advance Ratio

In Figure 4.10, the trimmed collective angle variation with advance ratio is shown. This figure shows that all models have acceptable correlation with the experiment in the collective channel throughout the advance ratio sweep.

4.4.2 Collective Sweep, $\mu = 0.08$, $\alpha_s = -1.35^\circ$

The second set of experiments show the rotor flapping angle variations with respect to changing collective pitch angle. Here, the advance ratio and shaft angle are fixed to 0.08 and forward 1.35 degree, respectively. Changes in the coning, lateral and longitudinal flapping with respect to collective pitch are shown.

It is observed that, when the advance ratio and shaft tilt are fixed, the steady-state flapping angles increase rather linearly with increasing collective pitch (Figures, 4.11-4.13).

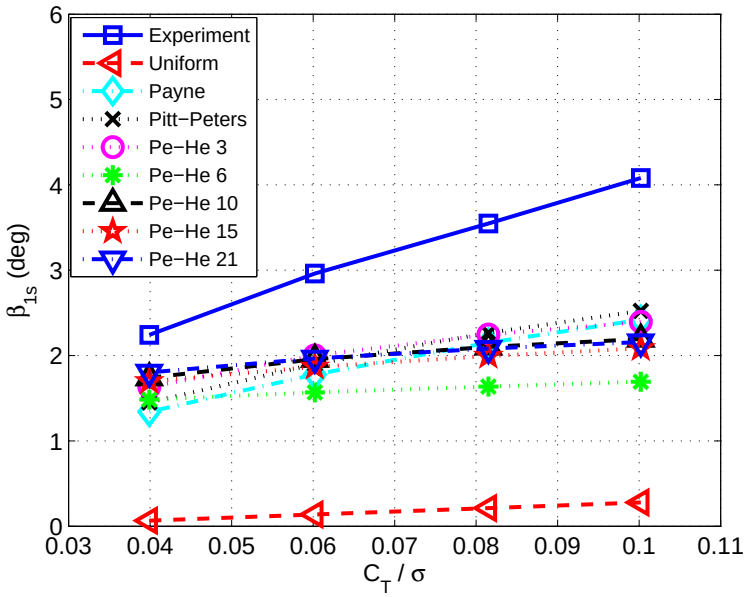

Figure 4.11: Lateral Flapping Angle vs. Normalized Thrust Coefficient

The comparison of the lateral flapping angle with the experimental data is presented in Figure 4.11. The lack of non-uniformity in the uniform inflow predictions result in large errors when compared to the results of the experiment. Other considered inflow models have better correlation. As the collective pitch increases, the lateral flapping angles also slightly increase, but not as much as observed in the experiment. Therefore, the error between the experimental data and the models become larger

with higher rotor loading.

Figure 4.12 presents the estimations for the longitudinal flapping angles. The trend of all inflow models seem to agree with the experimental data. While uniform inflow underestimates the longitudinal flapping with an offset, the Peters-He 15-State inflow model slightly overestimates the experimental flapping angle.

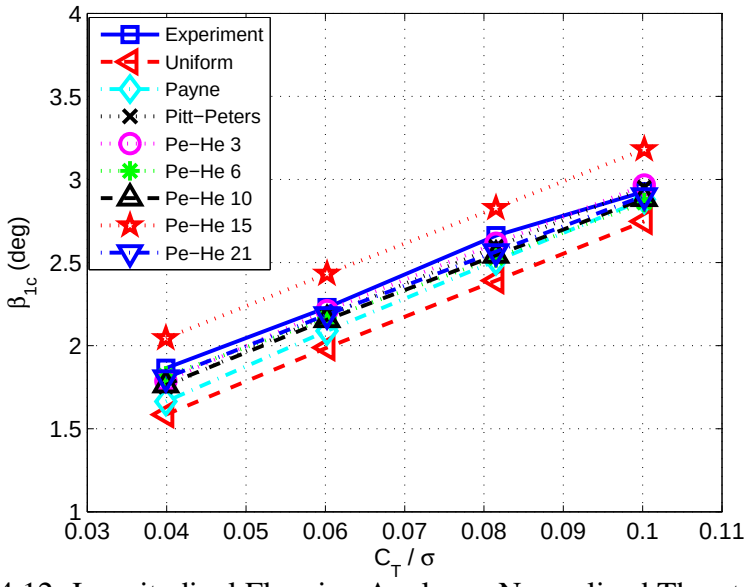

Figure 4.12: Longitudinal Flapping Angle vs. Normalized Thrust Coefficient

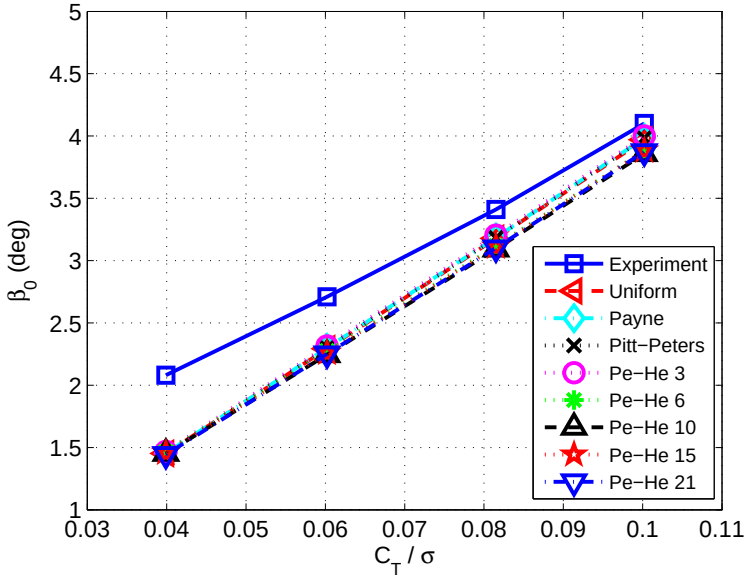

Figure 4.13: Coning Angle vs. Normalized Thrust Coefficient

The coning angle predictions are shown in Figure 4.13. All models almost have identical predictions. As the collective pitch increases, the coning angles also increase

and the error between the data and the experiment become smaller. Experimental coning and model predictions show a relatively linear trend with changing collective pitch.

4.4.3 Shaft Tilt Sweep, $\mu = 0.08$, $\theta_{0.75} = 11^\circ$

In this last set of experiments, the shaft angle is varied from -6 to 2 degrees, while the advance ratio and the collective angle are held constant at 0.08 and 11.75 degree at 75% radial location, respectively.

Figure 4.14 shows a comparison of the lateral flapping angle with respect to the shaft tilt angle. The Uniform Inflow has the largest error when compared to the experimental data. With the exception of the Peters-He 6-State inflow model, the results of the remaining inflow models are relatively close to each other. The discrepancy of the Peters-He 6-State inflow model is again credited to the fact that the inflow variation in the longitudinal axis is the least.

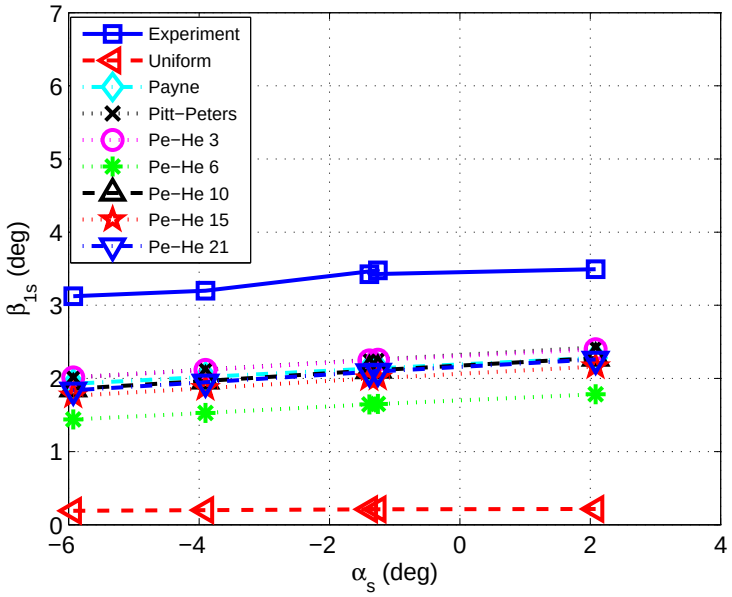

Figure 4.14: Lateral Flapping Angle vs. Shaft Tilt Angle

While the shaft tilt angle is changed from the most forward position to the most backward position, the steady-state lateral flapping angle responses show a slight increase, except the uniform inflow model (Figure 4.14).

Comparisons of the results of the longitudinal flapping angle are shown in Figure 4.15. Similar to previous findings, the longitudinal flapping angle responses are in relative good agreement with the experimental data. Here, the Peters-He 15-State inflow model overestimates the flapping angle while the uniform inflow model slightly underestimates. All models predict a constant flapping angle, while there is a small but noticeable increase in experimental data when shaft tilt is at its most backward position.

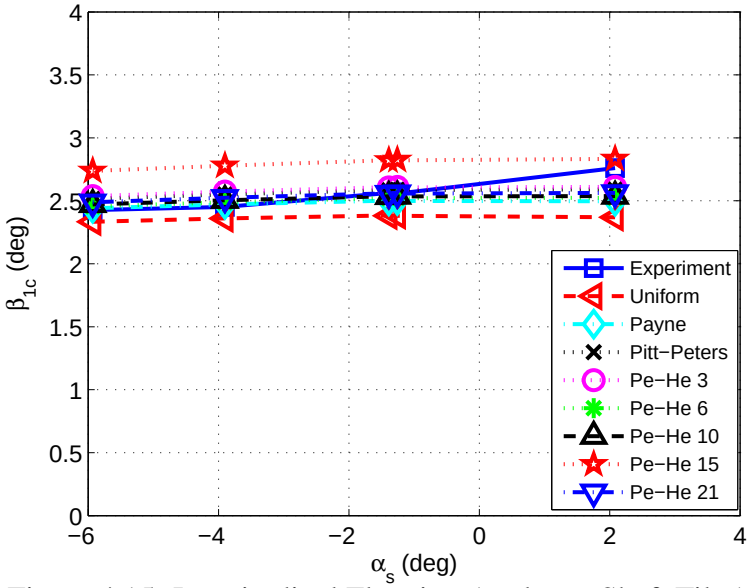

Figure 4.15: Longitudinal Flapping Angle vs. Shaft Tilt Angle

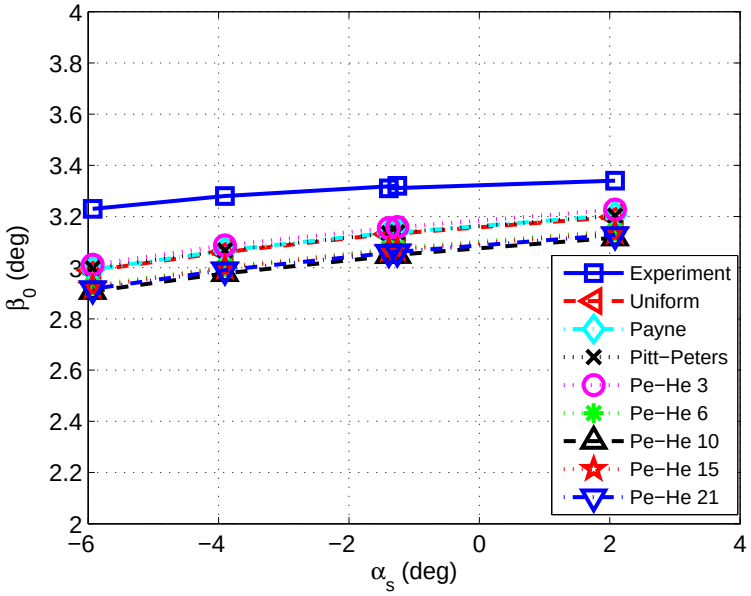

Figure 4.16: Coning Angle vs. Shaft Tilt Angle

Estimations of the coning angles are given in Figure 4.16. All rotor models show an increase in the coning angle with increasing shaft tilt angle.

4.5 Observations

The comparison of the wind tunnel test data of the resized CH-47C model rotor in low advance ratio as reported in 1972 by Harris [24] is compared with various dynamic inflow models commonly used in literature. The findings are as follows:

- Generally, the uniform inflow is not enough to predict the lateral flapping angles in steady forward flight. In fact it has the largest modelling errors.
- A simple linear variation in the longitudinal axis improves the results significantly. Therefore, using Payne's inflow variation or a Pitt-Peters Inflow variation brings the lateral flapping angle closer to the measured value in the experiments.
- As the inflow states increase, the variation of the inflow on the rotor disk also increases. Given this higher fidelity of inflow variation, one would expect that the flap angle responses in steady-state always turn out closer to the experimental results. This in fact is not always true when Peters-He inflow is modelled in a rotational system (when the original blade element rotor model structure is preserved). For instance, results corresponding to Peters-He 6-State and 15-State inflow models have shown discrepancies in this thesis.

CHAPTER 5

EFFECT OF DYNAMIC INFLOW MODELS ON STEADY-STATE PERFORMANCE RESULTS

5.1 Introduction

In this chapter, dynamic inflow models are compared with the wind tunnel test of the main rotor of the S-76 helicopter in steady-state conditions [25].

The S-76 main rotor had been tested at various test cases. In this thesis, two hover cases and two forward flight cases are selected. In hover tests, thrust of the rotor is changed from low to high values. In the first hover test, shaft angle held constant at -5 degree. In the other test, it is fixed to -15 degree. In forward flight tests, free-stream velocity is changed from low to high speed conditions. Throughout the speed range, thrust and shaft angle held constant. In the first forward flight test, normalized thrust coefficient is equal to 0.065. In the second test, it is equal to 0.080. Shaft angle is held constant at -5 degree for both forward flight cases.

The S-76 main rotor wind tunnel results are compared with the isolated rotor models having inflow models explained in Chapter 2. In hover cases; power, first harmonic blade angles (collective pitch, longitudinal cyclic and lateral cyclic) and coning angle are compared. In forward flight cases; power, side force, drag force, first harmonic blade angles and coning angle are shown. In addition to these performance results, inflow and angle of attack distributions over rotor disk are presented in some test points. Effect of these distributions over the performance results are also discussed.

5.2 Implementation

The S-76 main rotor is modelled as an isolated blade element model explained in Chapter 2.5. Inflow part of the blade element code is replaced by the dynamic inflow models explained in Chapter 2. In this chapter, dynamic uniform inflow, Payne's inflow, Pitt-Peters inflow and Peters-He inflow with higher harmonics are used. In Peters-He; 3, 6, 10, 15 and 21 inflow states are selected.

The S-76 main rotor parameters are found at [25, 37, 38] and some parameters are given at Table 5.1. Blade chord and twist distributions along spanwise direction are taken from [38] and these distributions are given at Appendix A. Airfoils' 2-D aerodynamic lift and drag coefficient tables are also taken from [38] and these tables are available in the Appendix B. The S-76 main rotor blade has two different airfoil profiles. While SC1095-R8 airfoil is used from rotor center to 80% of the blade, SC1095 airfoil is used after the 84%. Transition region between these airfoils are linearly interpolated.

Table 5.1: S-76 Main Rotor Properties

Parameter	**Value**
Radius	22 ft
Number of Blades	4
Solidity	0.0748
Hinge Offset	3.70% radius
Blade Mass	3.04 slug
Flapping Inertia	408 slug-ft^2
First Mass Moment	30 slug-ft
Hub Spring	1192 ft-lb/rad
Pitch-Flap Coupling	16.96 deg
Airfoils	SC1095R8 & SC1095
Nominal RPM	293

The S-76 main rotor's wind tunnel measurements are gathered at trimmed conditions. In wind tunnel tests, S-76 main rotor is trimmed to desired thrust and lateral & longitudinal flapping angles which are assumed to be less than 0.2 degree. Auto-pilot algorithm explained in Chapter 2.6 is capable of trimming the model to desired thrust and hub moments or first harmonic flapping angles or mixing of two. In the tests,

flapping angles are not clear, however hub moments are well documented. Therefore, isolated rotor models are trimmed to desired thrust, roll and pitch hub moments.

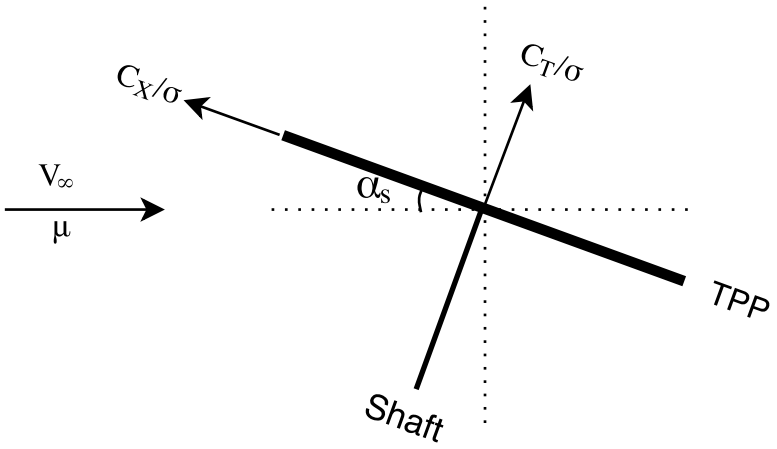

Figure 5.1: S-76 Main Rotor Axis Convention

Direction of the thrust, drag force and orientation of tip path plane can be seen from Figure 5.1. Normalized thrust coefficient, C_T/σ, is perpendicular to tip path plane. Normalized drag force coefficient, C_X/σ, is parallel to plane and normalized side force coefficient, C_Y/σ, is positive into the page direction. In the wind tunnel tests, free-stream velocity, V_∞, is taken parallel to ground.

5.3 Simulation Results and Discussion

The main rotor of the S-76 helicopter's wind tunnel test campaigns are held in number of different conditions. In this thesis, simulations are done at two hover cases and two forward flight cases.

In the first hover test, shaft angle is taken equal to forward 5 degree. In the next hover test, it is selected as -15 degree. In both hover tests, thrust is changed from low to high values. Hover results are compared in terms of power, first harmonic blade angles and coning angle for each inflow model. In addition to the performance results, inflow and angle of attack distributions are plotted for a specific case ($\alpha_s = -5^\circ,\ C_T/\sigma = 0.078$).

In both forward flight cases, shaft angle is fixed to -5 degree. In the first forward flight test, normalized thrust coefficient is held constant at 0.065. In the second experiment,

it is equal to 0.080. In these speed tests, additional performance parameters such as normalized side force and normalized drag force are also investigated. Inflow and angle of attack distributions in forward flight tests are given at two advance ratio and these advance ratios are equal to 0.2 and 0.08, respectively.

5.3.1 Hover Performance

5.3.1.1 Thrust Sweep, $\alpha_s = -5^\circ$

Normalized power coefficient, C_P/σ, comparison is given at Figure 5.2. Overall power estimations are close to experimental data. After the C_T/σ value of 0.060, all models slightly underestimate the power.

Collective angle predictions are presented in Figure 5.3. In middle thrust region, $C_T/\sigma = 0.055$, all considered models show good agreement with the experiment. When C_T/σ above 0.070, models do overprediction. In low thrust values, C_T/σ is below 0.040, simulations have slightly more collective pitch.

Figures 5.4 and 5.5 show lateral cyclic and longitudinal cyclic comparisons. For entire thrust range, longitudinal and lateral cyclic positions have fairly well agreement with the data. Although these cyclic positions have relatively small errors, both lateral and longitudinal cyclic positions are consistently underestimated throughout the thrust sweep. For both cyclic inputs, considered inflow models have almost identical results.

Coning angle estimation is given at Figure 5.6. At the lowest loading, $C_T/\sigma = 0.030$, models predict the experimental result. When thrust is increased from low loading to high loading condition, the experiment shows non-linear change in the coning angle. Normally, coning has a linear relationship with the thrust. In this case, simulation results show this linear relationship. For this test condition, experiment is affected by the ground and/or some kind of facility effect [39].

The inflow and angle of attack distributions on the rotor disk are recorded when C_T/σ is equal to 0.078. Inflow angles are plotted in Figures 5.7 & 5.8. According to Figure 5.7, uniform, Payne, Pitt-Peters and Peters-He 3-State inflow models have uniform flow field along both azimuthal and radial directions. Higher state models

such as Peters-He 6, 10, 15 and 21-State have azimuthally symmetric flow field (Figure 5.8). In the higher state models, high order radial shape functions are used and that is why these models have radial difference. In Peters-He 6 and 10-State inflow models, magnitude of inflows are increased towards the tip of the blade. However, in Peters-He 15 and 21-State inflow models, inflows are first increased, then near the tip they are reduced. Effect of these different induced flow fields over the angle of attack distribution can be seen from Figures 5.9 and 5.10. Although angle of attack distributions show slight differences near the tip of the blade, performance results given through in Figures 5.2-5.6 exhibit similar or identical results. Therefore, due to symmetry, inflow and angle of attack distributions have insignificant effect in performance evaluation in hover.

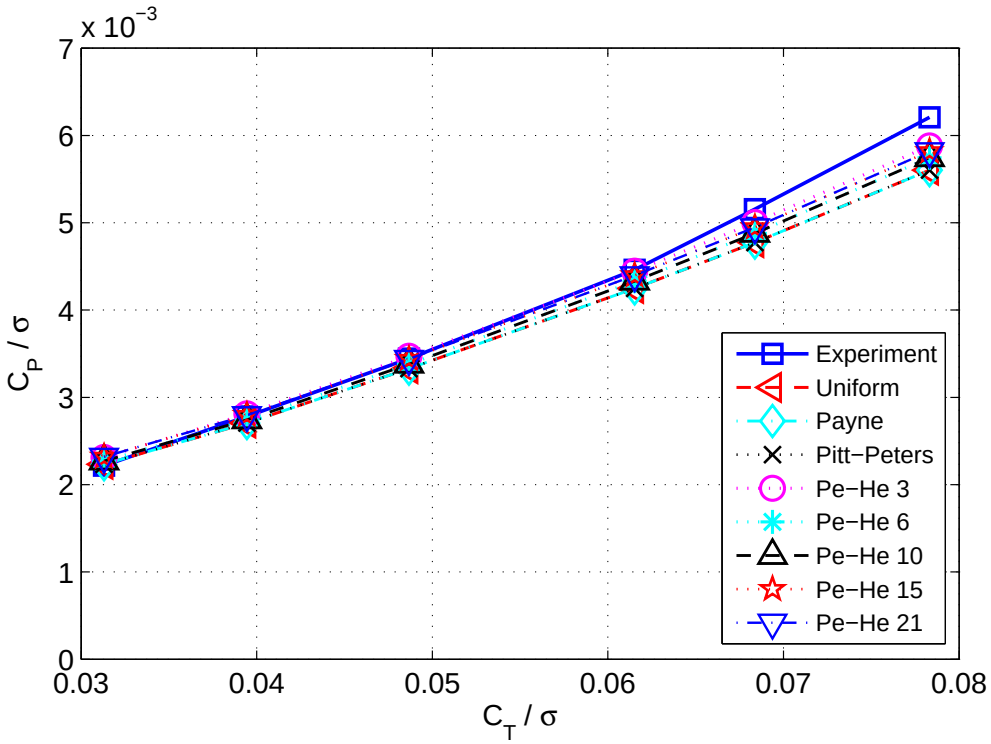

Figure 5.2: Normalized Power Coefficient vs Normalized Thrust Coefficient, at Hover, $\alpha_s = -5^\circ$

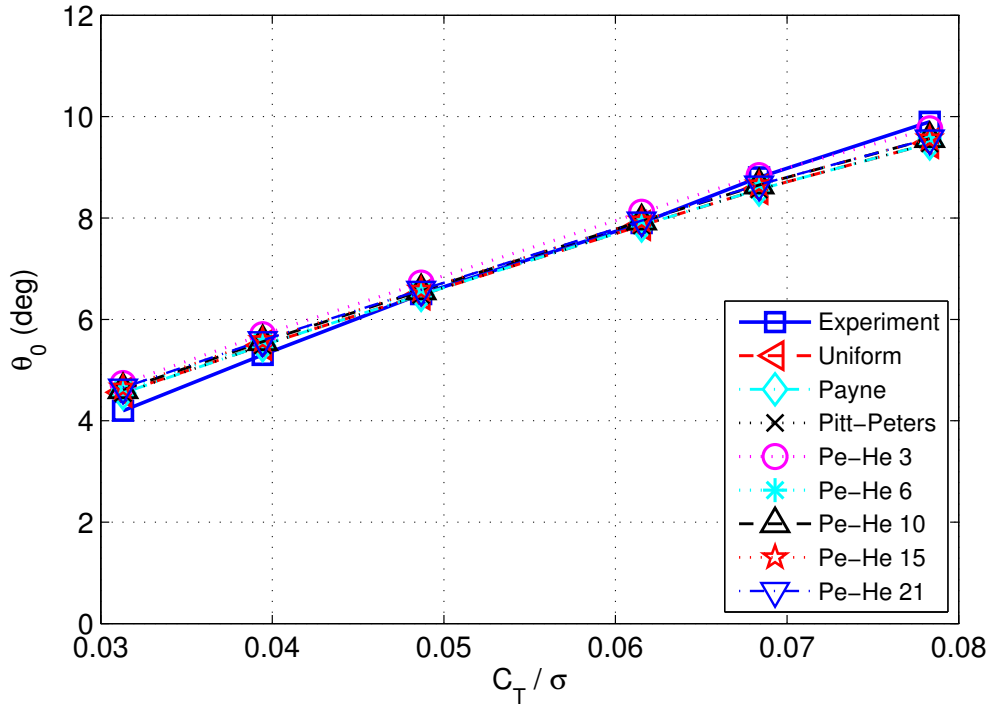

Figure 5.3: Collective Angle vs Normalized Thrust Coefficient, at Hover, $\alpha_s = -5°$

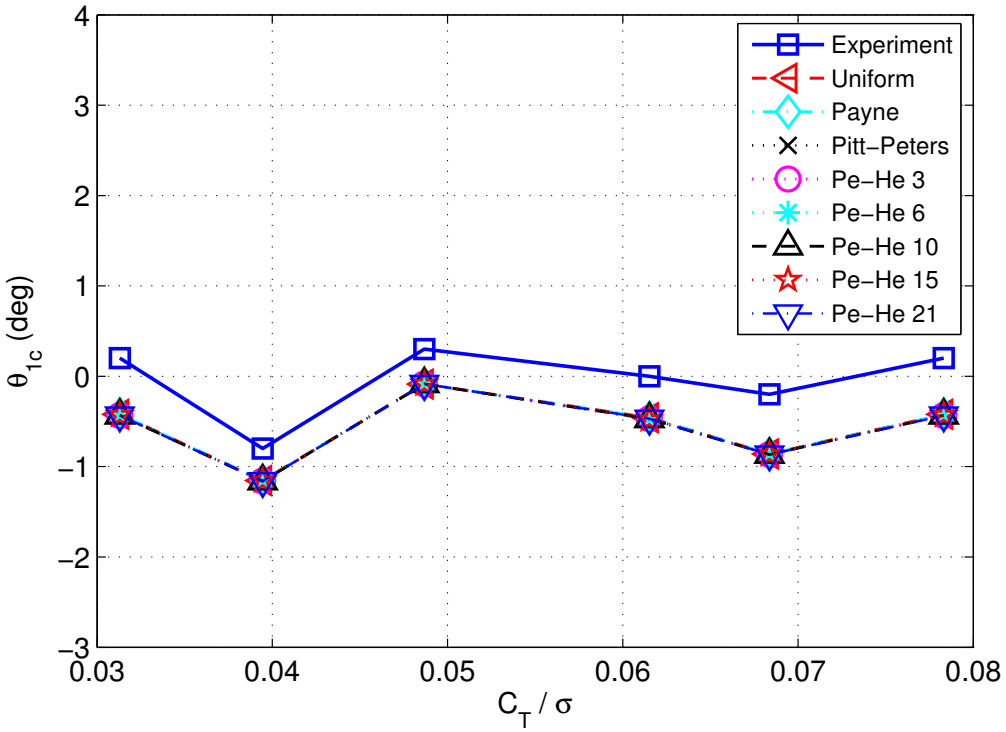

Figure 5.4: Lateral Cyclic Position vs Normalized Thrust Coefficient, at Hover, $\alpha_s = -5°$

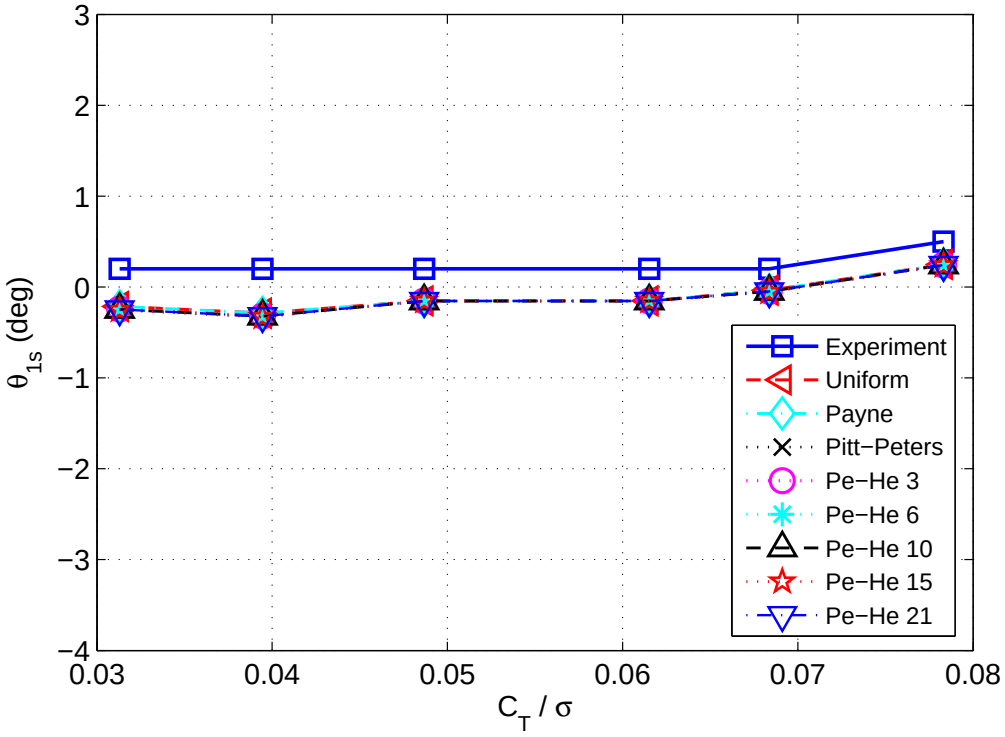

Figure 5.5: Longitudinal Cyclic Position vs Normalized Thrust Coefficient, at Hover, $\alpha_s = -5°$

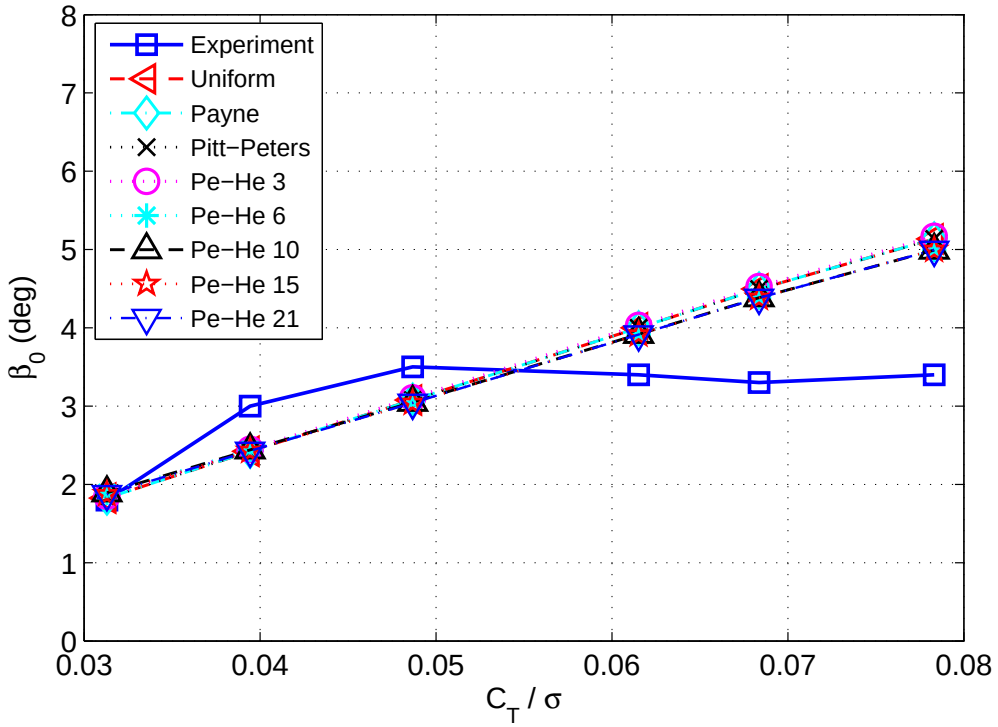

Figure 5.6: Coning Angle vs Normalized Thrust Coefficient, at Hover, $\alpha_s = -5°$

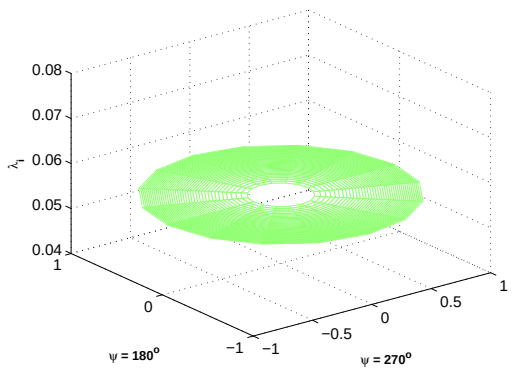

(a) Dynamic Uniform

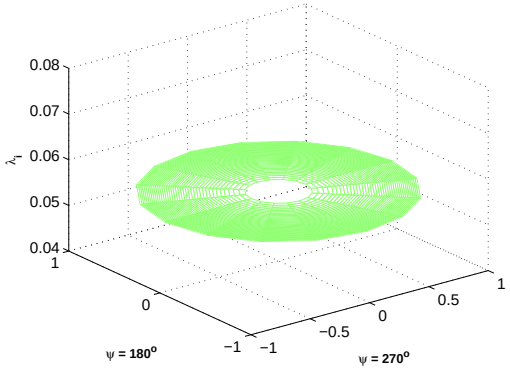

(b) Payne

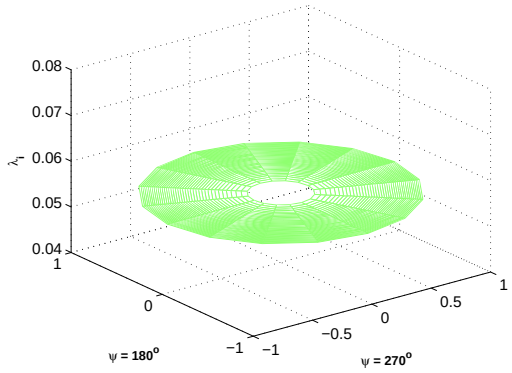

(c) Pitt-Peters

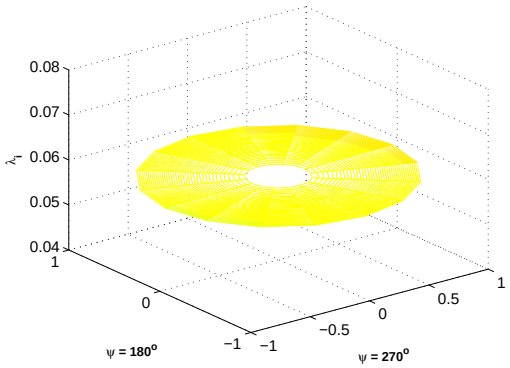

(d) Peters-He 3-State

Figure 5.7: Uniform, Payne, Pitt-Peters & Peters-He 3 State Induced Flow 3-D Plots, at Hover, $\alpha_s = -5°$, $C_T/\sigma = 0.078$

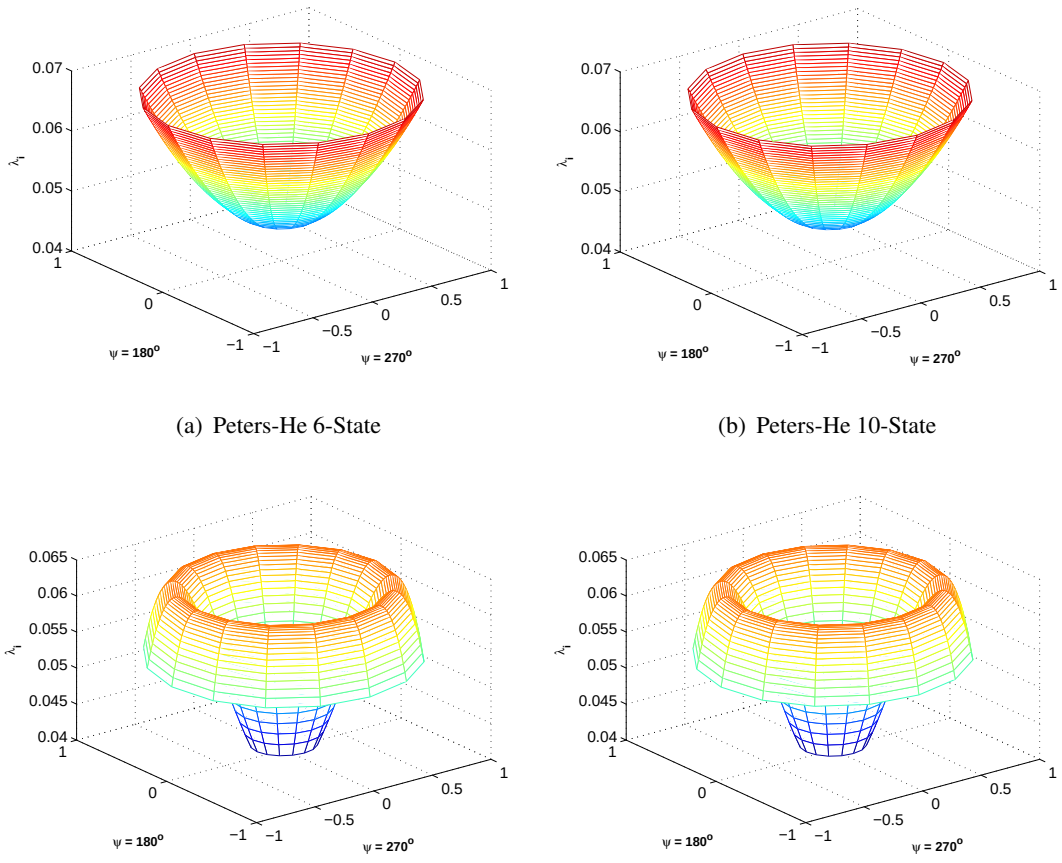

(a) Peters-He 6-State

(b) Peters-He 10-State

(c) Peters-He 15-State

(d) Peters-He 21-State

Figure 5.8: Peters-He 6, 10, 15 & 21 State Induced Flow 3-D Plots, at Hover, $\alpha_s = -5°$, $C_T/\sigma = 0.078$

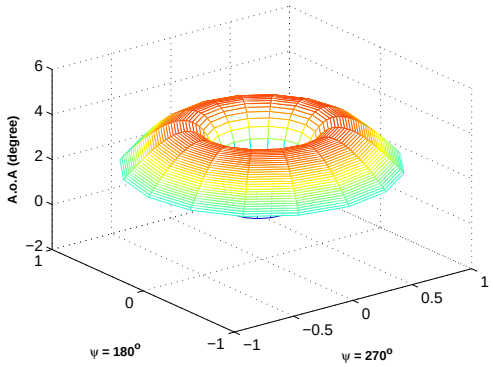

(a) Dynamic Uniform

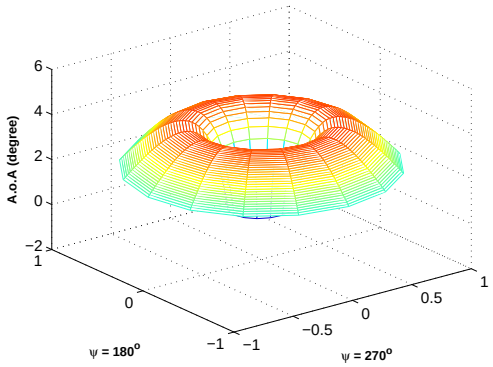

(b) Payne

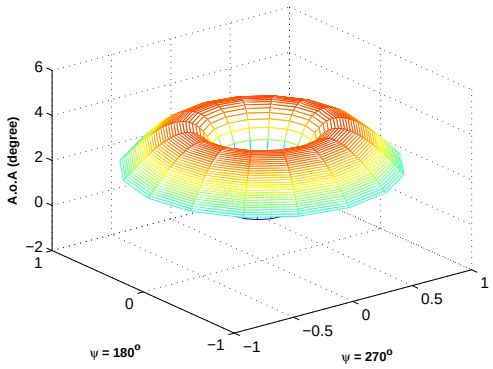

(c) Pitt-Peters

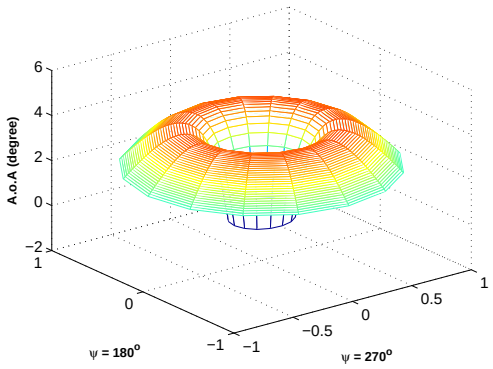

(d) Peters-He 3-State

Figure 5.9: Uniform, Payne, Pitt-Peters & Peters-He 3 State Angle of Attack Distribution, at Hover, $\alpha_s = -5°$, $C_T/\sigma = 0.078$

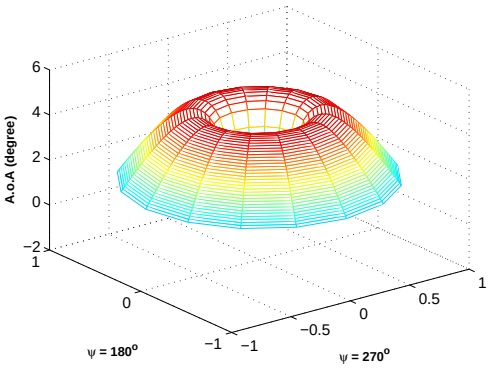

(a) Peters-He 6-State

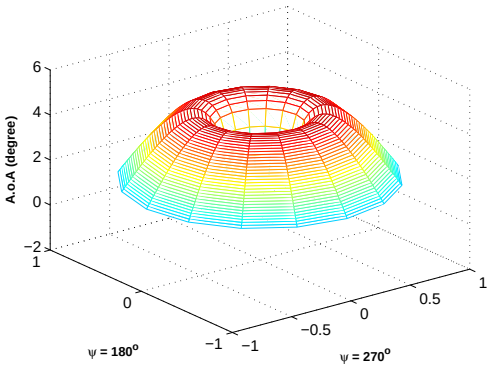

(b) Peters-He 10-State

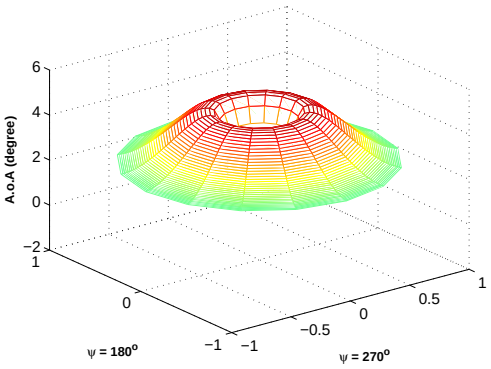

(c) Peters-He 15-State

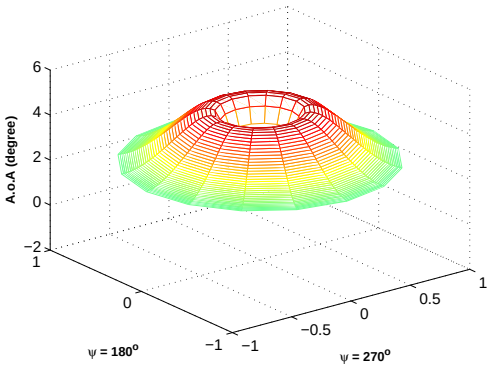

(d) Peters-He 21-State

Figure 5.10: Peters-He 6, 10, 15 & 21 State Angle of Attack Distribution, at Hover, $\alpha_s = -5°$, $C_T/\sigma = 0.078$

5.3.1.2 Thrust Sweep, $\alpha_s = -15^\circ$

In this case, shaft angle is changed from -5 to -15 degree and range of the thrust sweep is increased. Generally, simulation results are similar to previous case with the exception of the coning angle. Since performance predictions show similarities, inflow and angle of attack distributions are not presented in the second hover test.

Normalized power coefficient is compared with the experiment in Figure 5.11. All considered inflow models are close to each other. When C_T/σ is above the 0.05, all models underpredict the power with small margins. As thrust increases, divergence between the data and the inflow models become larger.

In Figure 5.12, change in the collective angle respect to normalized thrust coefficient is presented. Explained inflow models have similar predictions and they have good agreement with the data especially beneath the C_T/σ value of 0.077. When loading condition become relatively higher, models have comparably less collective angles than the experiment. At the lowest C_T/σ, collective angles become slightly larger than the data.

The lateral and longitudinal cyclic pitch positions are given in Figures 5.13 and 5.14, respectively. Likewise the previous hover test, performance results are almost identical. When C_T/σ is under the 0.04, lateral cyclic input is well correlated with the data. After 0.04, differences between data and the models become comparatively larger. The maximum error in lateral cyclic position is less than 1 degree. Compared to lateral cyclic estimations, longitudinal cyclic predictions are closer to the experiment. Throughout the thrust range, longitudinal cyclic exhibit good agreement with the experimental input.

Coning angle results respect to C_T/σ are shown in Figure 5.15. This figure indicates that experimental coning has a linear relationship with the loading or thrust level. In the previous case, experimental coning had non-linear relationship. In this case, overall coning angle estimations agree well with the data. Figure 5.15 shows that all models have larger coning to thrust ratio compared to the experiment. Therefore, considered inflow models have relatively less coning than the experiment at the low loading case. When thrust is high, models have rather greater coning angle.

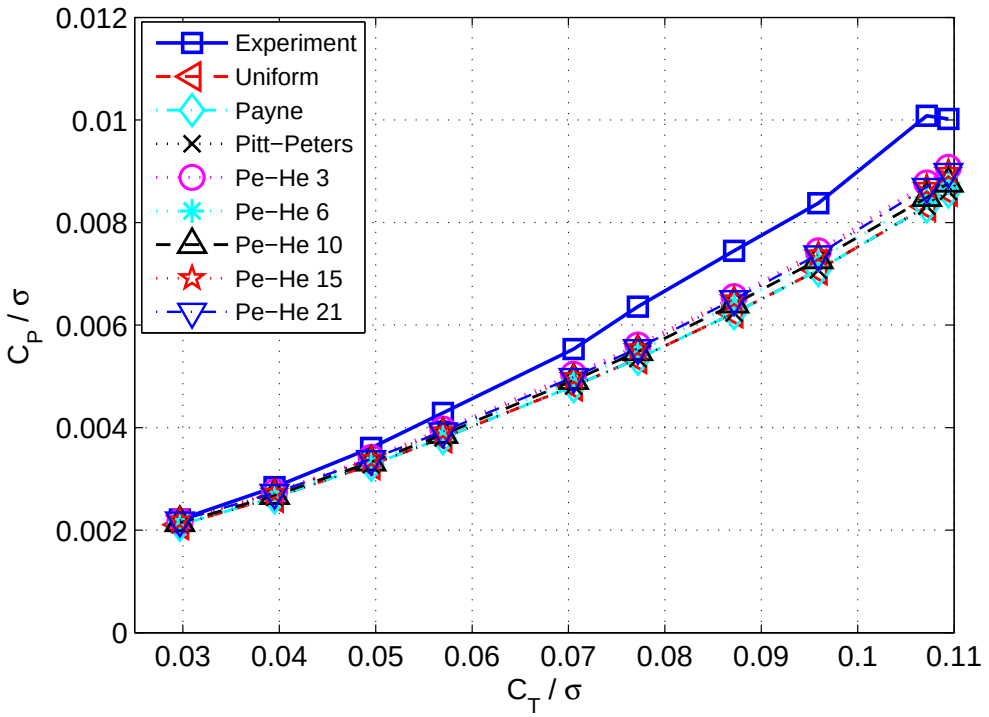

Figure 5.11: Normalized Power Coefficient vs Normalized Thrust Coefficient, at Hover, $\alpha_s = -15°$

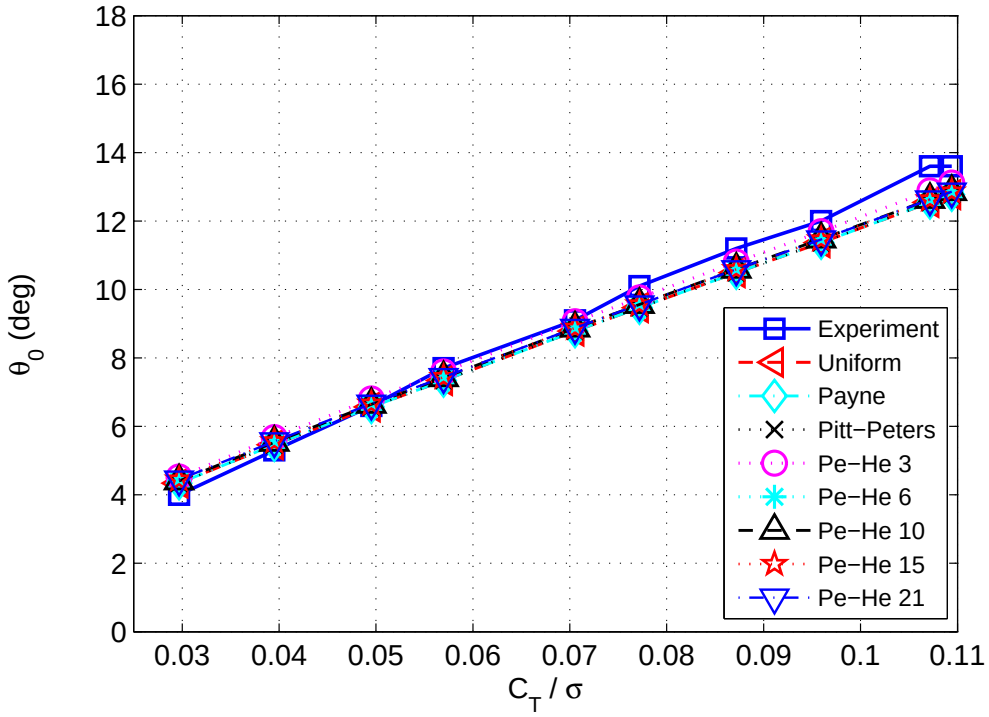

Figure 5.12: Collective Angle vs Normalized Thrust Coefficient, at Hover, $\alpha_s = -15°$

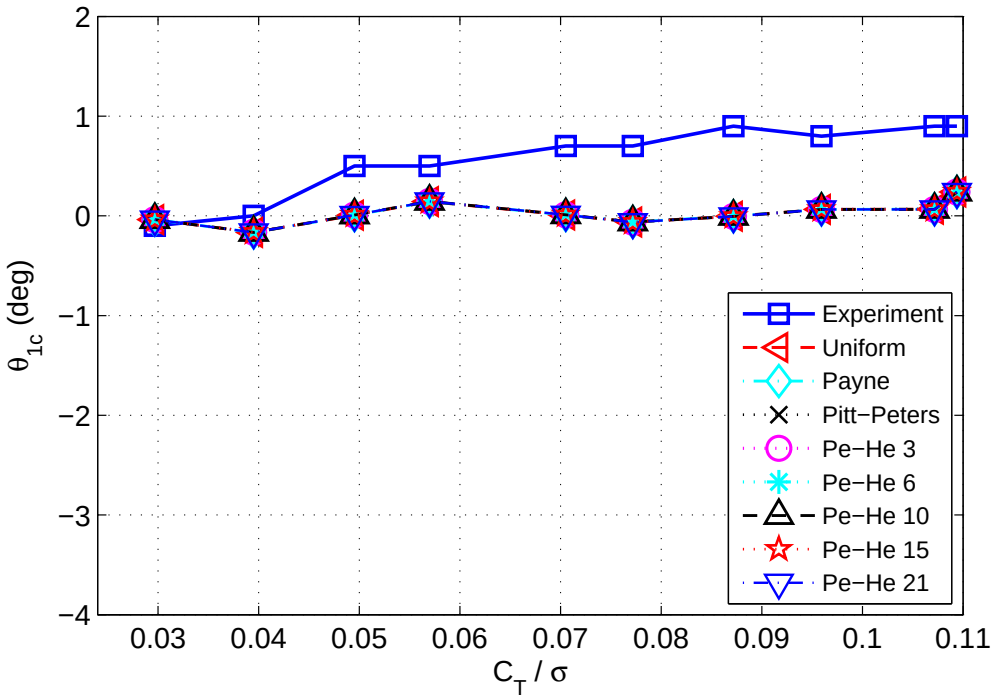

Figure 5.13: Lateral Cyclic Position vs Normalized Thrust Coefficient, at Hover, $\alpha_s = -15°$

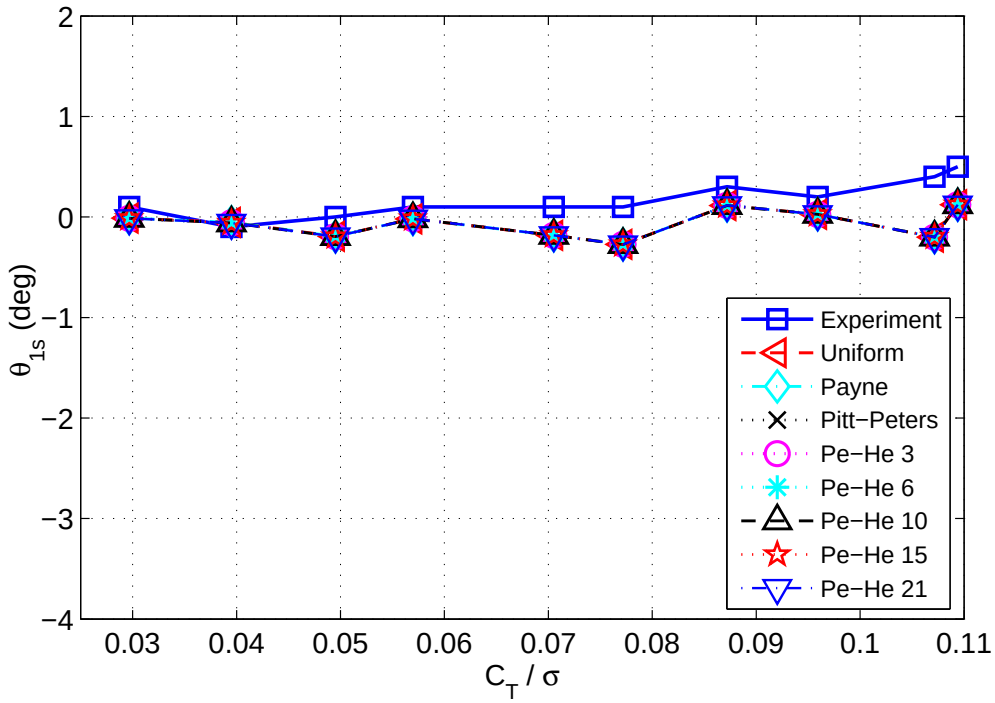

Figure 5.14: Longitudinal Cyclic Position vs Normalized Thrust Coefficient, at Hover, $\alpha_s = -15°$

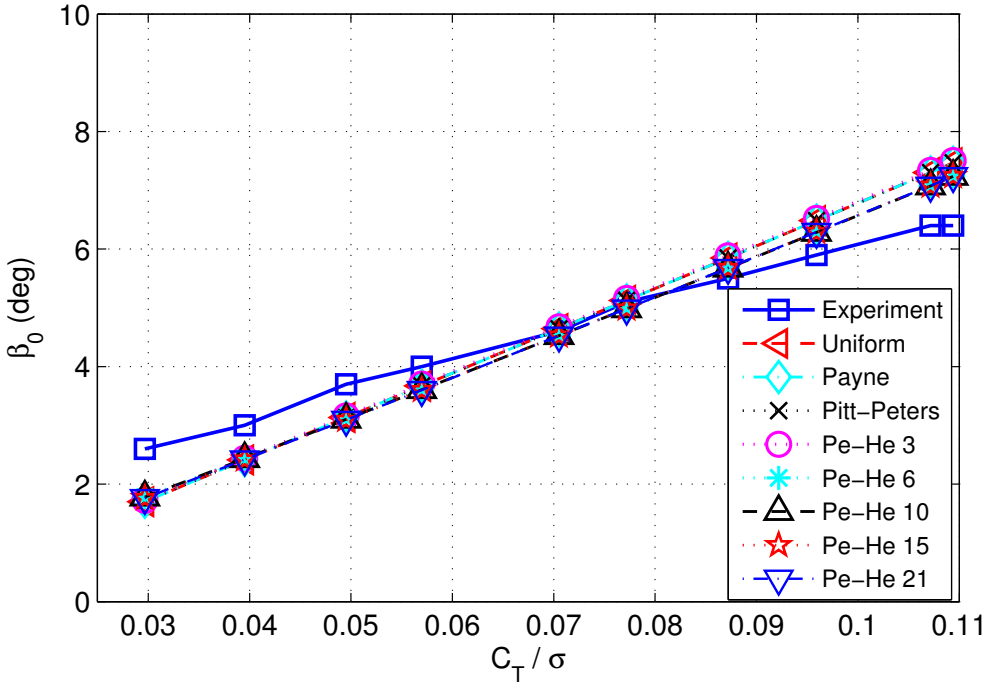

Figure 5.15: Coning Angle vs Normalized Thrust Coefficient, at Hover, $\alpha_s = -15°$

5.3.2 Forward Flight Performance

In this part, forward flight performance results are compared with the wind tunnel test data. Among various wind tunnel tests, two set of test conditions are selected for performance evaluation. In these tests, the advance ratio changes from 0.01 to 0.25 and rotor shaft angle is held constant at -5 degree. In the first test, normalized thrust is held at 0.065. In the second test, normalized thrust coefficient is increased to 0.080.

5.3.2.1 Speed Sweep, $\mathbf{C_T/\sigma = 0.065}$, $\mathbf{\alpha_s = -5°}$

The power estimation respect to advance ratio, μ, is given in Figure 5.16. Except Peters-He 15-State inflow, all models are close to each other and they show good agreement with the data throughout the speed range. When advance ratio is under 0.1, models do slight overestimation. After this advance ratio, predictions become comparatively closer to the experiment, except Peters-He 15-State. After the advance ratio of 0.15, Peters-He 15-State inflow model starts to diverge from other models and from the experiment. In high speed conditions, Peters-He 15-State inflow model has

excessive upwash at the front of the rotor and downwash at the rear side of the rotor. At the advance ratio of 0.2, inflow distributions are given at Figures 5.23, 5.24, 5.25 and 5.26. Effect of the inflow over the angle of attack can be examined from Figures 5.27, 5.28, 5.29 and 5.30. Figures 5.28 & 5.30 show that when blade pass through the retreating side, Peters-He 15-State inflow model has large angle of attack peak near the blade center. It also has rather large angle of attack at the tip of the advancing blade. In contrast to this large angle of attack regions, this inflow model has relatively low angle of attacks at the other regions. Therefore, compared to other models, Peters-He 15-State inflow model requires more power to provide same loading in high speed conditions.

Normalized drag force coefficient, C_X/σ, estimations are presented in Figure 5.17. Beneath the advance ratio of 0.1, considered models are close to each other. As speed decreases, models converge to a single line where they do slight overestimation respect to experiment. As free-stream velocity increases, models start to deviate from each other. In high speed, all models underpredict the experimental data. In this test case, higher state models such as Peters-He 10, 15 and 21-State have marginally worse results than the low state models.

Change in the side force is shown at Figure 5.18. In high speed conditions, inflow models have good correlation with the data, except the uniform inflow model. In the low advance ratio region, uniform inflow cannot correctly predict the side force and its trend. According to [24], inflow models which have a variation over the rotor disk can capture the low speed dynamics better than the uniform inflow. This phenomena is studied in detail at the Chapter 4. In the C_Y/σ predictions, Peters-He 10, 15 and 21-State models have better results than the other inflow models.

The low speed inflow distributions are displayed in Figures 5.31, 5.32, 5.33 and 5.34. Except the uniform inflow, models have similar longitudinal variation at the advance ratio of 0.08. Higher state models such as Peters-He 6, 10, 15 and 21-State show similarity along lateral axis. The low state inflow models do not have any lateral variation in this trimmed condition. In contrast to high speed flight, Peters-He 15-State model does not have excessive upwash and downwash in low advance ratio condition. In fact, at the advance ratio of 0.08, Peters-He 15 and 21-State inflow

models have similar induced flow field. In this forward flight test, along addition to inflow plots, angle of attack distributions are also presented in Figures 5.35, 5.36, 5.37 and 5.38. Since Peters-He 15 and 21-State show similarity in inflow distribution, their angle of attack distributions are also similar (Figs. 5.36 & 5.38).

Collective pitch predictions are compared with the experimental data in Figure 5.19. When advance ratio is below 0.05, inflow models have good agreement with the data. As speed increases towards to advance ratio of 0.15 , error between the models and the data become larger. Between 0.12 and 0.15 advance ratio, models have the maximum collective pitch error which is less than 1.2 degrees. Likewise the power case, Peters-He 15-State inflow model deviate from other models at high speed flights. Again, this model requires more collective pitch angle to provide same loading at high advance ratio.

Lateral cyclic predictions are similar to normalized side force coefficient results. Figure 5.20 presents lateral cyclic predictions throughout the speed range. In low advance ratio region, uniform inflow estimation has large error and it does not follow the experimental trend. Note that, in this region, other inflow models are close to experimental data and they seem to capture peak cyclic position. After the advance ratio of 0.08 (peak cyclic position), Payne, Pitt-Peters, Peters-He 3 and 6-State inflow models try to follow the reduced lateral cyclic position. However, Peters-He 10, 15 and 21-State inflow models become almost steady after the peak lateral cyclic input. In high speed region, low state inflow models have better correlation with the experimental cyclic position.

Figure 5.21 shows longitudinal cyclic estimations. Considered inflow models are close to experimental data up to advance ratio of 0.1. As free-stream velocity increases, longitudinal cyclic pitch also increases to stay in trimmed condition. Although models follow the experimental pitch trend throughout the speed range, offsets between predictions and the experiment become comparatively larger. In high speed conditions, models except the Peters-He 10 and 21-State have similar predictions. Peters-He 10 and 21-State inflow models have comparably larger errors than the other models. In longitudinal cyclic estimations, the maximum error occurs at the highest speed and it is less than 2 degrees.

In this experiment C_T/σ is fixed at 0.065. Since coning angle is directly connected to loading, it can be expected to have a constant coning angle throughout the speed range. In fact, Figure 5.21 shows that coning angle is held around 4 degree. Although considered models do slight overestimation under the advance ratio of 0.1, they have good correlation with the data. As speed increases, models slightly deviate from each other. High state models such as Peters-He 15, 10 and 21-State have relatively better results at the high advance ratio. The experiment indicates that effect of free-stream velocity on coning angle is insignificant. However, free-stream velocity affects the theoretical inflow, therefore model predictions show dependence on free-stream velocity. The maximum error in this case is less than 0.4 degree.

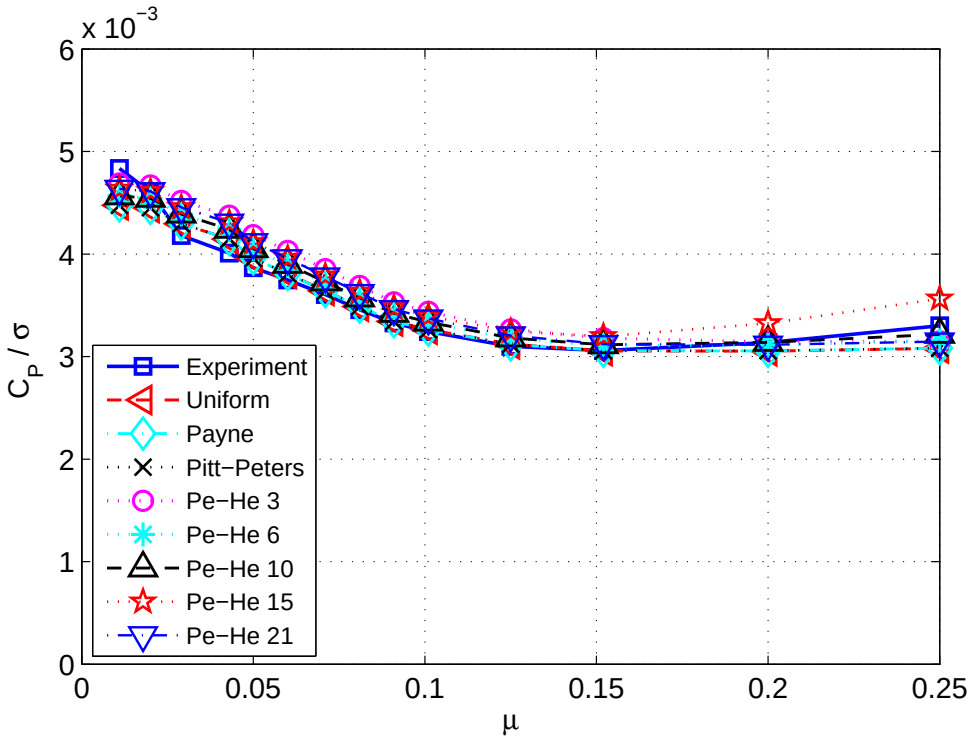

Figure 5.16: Normalized Power Coefficient vs Advance Ratio, at $C_T/\sigma = 0.065$, $\alpha_s = -5^\circ$

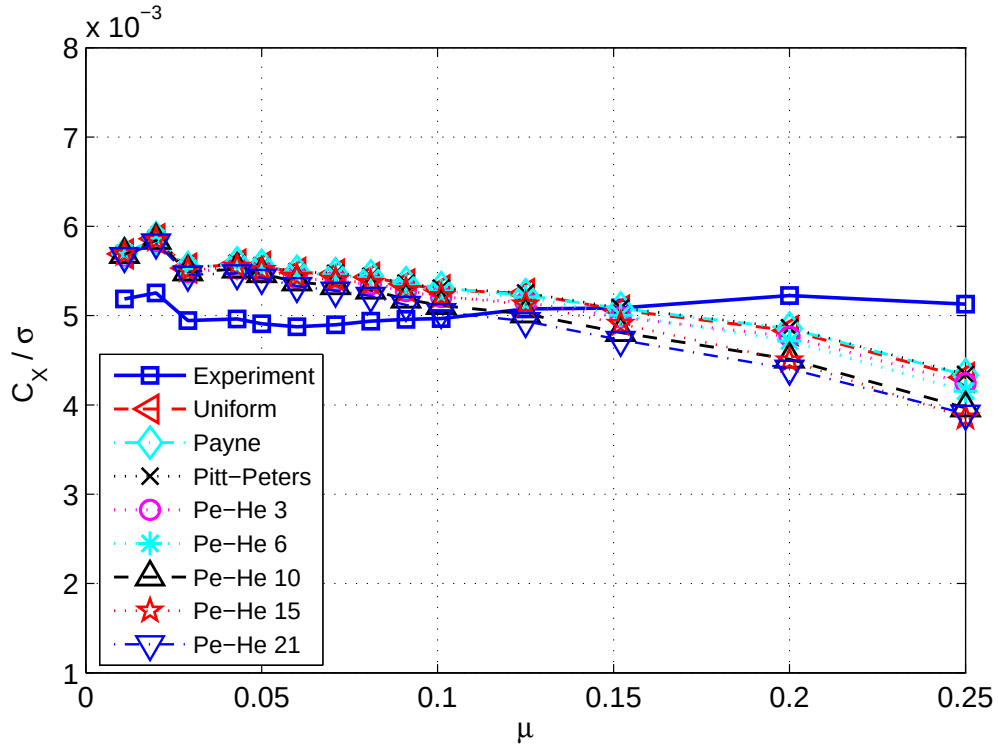

Figure 5.17: Normalized Drag Force Coefficient vs Advance Ratio, at $C_T/\sigma = 0.065$, $\alpha_s = -5°$

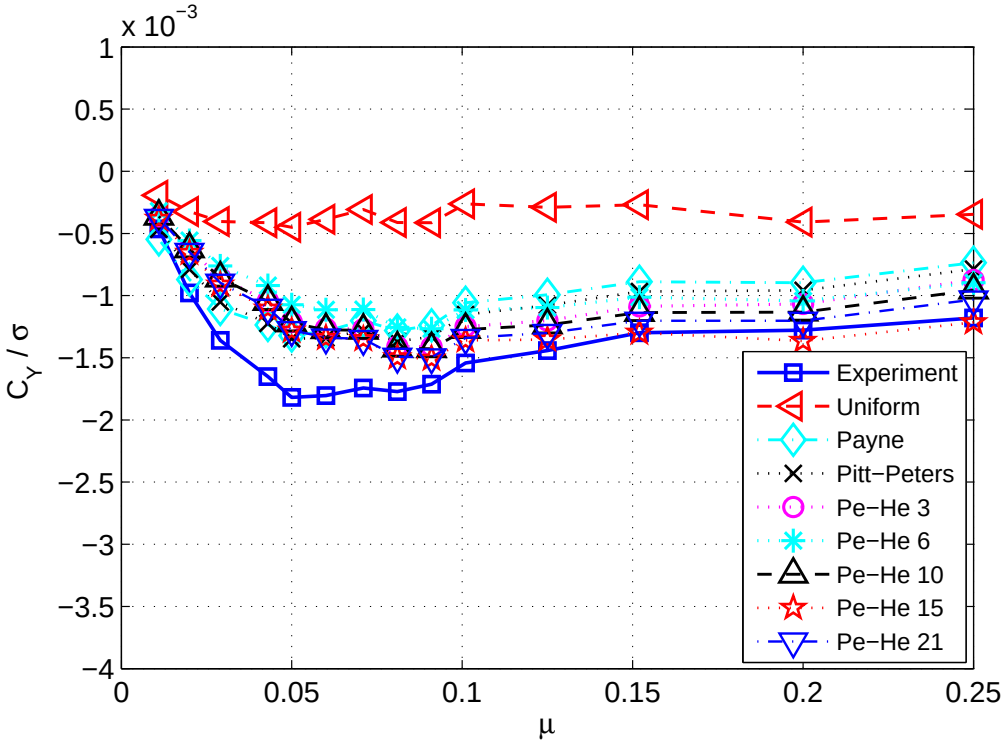

Figure 5.18: Normalized Side Force Coefficient vs Advance Ratio, at $C_T/\sigma = 0.065$, $\alpha_s = -5°$

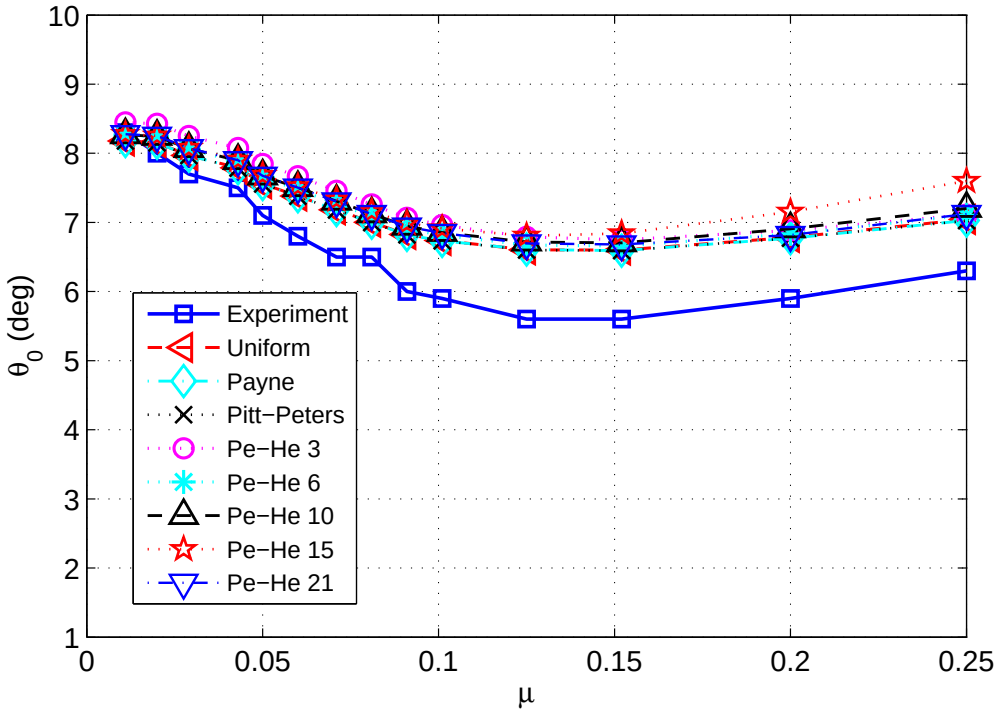

Figure 5.19: Collective Angle vs Advance Ratio, at $C_T/\sigma = 0.065$, $\alpha_s = -5°$

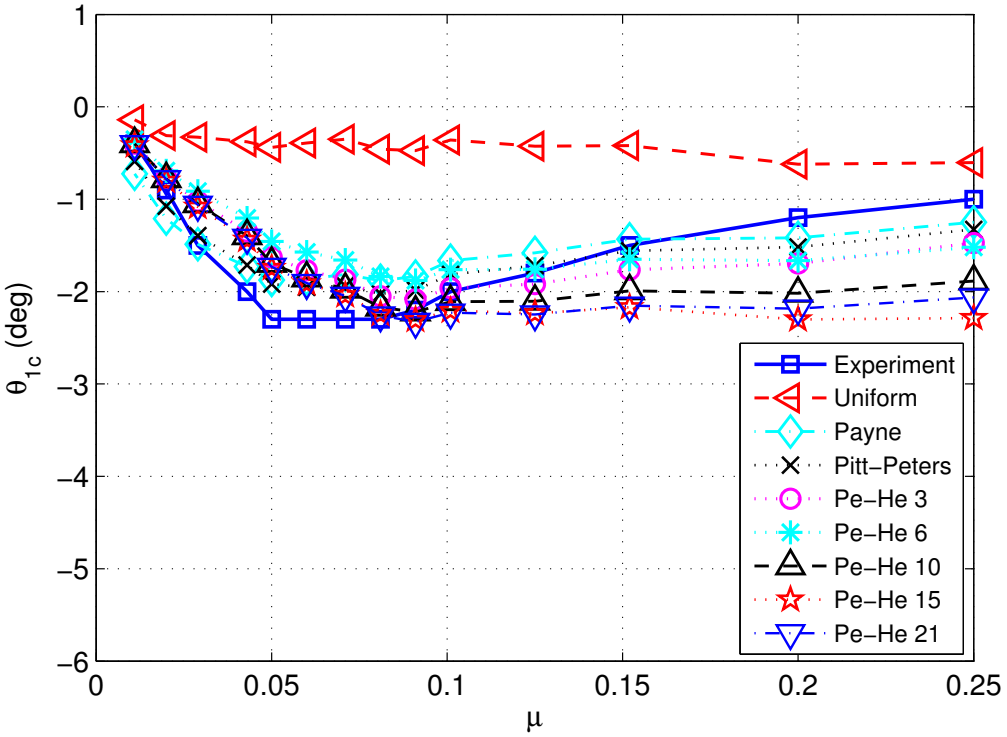

Figure 5.20: Lateral Cyclic Position vs Advance Ratio, at $C_T/\sigma = 0.065$, $\alpha_s = -5°$

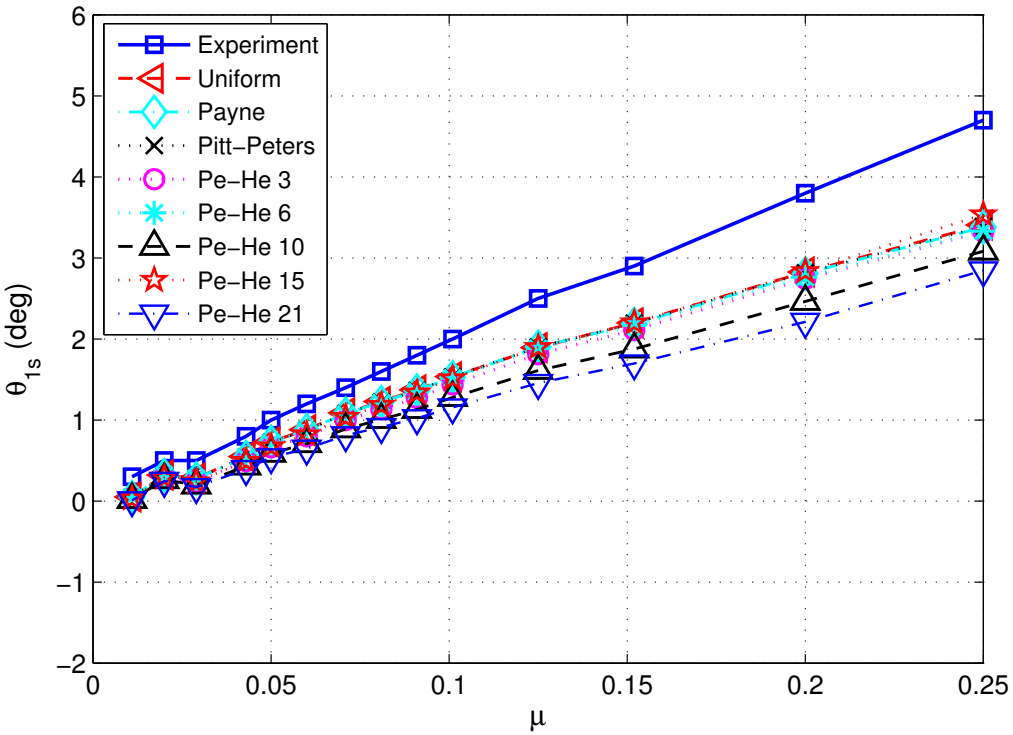

Figure 5.21: Longitudinal Cyclic Position vs Advance Ratio, at $C_T/\sigma = 0.065$, $\alpha_s = -5°$

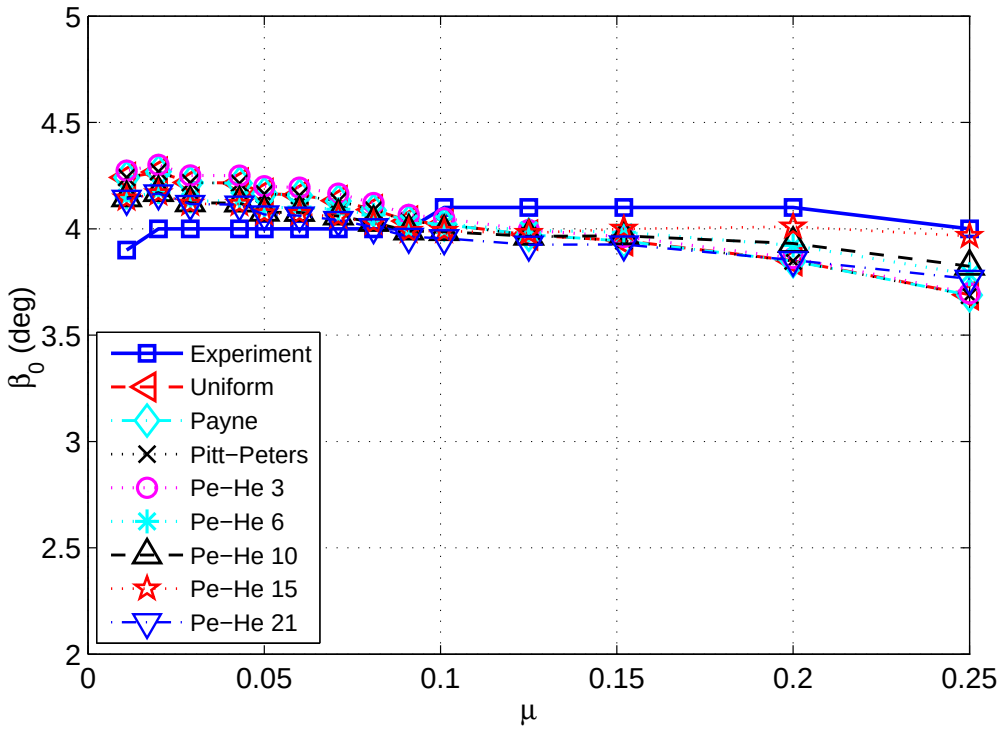

Figure 5.22: Coning Angle vs Advance Ratio, at $C_T/\sigma = 0.065$, $\alpha_s = -5°$

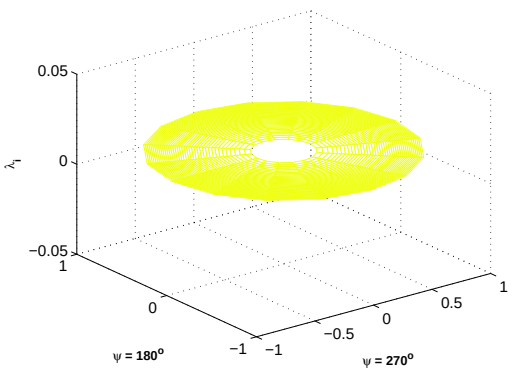

(a) Dynamic Uniform

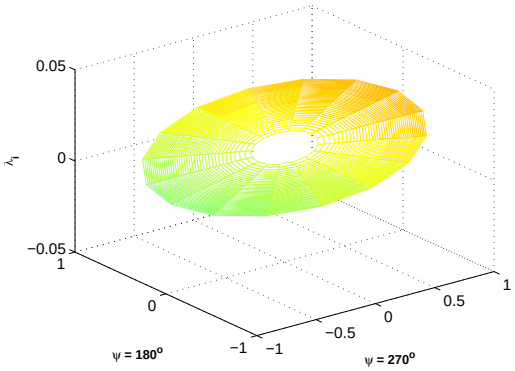

(b) Payne

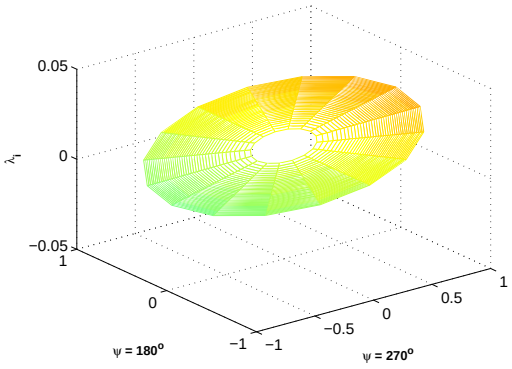

(c) Pitt-Peters

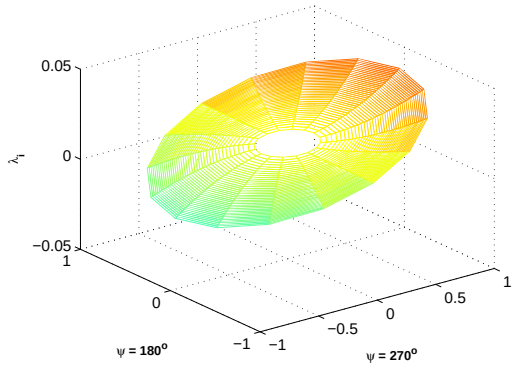

(d) Peters-He 3-State

Figure 5.23: Uniform, Payne, Pitt-Peters & Peters-He 3 State Induced Flow 3-D Plots, at Forward Speed, $\alpha_s = -5°$, $\mu = 0.2$, $C_T/\sigma = 0.065$

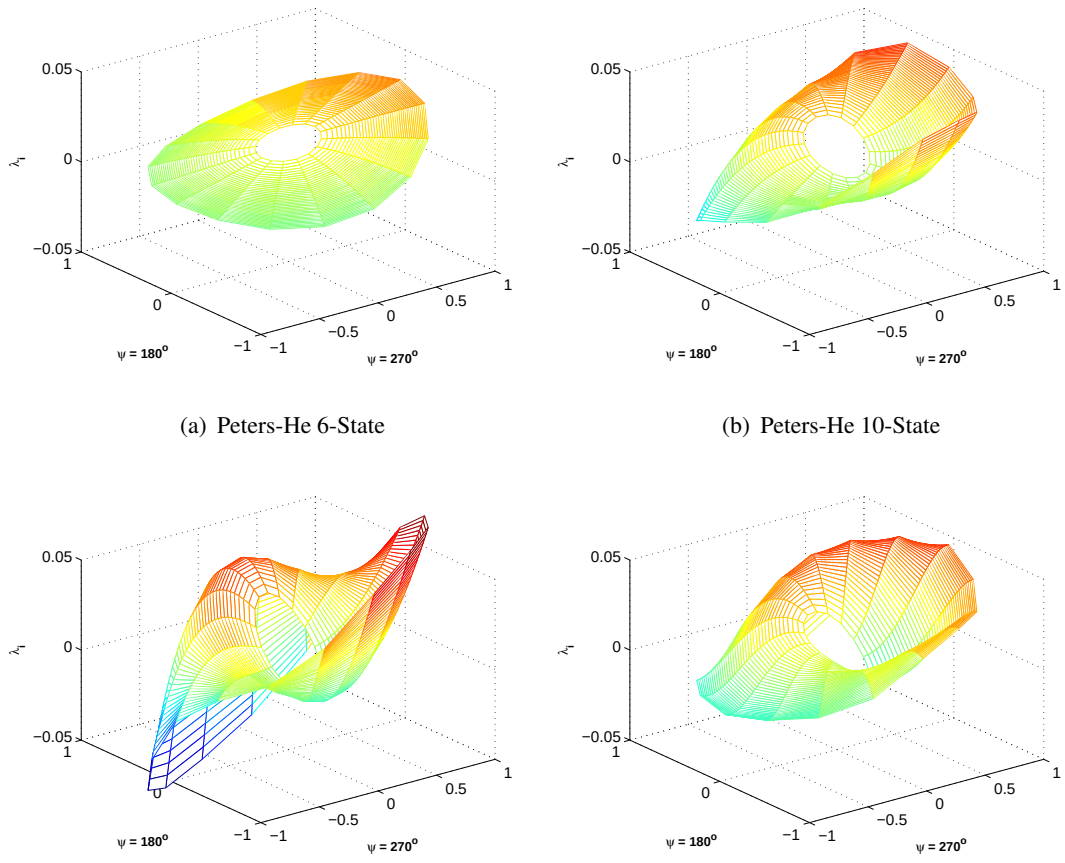

(a) Peters-He 6-State

(b) Peters-He 10-State

(c) Peters-He 15-State

(d) Peters-He 21-State

Figure 5.24: Peters-He 6, 10, 15 & 21 State Induced Flow 3-D Plots, at Forward Speed, $\alpha_s = -5°$, $\mu = 0.2$, $C_T/\sigma = 0.065$

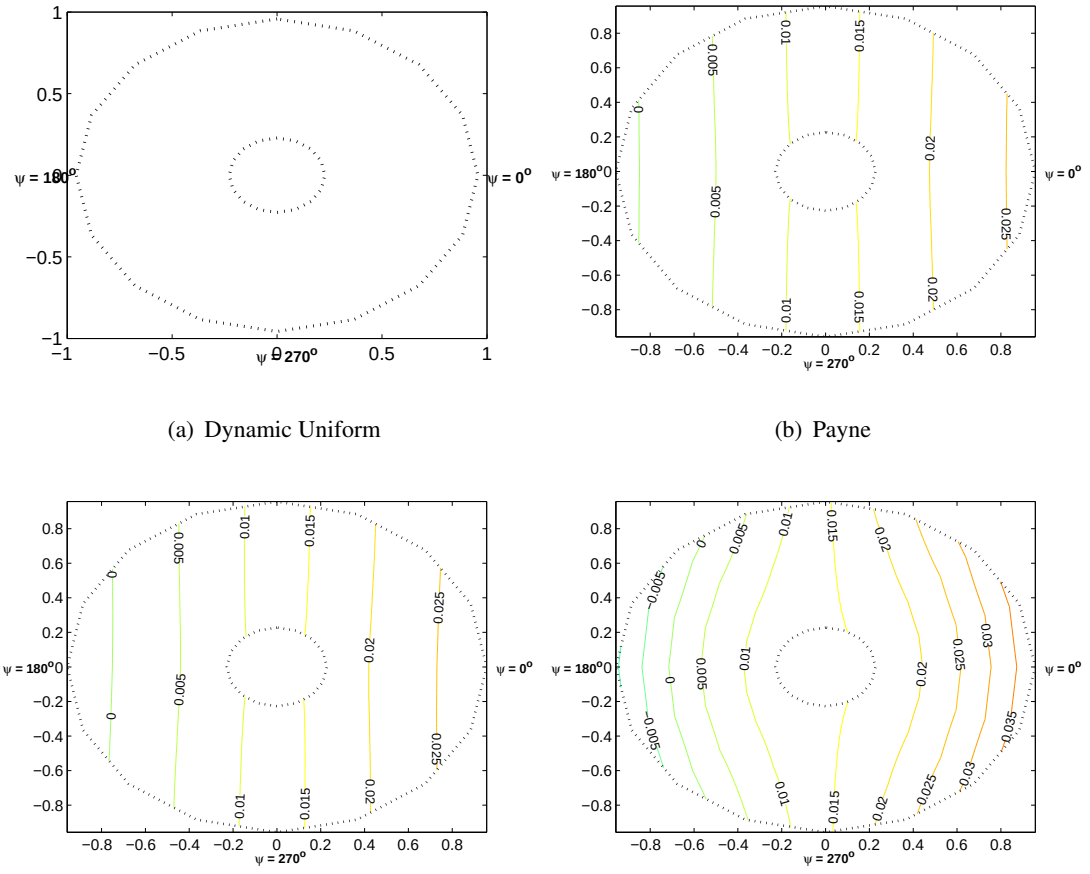

(a) Dynamic Uniform

(b) Payne

(c) Pitt-Peters

(d) Peters-He 3-State

Figure 5.25: Uniform, Payne, Pitt-Peters & Peters-He 3 State Induced Flow Contour Plots, at Forward Speed, $\alpha_s = -5°$, $\mu = 0.2$, $C_T/\sigma = 0.065$

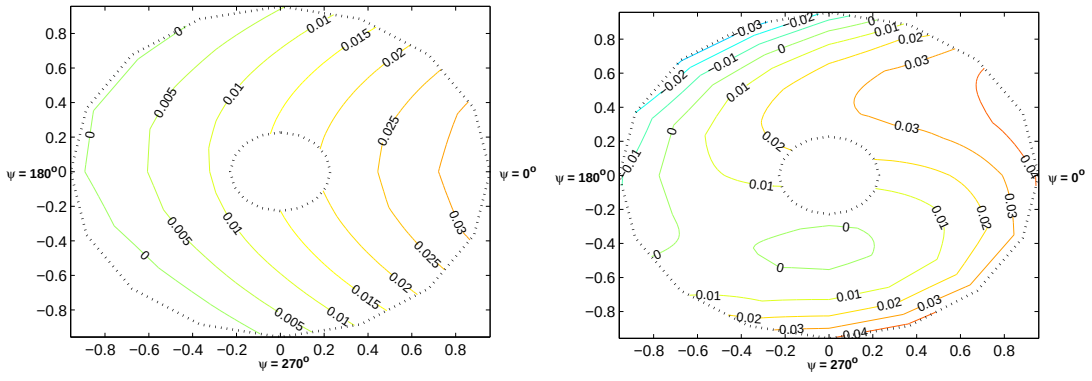

(a) Peters-He 6-State

(b) Peters-He 10-State

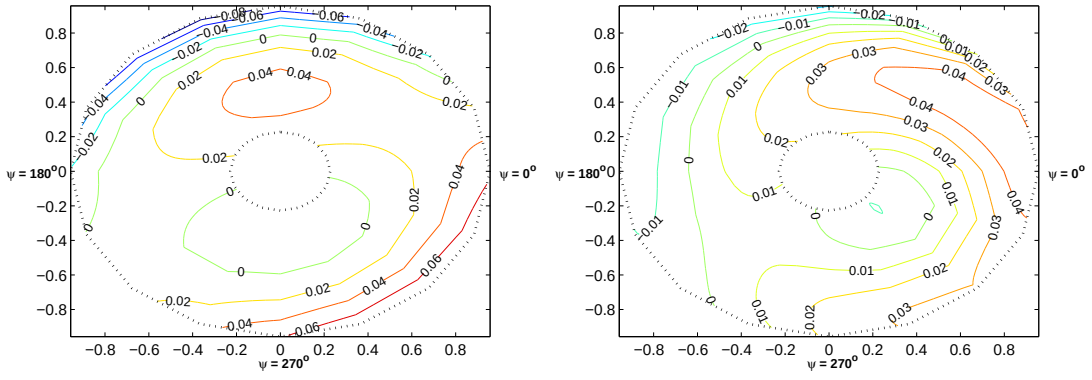

(c) Peters-He 15-State

(d) Peters-He 21-State

Figure 5.26: Peters-He 6, 10, 15 & 21 State Induced Flow Contour Plots, at Forward Speed, $\alpha_s = -5°$, $\mu = 0.2$, $C_T/\sigma = 0.065$

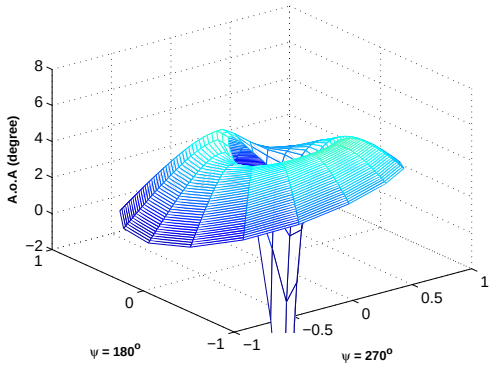

(a) Dynamic Uniform

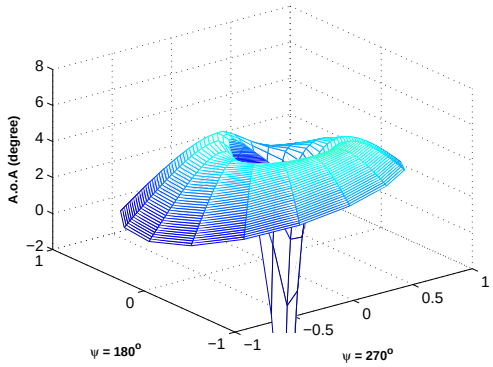

(b) Payne

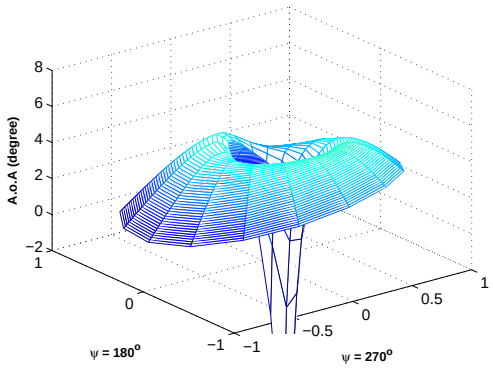

(c) Pitt-Peters

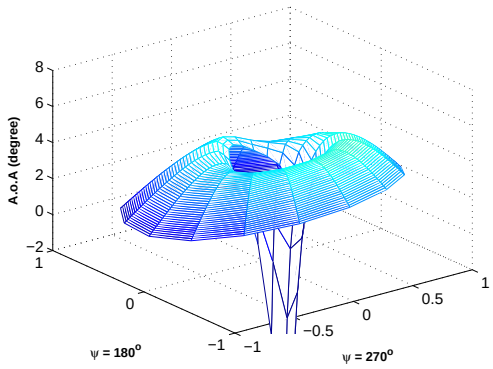

(d) Peters-He 3-State

Figure 5.27: Uniform, Payne, Pitt-Peters & Peters-He 3 State Angle of Attack 3-D Plots, at Forward Speed, $\alpha_s = -5°$, $\mu = 0.2$, $C_T/\sigma = 0.065$

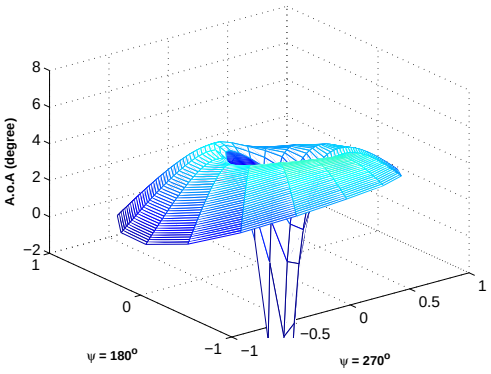

(a) Peters-He 6-State

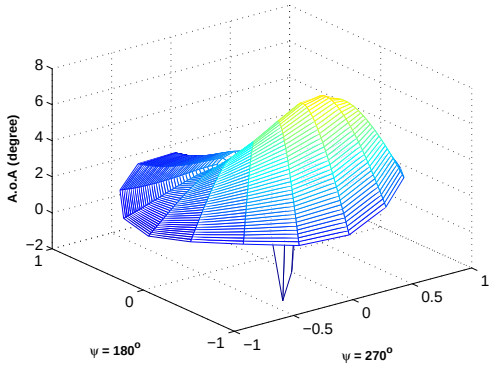

(b) Peters-He 10-State

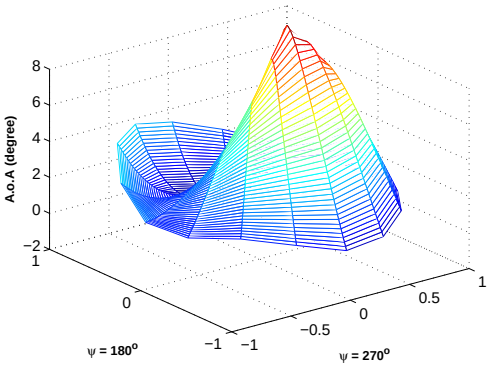

(c) Peters-He 15-State

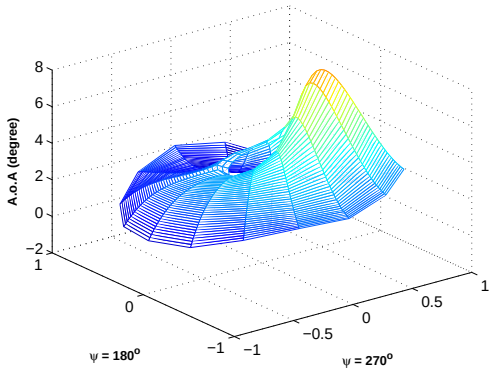

(d) Peters-He 21-State

Figure 5.28: Peters-He 6, 10, 15 & 21 State Angle of Attack 3-D Plots, at Forward Speed, $\alpha_s = -5°$, $\mu = 0.2$, $C_T/\sigma = 0.065$

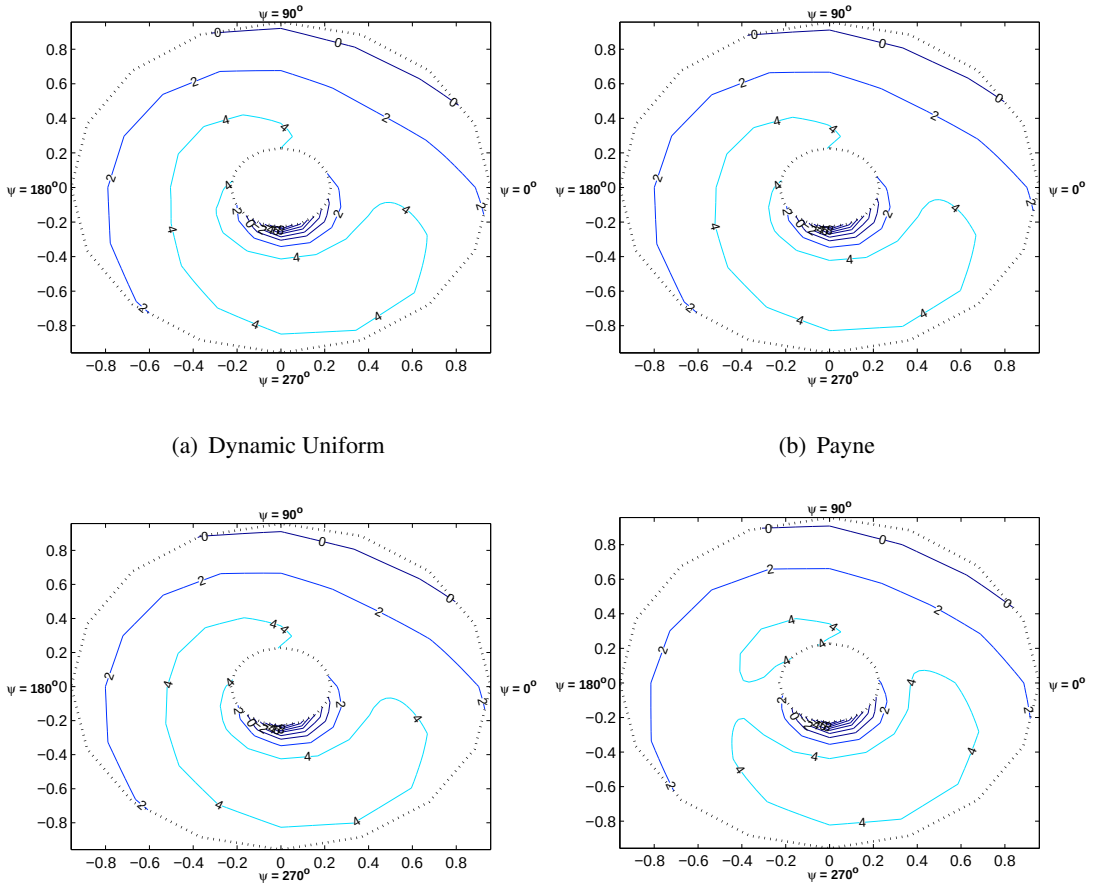

(a) Dynamic Uniform

(b) Payne

(c) Pitt-Peters

(d) Peters-He 3-State

Figure 5.29: Uniform, Payne, Pitt-Peters & Peters-He 3 State Angle of Attack Contour Plots, at Forward Speed, $\alpha_s = -5°$, $\mu = 0.2$, $C_T/\sigma = 0.065$

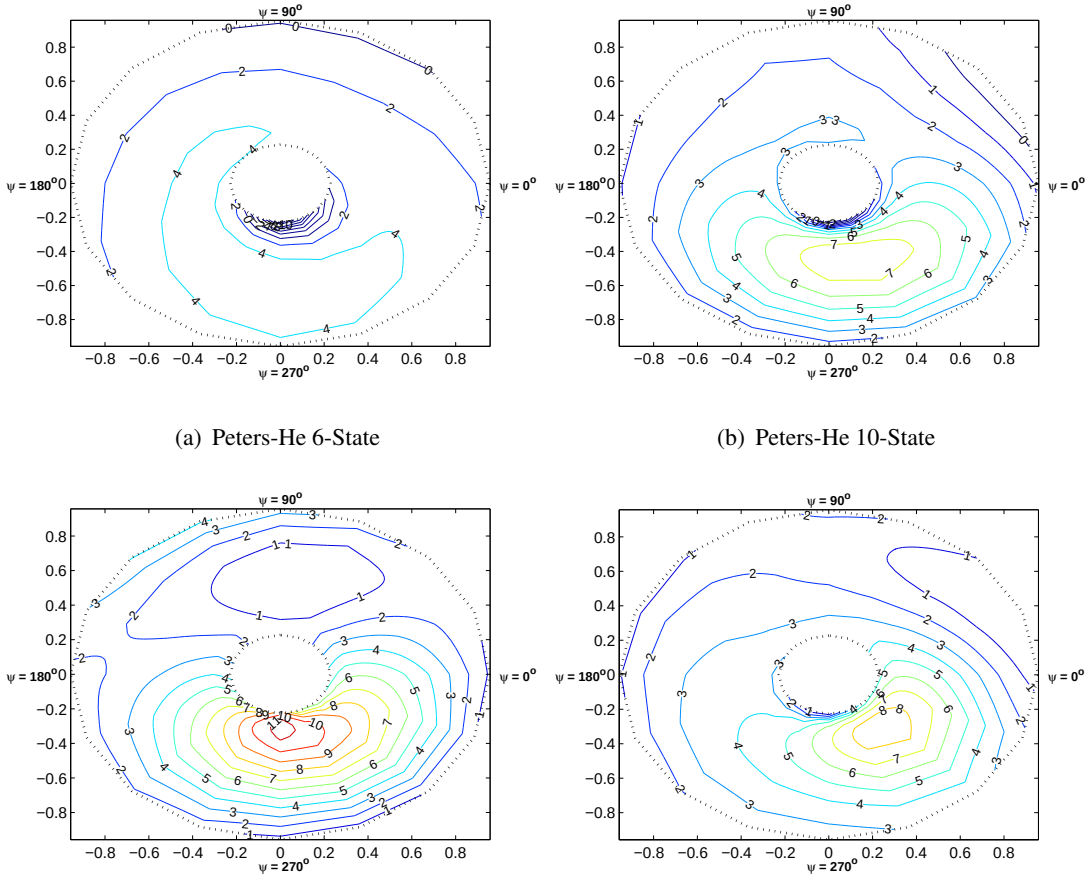

(a) Peters-He 6-State

(b) Peters-He 10-State

(c) Peters-He 15-State

(d) Peters-He 21-State

Figure 5.30: Peters-He 6, 10, 15 & 21 State Angle of Attack Contour Plots, at Forward Speed, $\alpha_s = -5°$, $\mu = 0.2$, $C_T/\sigma = 0.065$

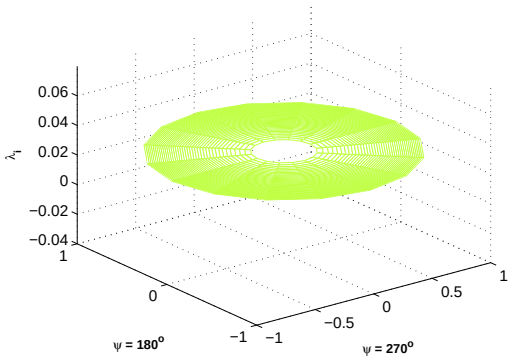

(a) Dynamic Uniform

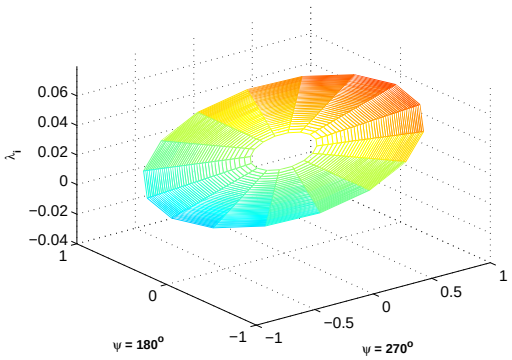

(b) Payne

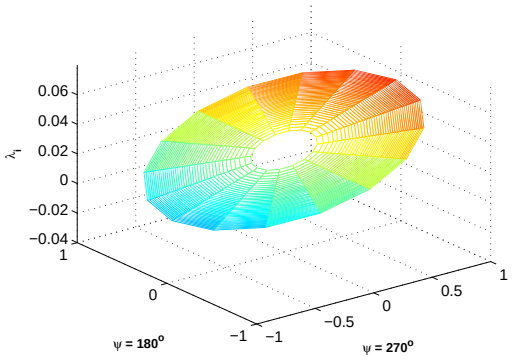

(c) Pitt-Peters

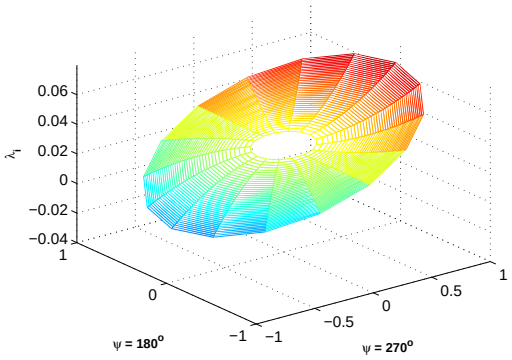

(d) Peters-He 3-State

Figure 5.31: Uniform, Payne, Pitt-Peters & Peters-He 3 State Induced Flow 3-D Plots, at Forward Speed, $\alpha_s = -5°$, $\mu = 0.08$, $C_T/\sigma = 0.065$

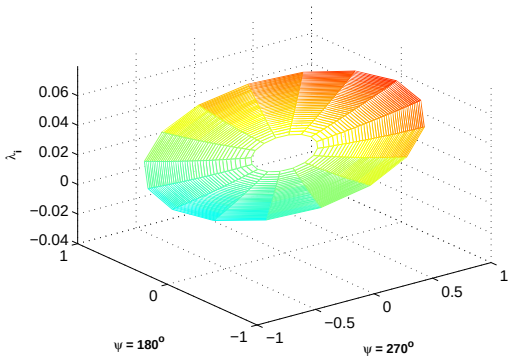

(a) Peters-He 6-State

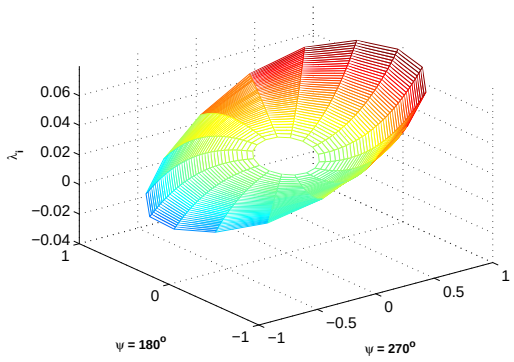

(b) Peters-He 10-State

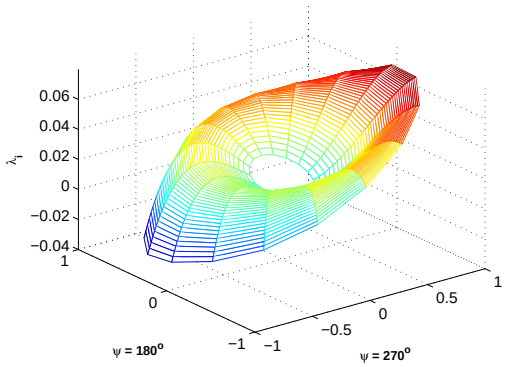

(c) Peters-He 15-State

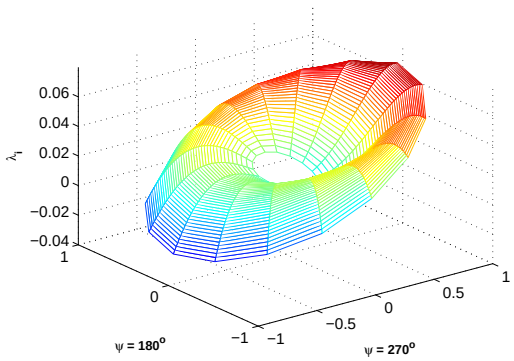

(d) Peters-He 21-State

Figure 5.32: Peters-He 6, 10, 15 & 21 State Induced Flow 3-D Plots, at Forward Speed, $\alpha_s = -5°$, $\mu = 0.08$, $C_T/\sigma = 0.065$

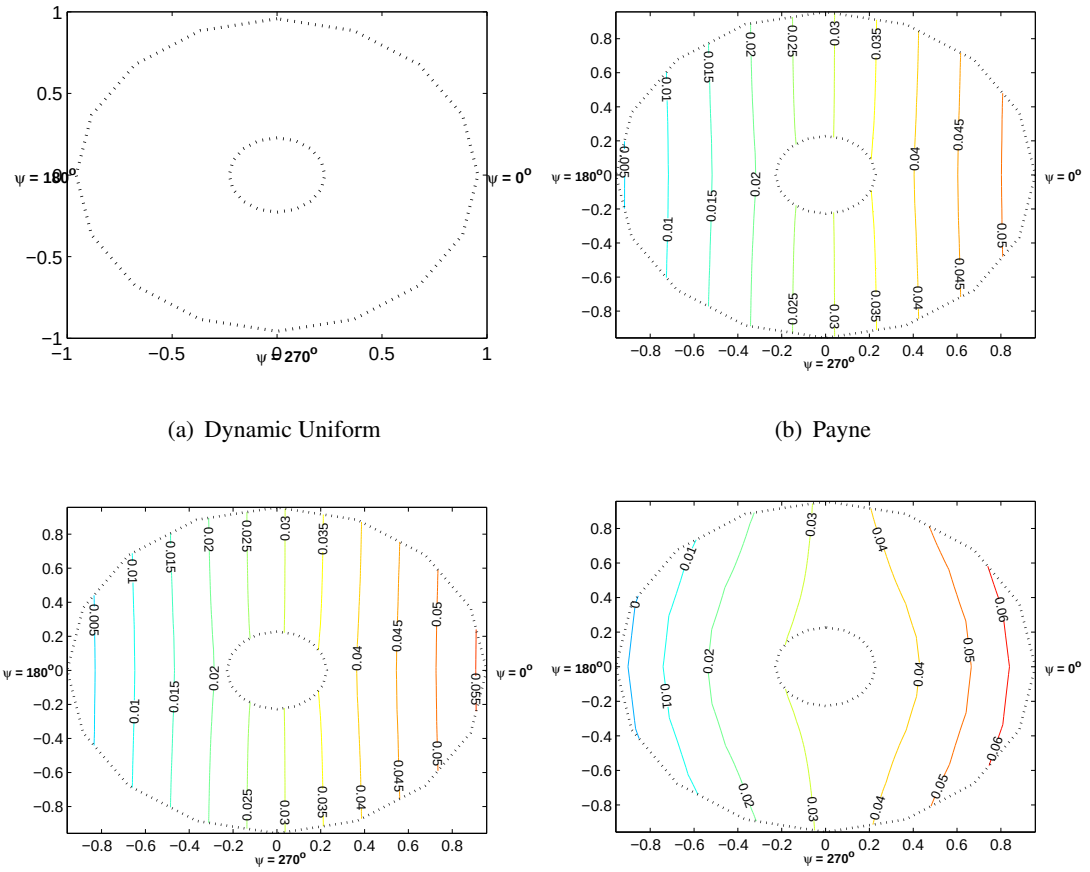

(a) Dynamic Uniform

(b) Payne

(c) Pitt-Peters

(d) Peters-He 3-State

Figure 5.33: Uniform, Payne, Pitt-Peters & Peters-He 3 State Induced Flow Contour Plots, at Forward Speed, $\alpha_s = -5°$, $\mu = 0.08$, $C_T/\sigma = 0.065$

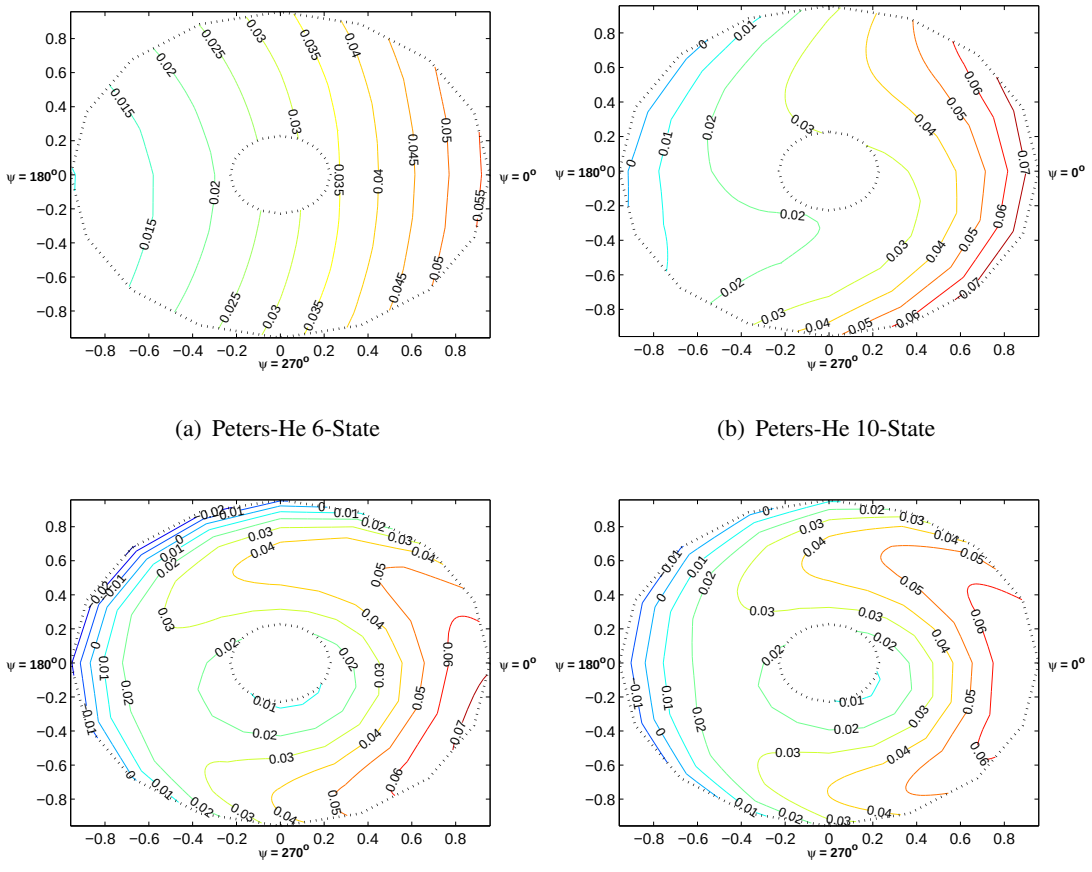

(a) Peters-He 6-State

(b) Peters-He 10-State

(c) Peters-He 15-State

(d) Peters-He 21-State

Figure 5.34: Peters-He 6, 10, 15 & 21 State Induced Flow Contour Plots, at Forward Speed, $\alpha_s = -5°$, $\mu = 0.2$, $C_T/\sigma = 0.065$

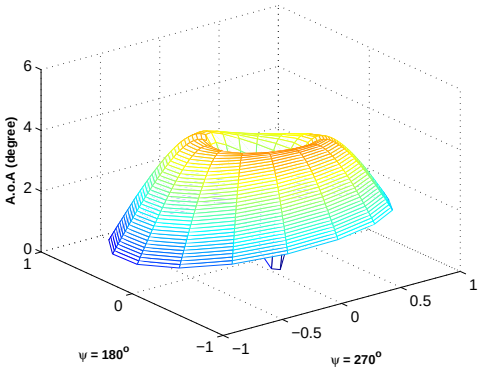

(a) Dynamic Uniform

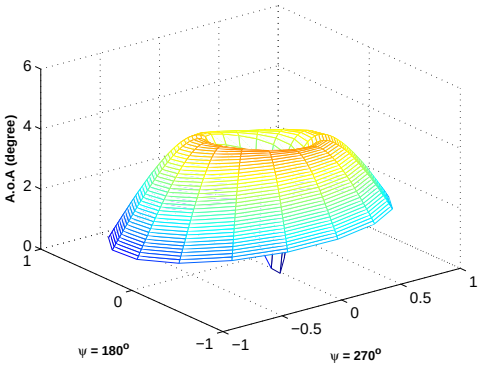

(b) Payne

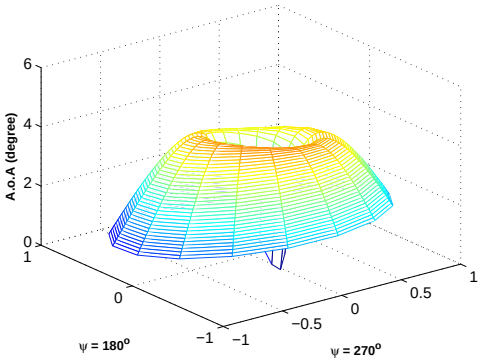

(c) Pitt-Peters

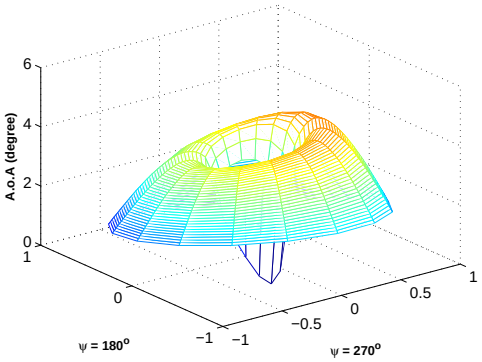

(d) Peters-He 3-State

Figure 5.35: Uniform, Payne, Pitt-Peters & Peters-He 3 State Angle of Attack 3-D Plots, at Forward Speed, $\alpha_s = -5°$, $\mu = 0.08$, $C_T/\sigma = 0.065$

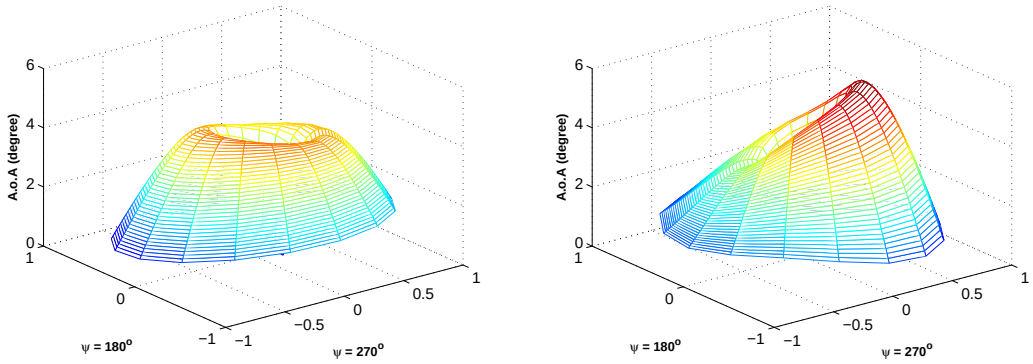

(a) Peters-He 6-State

(b) Peters-He 10-State

(c) Peters-He 15-State

(d) Peters-He 21-State

Figure 5.36: Peters-He 6, 10, 15 & 21 State Angle of Attack 3-D Plots, at Forward Speed, $\alpha_s = -5°$, $\mu = 0.08$, $C_T/\sigma = 0.065$

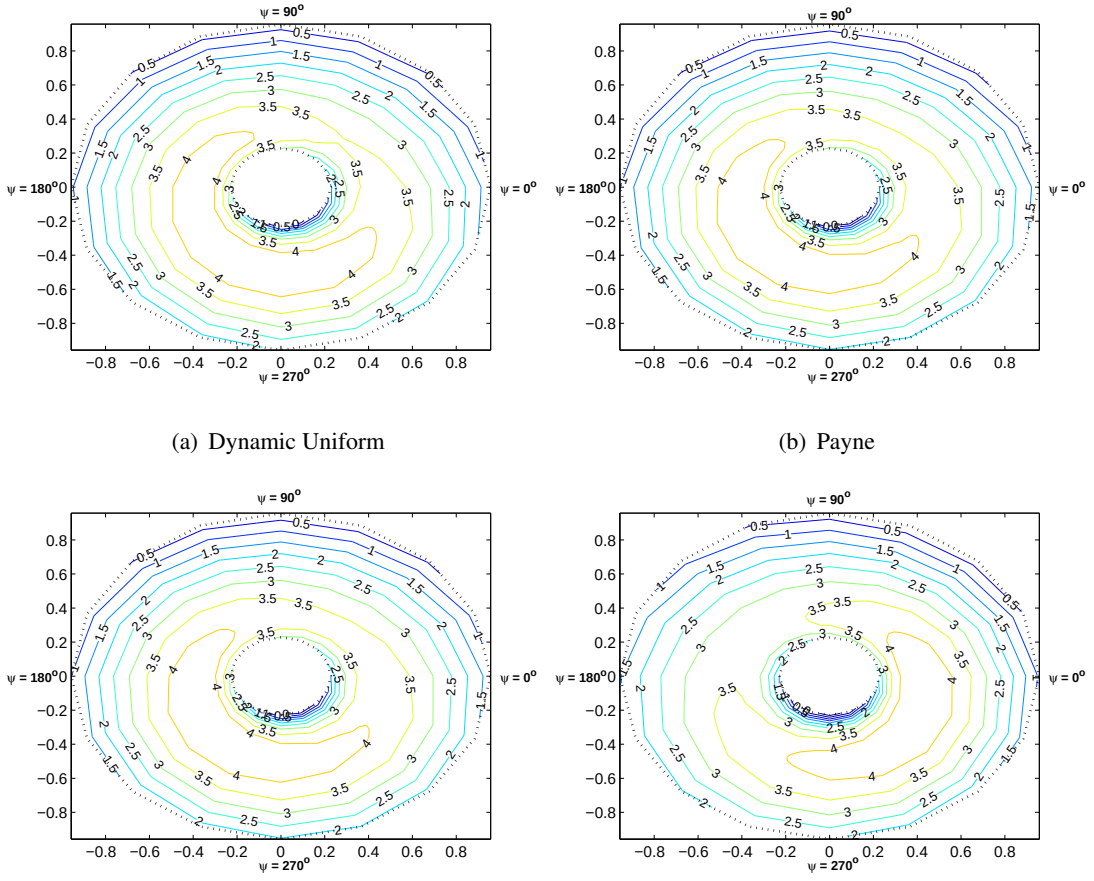

(a) Dynamic Uniform

(b) Payne

(c) Pitt-Peters

(d) Peters-He 3-State

Figure 5.37: Uniform, Payne, Pitt-Peters & Peters-He 3 State Angle of Attack Contour Plots, at Forward Speed, $\alpha_s = -5°$, $\mu = 0.08$, $C_T/\sigma = 0.065$

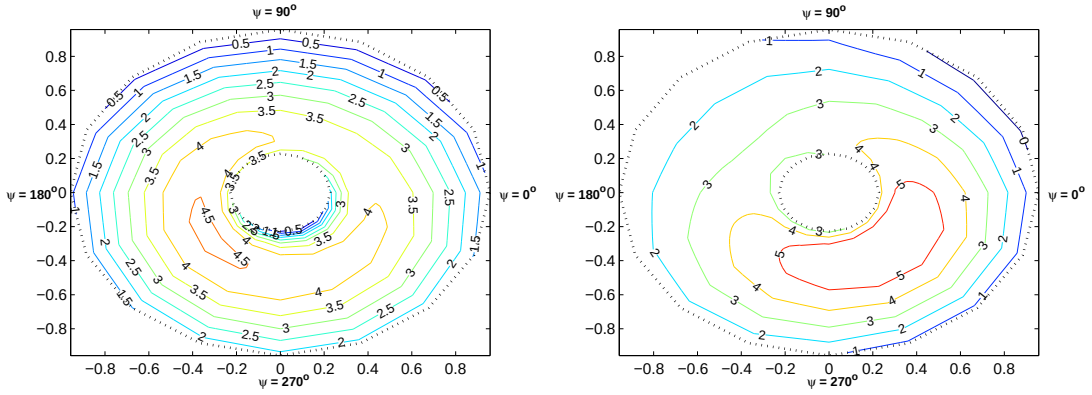

(a) Peters-He 6-State

(b) Peters-He 10-State

(c) Peters-He 15-State

(d) Peters-He 21-State

Figure 5.38: Peters-He 6, 10, 15 & 21 State Angle of Attack Contour Plots, at Forward Speed, $\alpha_s = -5°$, $\mu = 0.08$, $C_T/\sigma = 0.065$

5.3.2.2 Speed Sweep, $\mathbf{C_T/\sigma = 0.080}$, $\alpha_s = -5^\circ$

In this forward flight test condition, normalized thrust coefficient, C_T/σ, is increased from 0.065 to 0.080. Apart from normalized drag force coefficient and coning angle, other performance results such as power, side force, collective pitch angle, lateral cyclic and longitudinal cyclic positions have common results. These common results are given in Figures 5.39, 5.41, 5.42, 5.43 & 5.44. Since results are close to previous case, inflow and angle of attack distributions are not presented.

Normalized drag force coefficient predictions are plotted in Figure 5.40. C_X/σ estimations have good agreement with the data up to the advance ratio of 0.08. After this point, inflow models do not follow the experimental drag. As speed increases, error between models and the data become wider. Peters-He 10, 15 & 21-State inflow models have comparably worse predictions than the other considered models.

In Figure 5.45, coning angle, β_0, correlations are given. All models overpredict the experimental coning angle. The low state inflow models such as uniform, Payne, Pitt-Peters and Peters-He 3-State are close to each other and they have slightly more overprediction than the high state models. After the advance ratio of 0.1, models become closer the data. Except the Peters-He 15-State inflow model, other models follow the same trend towards the higher speeds. Peters-He 15-State inflow model is deviated from other models after the advance ratio of 0.15. Also, it slightly overestimates the experimental coning angle. Peters-He 15-State inflow model requires more collective pitch or power to provide same loading in high speed flight. This phenomena explained at the previous forward flight test case. Other models, especially Peters-He 10 and 21-State, have good agreement with the data in high speed conditions.

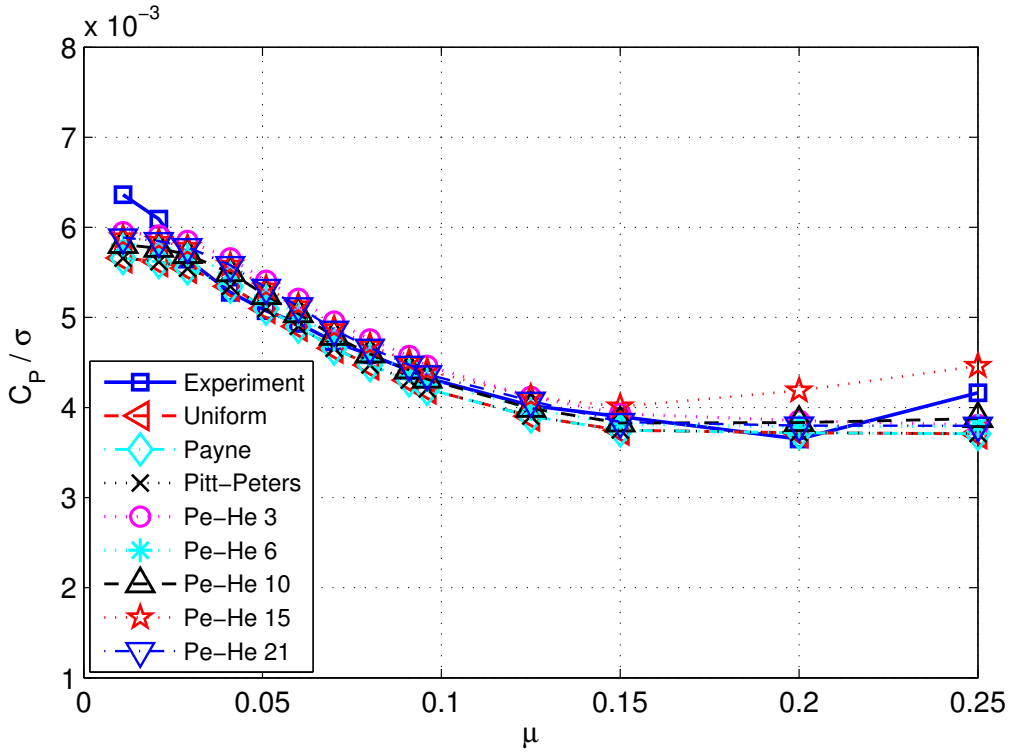

Figure 5.39: Normalized Power Coefficient vs Advance Ratio, at $C_T/\sigma = 0.080$, $\alpha_s = -5°$

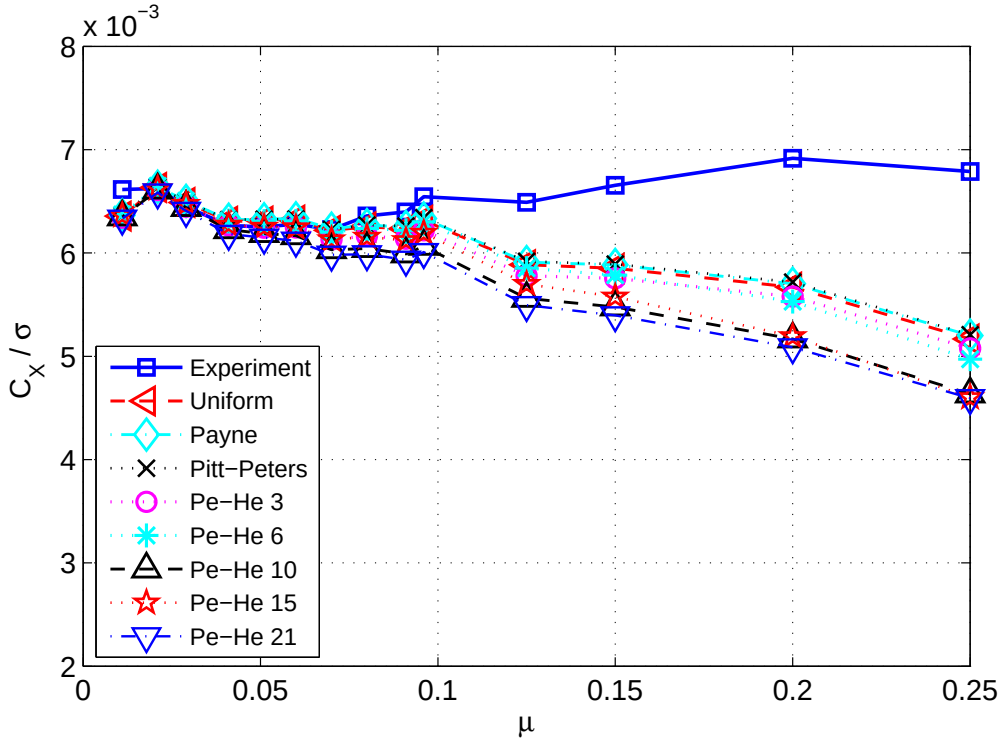

Figure 5.40: Normalized Drag Force Coefficient vs Advance Ratio, at $C_T/\sigma = 0.080$, $\alpha_s = -5°$

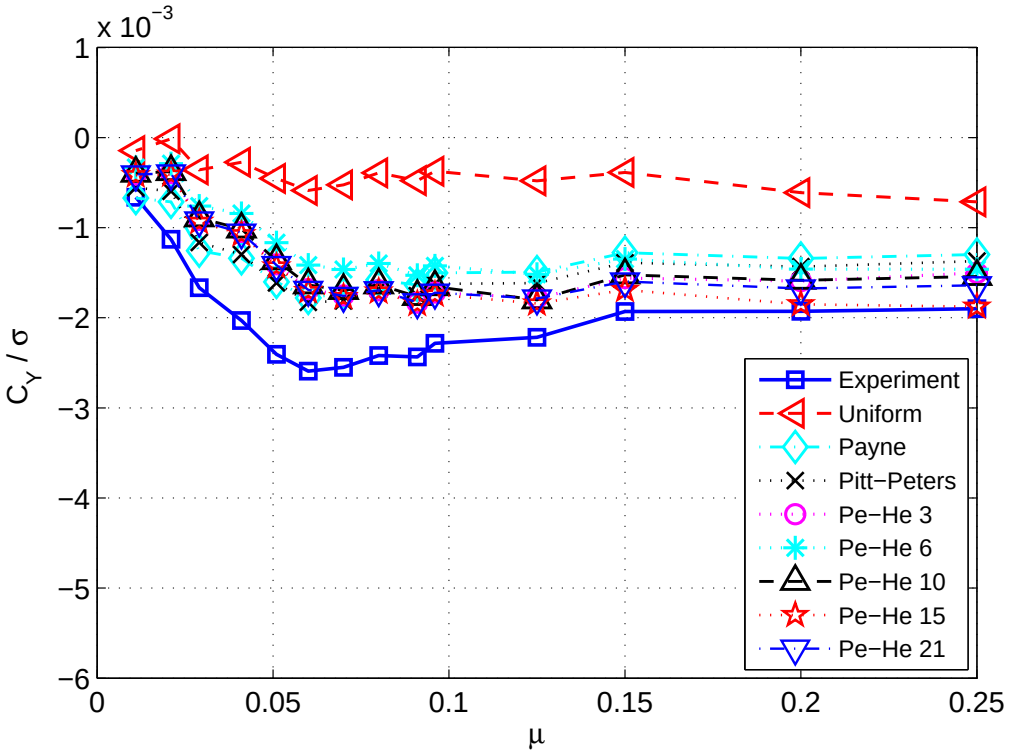

Figure 5.41: Normalized Side Force Coefficient vs Advance Ratio, at $C_T/\sigma = 0.080$, $\alpha_s = -5°$

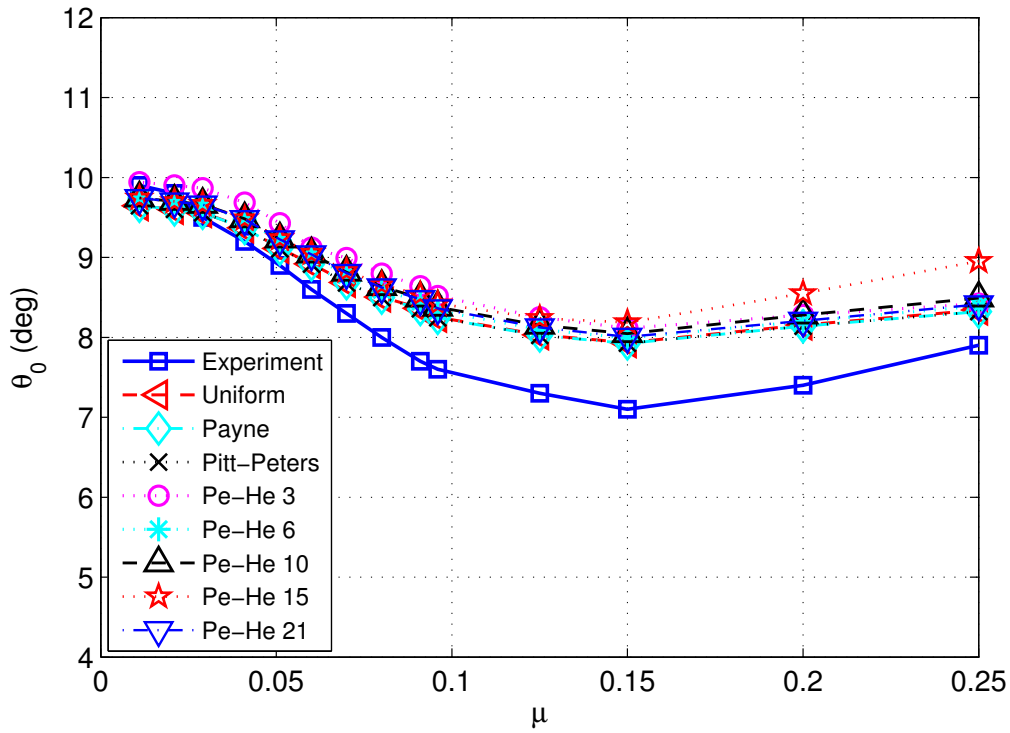

Figure 5.42: Collective Angle vs Advance Ratio, at $C_T/\sigma = 0.080$, $\alpha_s = -5°$

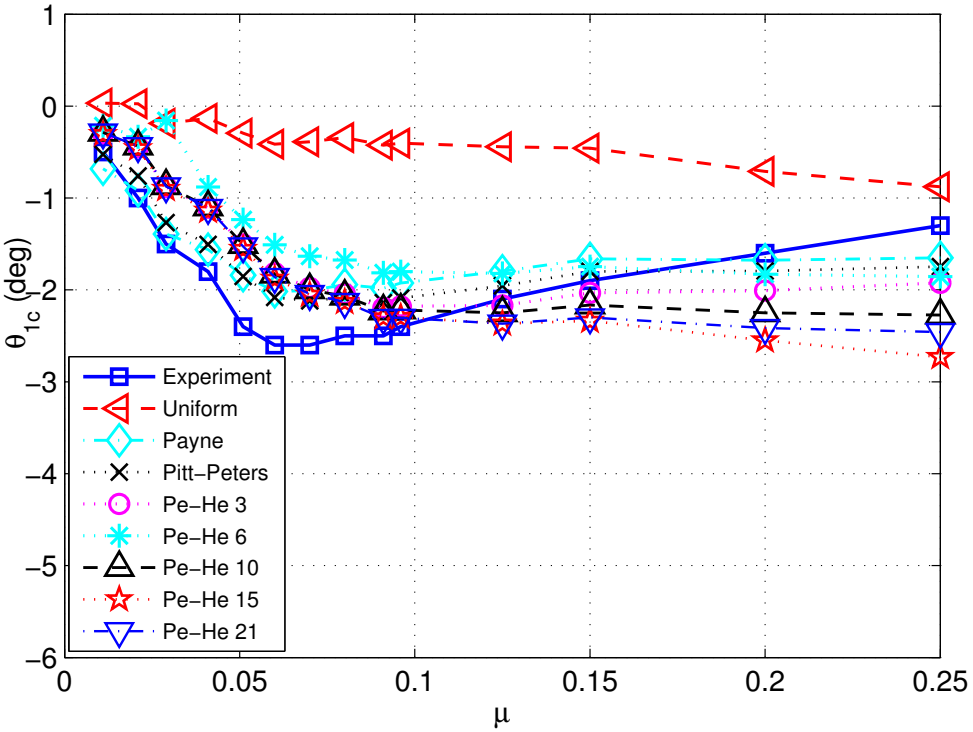

Figure 5.43: Lateral Cyclic Position vs Advance Ratio, at $C_T/\sigma = 0.080$, $\alpha_s = -5°$

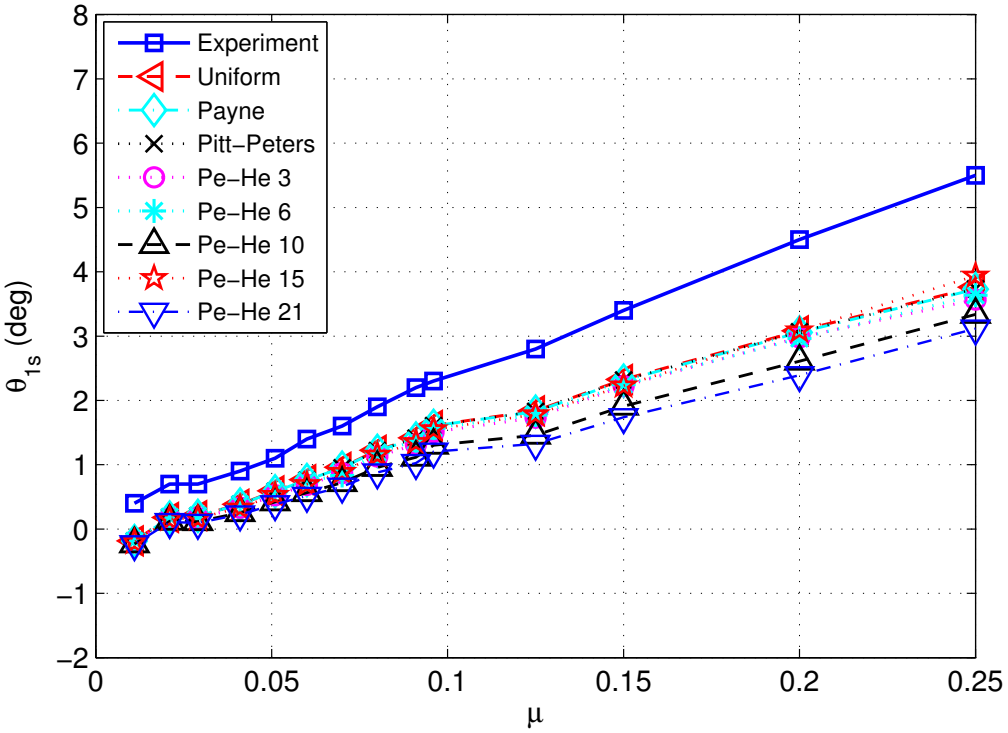

Figure 5.44: Longitudinal Cyclic Position vs Advance Ratio, at $C_T/\sigma = 0.080$, $\alpha_s = -5°$

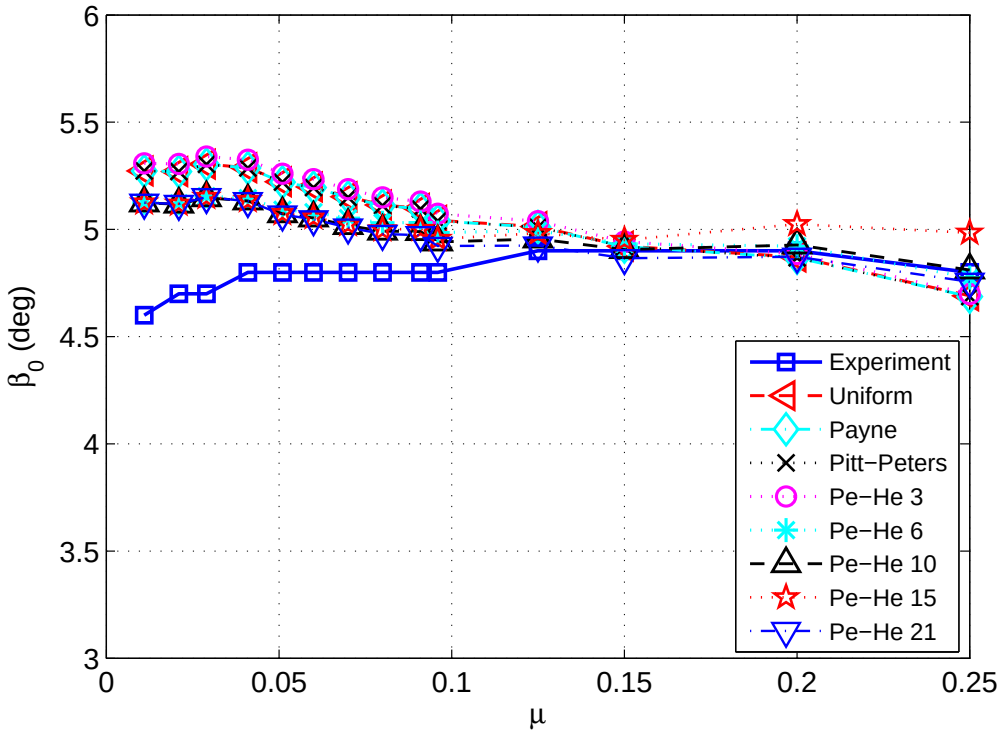

Figure 5.45: Coning Angle vs Advance Ratio, at $C_T/\sigma = 0.080$, $\alpha_s = -5°$

5.4 Observations

- In hover, all inflow models have good correlation with experimental data. Higher state inflow models such as Peters-He 6, 10, 15 and 21-State inflow have radial inflow distributions. These distributions slightly affect the magnitude of angle of attack especially near the blade tip. Although there are some differences in the inflow and angle of attack, performance predictions indicate that all inflow models are almost identical in hovering flight. From the performance evaluation, it is deduced that the effect of the radial shape functions used in Peters-He inflow models are less significant due to symmetry. In both hover case, power, collective pitch, lateral cyclic and longitudinal cyclic blade angles are fairly well estimated.

- In forward flight test cases, predictions have less accuracy than the hover cases. Forward flight tests show that variation of the longitudinal axis play major role in estimating the side force and lateral cyclic position. In the low advance ratio region, prediction of side force and lateral cyclic position of the uniform inflow

is the least accurate. Other models try to follow experimental data in the low advance ratio region. Most of the time, the side force and longitudinal cyclic angles are underestimated. Power, drag force, collective angle, lateral cyclic and coning angle predictions vary with the advance ratio.

- The results in hover usually have good agreement with the data and all models present almost identical results. Therefore, in hover, uniform inflow can be preferred for its simplicity. However, in forward flight the uniform inflow prediction of the side force and lateral cyclic have large errors. Other inflow models exhibit similar results throughout the speed range. Thus, Payne, Pitt-Peters and Peters-He 3-State inflow models can be used for performance calculations in forward flight.

CHAPTER 6

CONCLUSION & RECOMMENDATIONS

6.1 Conclusion

In this thesis, dynamic inflow models commonly used in flight simulations namely uniform inflow, extesion of uniform inflow with Payne's coefficients, Pitt-Peters inflow and Peters-He inflow model with higher harmonics are compared and a fidelity assessment of the inflow models is given. Firstly, predicted induced flow fields on the rotor disk are compared with experimental measurements. Secondly, the effect of the inflow variation on the flapping angle estimations is investigated. Finally, steady-state performance results of the various dynamic inflow models are compared with the wind tunnel tests. From these comparisons, the following conclusions are obtained:

1. Low state inflow models such as Payne, Pitt-Peters and Peters-He 3-State inflow models have only longitudinal inflow variation when trimmed to steady flapping angle.

2. In low state inflow models, selection of the excitation functions greatly affect the inflow variation along with the wake skew angle.

3. Peters-He 6-State inflow model adds additional modes to the low state inflow models and introduces slight lateral inflow variation.

4. In Peters-He inflow models, when inflow state become high enough, the fundamental characteristic of the measured flow is attained.

5. Development of high pressure towards the blade tip negatively affects the con-

vergence of the Peters-He inflow model, thus models with tapered blade configuration have better correlation than the rectangular ones.

6. In low advance ratio flight, lateral flapping angle predictions of uniform inflow model have large modelling errors.

7. An inflow model with a basic longitudinal inflow distribution significantly improves the prediction of the lateral flapping angle and lateral cyclic position.

8. Steady-state lateral and longitudinal flapping angles are dependent on inflow variations along longitudinal and lateral axes, respectively. Here, approximately 90° phase shift is seen between inflow and flapping dynamics.

9. In this study, it is shown that higher state inflow models are not always better than the models with comparatively less state in terms of low advance ratio lateral flapping angle and forward flight steady-state performance estimations, since flapping dynamics are restricted to one-per-revolution frequency. There is only one flapping mode due to rigid blade assumption (elasticity of the blade is neglected) and the solution method depends on harmonic variation. Yet, inflow models with a variation are always better than uniform inflow when the lateral flapping angle is considered.

10. In hover, symmetric flow conditions are applied in azimuthal direction. In the radial direction, velocity becomes larger towards the tip. Since the inflow ultimately depends on the thrust, it becomes symmetric along the azimuthal direction. Differences in inflow are seen in radial direction. However, in hovering flight, symmetric elements on the rotor disk cancel each other and they are reduced to uniform inflow. Thus, radial differences seen in higher state inflow models are insignificant. In hover, all models are almost identical.

11. In forward flight, the dependence on the wake skew angle becomes apparent. Due to phase shift, an inflow variation at least along the longitudinal axis is required for improved estimations along the lateral axis.

    To conclude, the considered inflow models are almost identical in hover. Thus, in hover, uniform inflow can be preferred due to its simplicity in steady-steady performance analysis. In forward flight, longitudinal inflow variation is a must

for capturing the lateral dynamics. The lateral inflow variation is less significant since some portion of the advancing side and retreating side inflow variations are symmetric, thus the effect of the lateral inflow distribution is alleviated.

Moreover, flight mechanics are heavily affected by the one-per-revolution frequency dynamics. Since the coupled blade element model only considers one flapping mode (rigid blade), the rotor tip-path plane dynamics become restricted to this frequency. Therefore, inflow models with higher frequencies (harmonics) are not effective enough in rotor dynamics. In forward flight steady-state estimations, Payne, Pitt-Peters and Peters-He 3-State inflow models can be used when rigid blade flapping is apparent.

6.2 Recommendation for Future Work

The comparison of dynamic inflow models can be extended. Possible recommendations for the future work are listed below:

1. More dynamic inflow flow models can be added to the comparison.
2. Models such as free-wake, vortex-theory, and CFD estimations can be considered. Differences between these models and the dynamic inflow models can be examined. Then, possible corrections to dynamic inflow models can be extracted.
3. Rigid blade flapping solution can be replaced by a elastic blade solution to provide higher frequency coupling between the flapping and inflow.
4. For transient response comparison, dynamic inflow models can be integrated to a full helicopter simulation.

REFERENCES

[1] C. He, *Development and Application of a Generalized Dynamic Wake Theory for Lifting Rotors*. PhD thesis, Georgia Institute of Technology, 1989.

[2] H. Glauert, "An Aerodynamic Theory of the Airscrew," British A. R. C, R & M No. 786, 1922.

[3] H. Glauert, "General Theory of Autogyro," British A. R. C, R & M No. 1111, 1926.

[4] P. Brotherhood and W. Stewart, "An Experimental Investigation of the Flow Through a Helicopter Rotor in Forward Flight," British A. R. C, R & M No. 2734, 1949.

[5] R. P. Coleman, A. M. Feingold, and C. W. Stempin, "Evaluation of Induced Velocity Fields of an Idealized Helicopter Rotor," NASA ARR L5E10, 1945.

[6] J. M. Dress, "A Theory of Airflow Through Rotors and its Application to some Helicopter Problems," *Journal of Helicopter Association of Great Britain*, vol. 3, no. 2, pp. 79–104, 1949.

[7] P. R. Payne, *Helicopter Dynamics and Aerodynamics*. Pitman, 1959.

[8] P. J. Carpenter and B. Friedovich, "Effect of a Rapid Blade Pitch Increase on the Thrust and Induced Velocity Response of a Full Scale Helicopter Rotor," NACA TN 3044, 1953.

[9] G. J. Sissingh, "The Effect of Induced Velocity Variation on Helicopter Rotor Damping in Pitch or Roll," British A. R. C, C.P.No.101 (14,757), 1952.

[10] H. C. J. Curtiss and N. K. Shupe, "Stability and Control Theory for Hingeless Rotors," American Helicopter Society 27th Annual Forum, May 19-21, 1971.

[11] D. Banarjee, S. T. Crews, and K. H. Hohenemser, "Identification of State Variables and Dynamic Inflow from Rotor Model Dynamic Tests," *Journal of American Helicopter Society*, vol. 22, no. 2, 1977.

[12] D. Banarjee, S. T. Crews, and K. H. Hohenemser, "Parameter Identification Applied to Analytic Hingeless Rotor Modeling," *Journal of American Helicopter Society*, vol. 24, no. 1, 1979.

[13] R. A. Ormiston and D. A. Peters, "Hingeless Rotor Response with Nonuniform Inflow and Elastic Blade Bending," *Journal of Aircraft*, vol. 9, no. 10, pp. 730–736, 1972.

[14] D. A. Peters, "Hingeless Rotor Frequency Response with Unsteady Inflow," NASA SP-362, 1974.

[15] D. M. Pitt and D. A. Peters, "Rotor Dynamic Inflow Derivatives and Time Constants from Various Inflow Models," 9th European Rotorcraft Forum, September, 1977.

[16] D. M. Pitt and D. A. Peters, "Theoretical Prediction of Dynamic Inflow Derivatives," *Vertica*, vol. 5, no. 1, 1981.

[17] K. W. Mangler, "Calculation of the Induced Velocity Field of a Rotor," Royal Aircraft Establishment, Report No. Aero 2247, 1948.

[18] D. A. Peters, D. D. Boyd, and C. J. He, "Finite-State Induced-Flow Model for Rotors in Hover and Forward Flight," American Helicopter Society 43th Annual Forum, May 18-20, 1987.

[19] D. A. Peters and C. J. He, "Correlation of Measured Induced Velocities with a Finite-State Wake Model," American Helicopter Society 45th Annual Forum, May 22-24, 1989.

[20] J. A. Morillo and D. A. Peters, "Velocity Field Above a Rotor Disk by a New Dynamic Inflow Model," *Journal of Aircraft*, vol. 39, no. 5, pp. 731–738, 2002.

[21] D. A. Peters, J. A. Morillo, and A. M. Nelson, "New Developments in Dynamic Wake Modeling for Dynamics Applications," *Journal of the American Helicopter Society*, vol. 48, no. 2, pp. 120–127, 2003.

[22] J. W. Elliot and S. L. Althoff, "Inflow Measurement Made with a Laser Velocimeter on a Helicopter Model in Forward Flight: Volume I - Rectangular Planform Blades at an Advance Ratio of 0.15," NASA TM 100541, 1988.

[23] J. W. Elliot and S. L. Althoff, "Inflow Measurement Made with a Laser Velocimeter on a Helicopter Model in Forward Flight: Volume IV - Tapered Planform Blades at an Advance Ratio of 0.15," NASA TM 100544, 1988.

[24] F. D. Harris, "Articulated Rotor Blade Flapping Motion at Low Advance Ratio," *Journal of the American Helicopter Society*, vol. 17, no. 1, pp. 41–48, 1972.

[25] P. M. Shinoda, "Full-Scale S-76 Rotor Performance and Loads at Low Speeds in the NASA Ames 80-by 120-Foot Wind Tunnel," NASA TM 110379, 1996.

[26] J. Seddon, *Basic Helicopter Aerodynamics*. Blackwell Scientific Publications, 1990.

[27] J. Leishman, *Principles of Helicopter Aerodynamics*. Cambridge University Press, 2006.

[28] M. Dreier, *Introduction to Helicopter and Tiltrotor Simulation*. AIAA, 2007.

[29] R. T. N. Chen, "A Survey of Non-uniform Inflow Model for Rotorcraft Flight Dynamics and Control Applications," NASA TM 102219, 1989.

[30] D. M. Pitt, *Rotor Dynamic Inflow Derivatives and Time Constants from Various Inflow Models*. PhD thesis, Washington University, 1980.

[31] D. A. Peters and N. HaQuang, "Dynamics Inflow for Practical Application," *Journal of American Helicopter Society*, vol. 34, no. 4, 1988.

[32] J. J. Howlett, "UH-60A Black Hawk Engineering Simulation Program: Volume I - Mathematical Model," NASA CR 166309, 1981.

[33] W. Johnson, *Rotorcraft Aeromechanics*. Cambridge University Press, 2013.

[34] D. A. Peters, K. B. S., and H. S. Chen, "Calculation of Trim Settings for a Helicopter Rotor by an Optimized Automatic Controller," *Journal of Guidance, Control, and Dynamics*, vol. 7, no. 1, pp. 85–91, 1984.

[35] D. D. Boyd, Jr., *Rotor/Fuselage Unsteady Interactional Aerodynamics: A New Computational Model*. PhD thesis, Virginia Polytechnic Institute and State University, 1999.

[36] A. R. S. Bramwell, G. Done, and D. Balmford, *Bramwell's Helicopter Dynamics*. Butterworth-Heinemann, 2001.

[37] Q. K. Nguyen, "Dynamic Analysis of Rotor Blade Undergoing Rotor Power Shutdown," NASA TM 102865, 1990.

[38] D. Jepson, R. Moffitt, K. Hilzinger, and J. Bissel, "Analysis and Correlation of Test Data From an Advanced Technology Rotor System," NASA CR 3714, 1983.

[39] P. M. Shinoda and W. Johnson, "Performance Results From a Test of an S-76 Rotor in the Nasa Ames 80-by 120-Foot Wind Tunnel," Paper AIAA-93-3414, 11th Applied Aerodynamic Conference, August 1993.

APPENDIX A

MAIN ROTOR BLADE GEOMETRIES

In this part, geometry of the main rotor blades used in Chapters 3 and 5 are given. In Chapter 3, rectangular and tapered blades are used [23]. In Chapter 5, the S-76 advanced main rotor blade is used [38]. For this blade, twist and chord distributions are also given.

A.1 Rectangular Blade Geometry

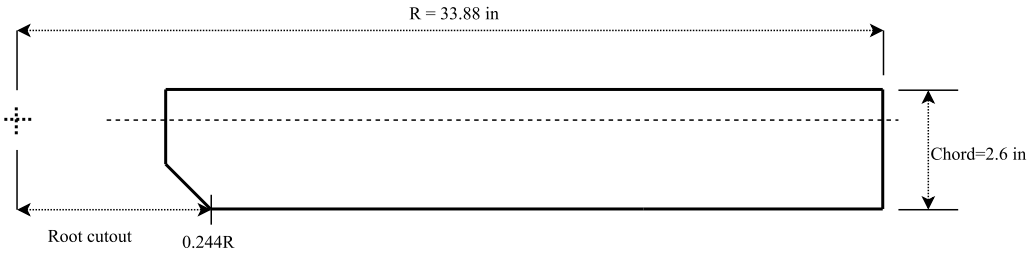

Figure A.1: 2-D View of the Rectangular Blade

A.2 Tapered Blade Geometry

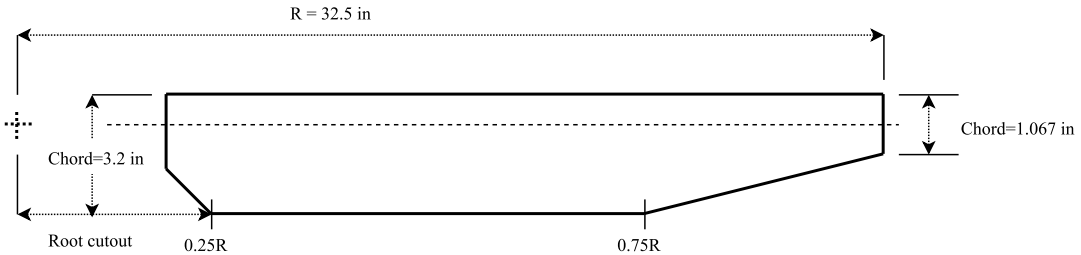

Figure A.2: 2-D View of the Tapered Blade

A.3 S-76 Main Rotor Blade Geometry

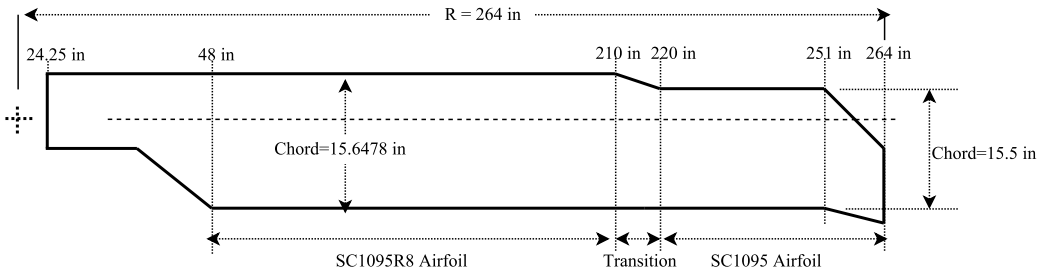

Figure A.3: 2-D View of the S-76 Main Rotor Blade

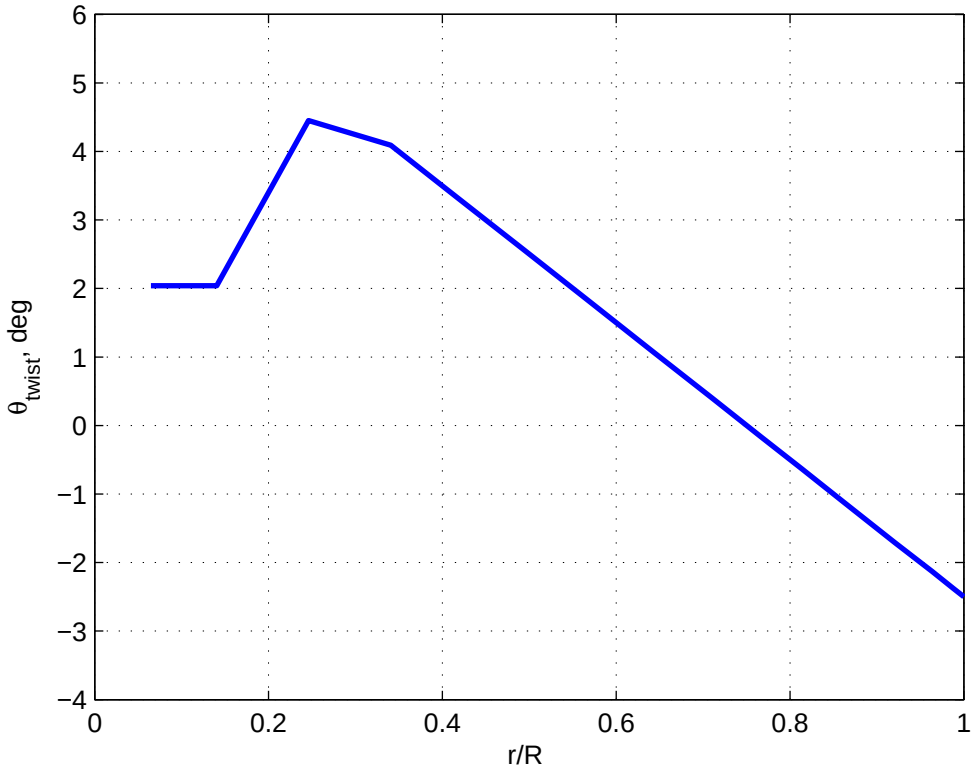

Figure A.4: S-76 Main Rotor Blade Twist Distribution

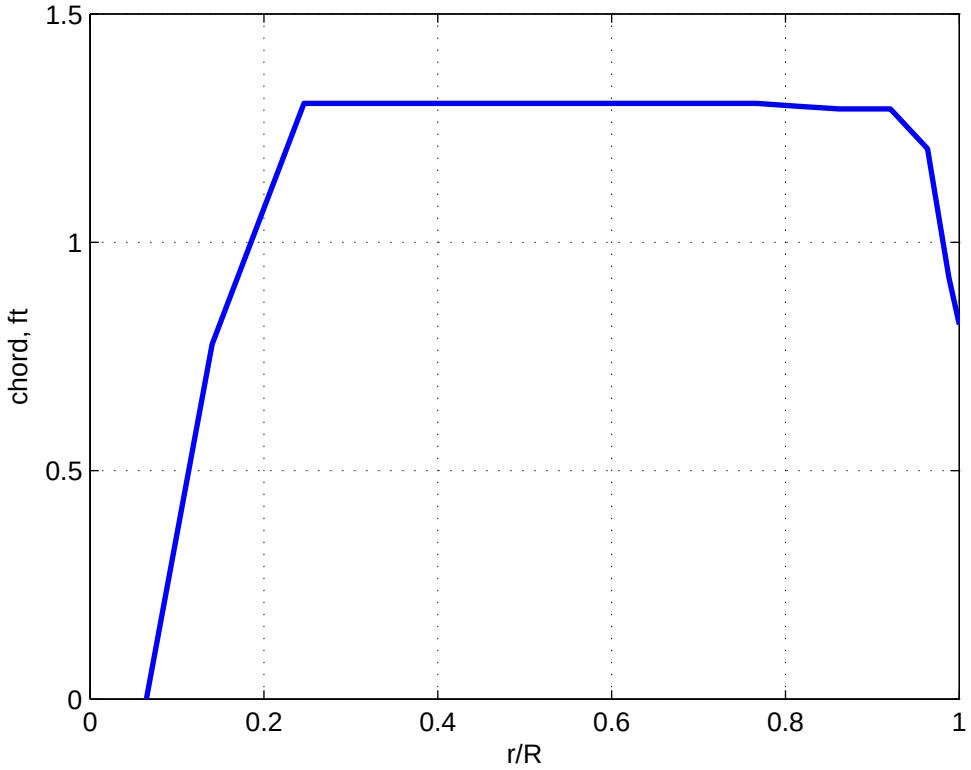

Figure A.5: S-76 Main Rotor Blade Chord Distribution

APPENDIX B

AIRFOIL CHARACTERISTICS OF THE S-76 MAIN ROTOR BLADE

The S-76 main rotor blade airfoils aerodynamic lift and drag coefficients are given in this part. The data is taken from the [38]. In order to have 2-D tables, the data structure is modified.

B.1 SC1095 Airfoil

Table B.1: 2-D Lift Coefficient Data of the SC1095 Airfoil

Mach #/ A.o.A	0	0.3	0.4	0.5	0.6	0.7	0.75	0.8	0.9	1	2
-180	0.000	0.000	0.000	0.000	0.000	0.000	0.000	0.000	0.000	0.000	0.000
-172	0.780	0.780	0.780	0.780	0.780	0.780	0.780	0.780	0.780	0.780	0.780
-160	0.640	0.640	0.640	0.640	0.640	0.640	0.640	0.640	0.640	0.640	0.640
-150	0.950	0.950	0.950	0.950	0.950	0.950	0.950	0.950	0.950	0.950	0.950
-30	-1.000	-1.000	-1.000	-1.000	-1.000	-1.000	-1.000	-0.950	-0.950	-0.950	-0.950
-15	-0.910	-0.910	-0.685	-0.790	-0.655	-0.745	-0.790	-0.809	-0.740	-0.710	-0.710
-10	-0.880	-0.880	-0.580	-0.720	-0.540	-0.660	-0.720	-0.810	-0.740	-0.630	-0.630
-8	-0.760	-0.760	-0.640	-0.720	-0.590	-0.713	-0.725	-0.750	-0.702	-0.623	-0.623
-6	-0.600	-0.600	-0.580	-0.613	-0.609	-0.740	-0.730	-0.690	-0.663	-0.615	-0.615
-5	-0.500	-0.500	-0.520	-0.520	-0.580	-0.720	-0.720	-0.580	-0.575	-0.521	-0.521
-3	-0.300	-0.300	-0.327	-0.477	-0.354	-0.516	-0.517	-0.360	-0.398	-0.334	-0.334
0	0.041	0.041	0.041	-0.038	0.075	-0.263	0.066	0.070	-0.150	-0.050	-0.050
2	0.269	0.269	0.286	0.255	0.361	-0.094	0.478	0.350	0.133	0.200	0.200
4	0.496	0.496	0.531	0.547	0.647	0.075	0.704	0.560	0.390	0.449	0.449
6	0.723	0.723	0.776	0.840	0.860	0.830	0.745	0.705	0.640	0.700	0.700
8	0.951	0.951	1.021	1.027	0.910	0.870	0.786	0.805	0.765	0.806	0.806
9	1.065	1.065	1.124	1.072	0.930	0.890	0.807	0.840	0.788	0.828	0.828
10	1.157	1.157	1.182	1.078	0.950	0.913	0.827	0.842	0.810	0.850	0.850
12	1.200	1.200	1.138	1.049	1.006	0.960	0.868	0.845	0.829	0.865	0.865
15	1.015	1.015	0.992	0.982	1.090	1.030	0.930	0.850	0.858	0.888	0.888
30	1.000	1.000	1.000	1.000	1.000	1.000	1.000	1.000	1.000	1.000	1.000
150	-0.950	-0.950	-0.950	-0.950	-0.950	-0.950	-0.950	-0.950	-0.950	-0.950	-0.950
156	-0.700	-0.700	-0.700	-0.700	-0.700	-0.700	-0.700	-0.700	-0.700	-0.700	-0.700
158	-0.660	-0.660	-0.660	-0.660	-0.660	-0.660	-0.660	-0.660	-0.660	-0.660	-0.660
160	-0.640	-0.640	-0.640	-0.640	-0.640	-0.640	-0.640	-0.640	-0.640	-0.640	-0.640
172	-0.780	-0.780	-0.780	-0.780	-0.780	-0.780	-0.780	-0.780	-0.780	-0.780	-0.780
180	0.000	0.000	0.000	0.000	0.000	0.000	0.000	0.000	0.000	0.000	0.000

Table B.2: 2-D Drag Coefficient Data of the SC1095 Airfoil

Mach #/ A.o.A	**0**	**0.3**	**0.4**	**0.5**	**0.6**	**0.7**	**0.75**	**0.8**	**0.9**	**1**	**2**
-180	0.020	0.020	0.020	0.020	0.020	0.020	0.020	0.020	0.020	0.020	0.020
-179	0.025	0.025	0.025	0.025	0.025	0.025	0.025	0.025	0.025	0.025	0.025
-175	0.065	0.065	0.065	0.065	0.065	0.065	0.065	0.065	0.065	0.065	0.065
-172	0.110	0.110	0.110	0.110	0.110	0.110	0.110	0.110	0.110	0.110	0.110
-150	0.642	0.642	0.642	0.642	0.642	0.642	0.642	0.642	0.642	0.642	0.642
-115	1.880	1.880	1.880	1.880	1.880	1.880	1.880	1.880	1.880	1.880	1.880
-90	2.080	2.080	2.080	2.080	2.080	2.080	2.080	2.080	2.080	2.080	2.080
-65	1.880	1.880	1.880	1.880	1.880	1.880	1.880	1.880	1.880	1.880	1.880
-30	0.630	0.630	0.630	0.630	0.630	0.630	0.630	0.630	0.630	0.630	0.630
-10	0.210	0.210	0.215	0.015	0.016	0.210	0.185	0.225	0.262	0.297	0.297
-9	0.102	0.102	0.160	0.033	0.026	0.182	0.162	0.193	0.233	0.273	0.273
-8	0.042	0.042	0.104	0.050	0.036	0.153	0.139	0.160	0.203	0.248	0.248
-7	0.018	0.018	0.050	0.035	0.036	0.125	0.117	0.130	0.176	0.225	0.225
-6	0.011	0.011	0.022	0.023	0.036	0.096	0.094	0.100	0.149	0.202	0.202
-5	0.009	0.009	0.012	0.011	0.026	0.068	0.071	0.083	0.132	0.177	0.177
-4	0.009	0.009	0.009	0.009	0.014	0.039	0.048	0.065	0.115	0.152	0.152
-3	0.008	0.008	0.008	0.008	0.011	0.020	0.027	0.042	0.091	0.135	0.135
-1	0.009	0.009	0.008	0.008	0.008	0.009	0.011	0.025	0.060	0.104	0.104
0	0.008	0.008	0.008	0.008	0.008	0.008	0.009	0.017	0.050	0.090	0.090
1	0.009	0.009	0.008	0.008	0.008	0.009	0.011	0.025	0.060	0.104	0.104
2	0.009	0.009	0.008	0.008	0.009	0.010	0.023	0.040	0.080	0.118	0.118
3	0.009	0.009	0.008	0.009	0.010	0.020	0.045	0.065	0.100	0.135	0.135
4	0.010	0.010	0.008	0.009	0.012	0.044	0.068	0.090	0.120	0.153	0.153
5	0.011	0.011	0.009	0.011	0.021	0.068	0.091	0.109	0.144	0.178	0.178
6	0.014	0.014	0.011	0.014	0.040	0.092	0.114	0.128	0.167	0.203	0.203
7	0.019	0.019	0.012	0.020	0.065	0.116	0.137	0.149	0.189	0.226	0.226
8	0.037	0.037	0.014	0.030	0.086	0.140	0.160	0.170	0.210	0.249	0.249
9	0.100	0.100	0.017	0.055	0.106	0.164	0.183	0.198	0.236	0.274	0.274
10	0.210	0.210	0.024	0.090	0.126	0.188	0.206	0.225	0.262	0.298	0.298
15	0.315	0.315	0.222	0.240	0.227	0.308	0.320	0.343	0.374	0.408	0.376
30	0.630	0.630	0.630	0.630	0.630	0.630	0.630	0.630	0.630	0.630	0.630
65	1.880	1.880	1.880	1.880	1.880	1.880	1.880	1.880	1.880	1.880	1.880
90	2.080	2.080	2.080	2.080	2.080	2.080	2.080	2.080	2.080	2.080	2.080
150	0.640	0.640	0.640	0.640	0.640	0.640	0.640	0.640	0.640	0.640	0.640
172	0.110	0.110	0.110	0.110	0.110	0.110	0.110	0.110	0.110	0.110	0.110
175	0.065	0.065	0.065	0.065	0.065	0.065	0.065	0.065	0.065	0.065	0.065
179	0.025	0.025	0.025	0.025	0.025	0.025	0.025	0.025	0.025	0.025	0.025
180	0.020	0.020	0.020	0.020	0.020	0.020	0.020	0.020	0.020	0.020	0.020

B.2 SC1095-R8 Airfoil

Table B.3: 2-D Lift Coefficient Data of the SC1095-R8 Airfoil

Mach # /A.o.A	0	0.3	0.4	0.5	0.6	0.7	0.75	0.8	0.9	1	2
-180	0.000	0.000	0.000	0.000	0.000	0.000	0.000	0.000	0.000	0.000	0.000
-172	0.780	0.780	0.780	0.780	0.780	0.780	0.780	0.780	0.780	0.780	0.780
-160	0.640	0.640	0.640	0.640	0.640	0.640	0.640	0.640	0.640	0.640	0.640
-150	0.556	0.556	0.556	0.556	0.556	0.556	0.556	0.556	0.556	0.556	0.556
-30	-1.000	-1.000	-1.000	-1.000	-1.000	-1.000	-1.000	-0.950	-0.950	-0.950	-0.950
-15	-0.850	-0.850	-0.805	-0.700	-0.700	-0.700	-0.775	-0.809	-0.740	-0.710	-0.710
-10	-0.800	-0.800	-0.740	-0.600	-0.600	-0.600	-0.700	-0.810	-0.670	-0.630	-0.630
-8	-0.744	-0.744	-0.684	-0.656	-0.600	-0.600	-0.700	-0.750	-0.667	-0.623	-0.623
-6	-0.534	-0.534	-0.545	-0.560	-0.580	-0.592	-0.694	-0.690	-0.663	-0.615	-0.615
-5	-0.440	-0.440	-0.450	-0.470	-0.500	-0.550	-0.650	-0.580	-0.575	-0.521	-0.521
-3	-0.204	-0.204	-0.202	-0.215	-0.240	-0.310	-0.380	-0.360	-0.398	-0.334	-0.334
0	0.150	0.150	0.171	0.166	0.140	0.200	0.241	0.070	-0.150	-0.050	-0.050
2	0.386	0.386	0.419	0.421	0.453	0.570	0.630	0.350	0.138	0.200	0.200
4	0.622	0.622	0.668	0.675	0.750	0.810	0.740	0.560	0.390	0.449	0.449
6	0.852	0.852	0.916	0.930	0.900	0.866	0.800	0.705	0.640	0.700	0.700
8	1.076	1.076	1.150	1.040	0.937	0.898	0.845	0.805	0.765	0.806	0.806
9	1.188	1.188	1.220	1.060	0.954	0.914	0.860	0.840	0.788	0.828	0.828
10	1.300	1.300	1.270	1.080	0.971	0.926	0.875	0.842	0.810	0.850	0.850
12	1.440	1.440	1.130	1.110	1.006	0.948	0.905	0.845	0.829	0.865	0.865
15	1.263	1.263	1.125	1.110	1.070	0.980	0.950	0.850	0.858	0.888	0.888
30	1.000	1.000	1.000	1.000	1.000	1.000	1.000	1.000	1.000	1.000	1.000
150	-0.950	-0.950	-0.950	-0.950	-0.950	-0.950	-0.950	-0.950	-0.950	-0.950	-0.950
156	-0.700	-0.700	-0.700	-0.700	-0.700	-0.700	-0.700	-0.700	-0.700	-0.700	-0.700
158	-0.660	-0.660	-0.660	-0.660	-0.660	-0.660	-0.660	-0.660	-0.660	-0.660	-0.660
160	-0.640	-0.640	-0.640	-0.640	-0.640	-0.640	-0.640	-0.640	-0.640	-0.640	-0.640
172	-0.780	-0.780	-0.780	-0.780	-0.780	-0.780	-0.780	-0.780	-0.780	-0.780	-0.780
180	0.000	0.000	0.000	0.000	0.000	0.000	0.000	0.000	0.000	0.000	0.000

Table B.4: 2-D Drag Coefficient Data of the SC1095-R8 Airfoil

Mach # /A.o.A	**0**	**0.3**	**0.4**	**0.5**	**0.6**	**0.7**	**0.75**	**0.8**	**0.9**	**1**	**2**
-180	0.020	0.020	0.020	0.020	0.020	0.020	0.020	0.020	0.020	0.020	0.020
-179	0.025	0.025	0.025	0.025	0.025	0.025	0.025	0.025	0.025	0.025	0.025
-175	0.065	0.065	0.065	0.065	0.065	0.065	0.065	0.065	0.065	0.065	0.065
-172	0.110	0.110	0.110	0.110	0.110	0.110	0.110	0.110	0.110	0.110	0.110
-150	0.642	0.642	0.642	0.642	0.642	0.642	0.642	0.642	0.642	0.642	0.642
-115	1.880	1.880	1.880	1.880	1.880	1.880	1.880	1.880	1.880	1.880	1.880
-90	1.880	1.880	1.880	1.880	1.880	1.880	1.880	1.880	1.880	1.880	1.880
-65	1.880	1.880	1.880	1.880	1.880	1.880	1.880	1.880	1.880	1.880	1.880
-30	0.630	0.630	0.630	0.630	0.630	0.630	0.630	0.630	0.630	0.630	0.630
-10	0.250	0.250	0.260	0.270	0.288	0.310	0.326	0.225	0.262	0.297	0.297
-9	0.195	0.195	0.207	0.215	0.213	0.258	0.273	0.198	0.236	0.273	0.273
-8	0.141	0.141	0.154	0.161	0.137	0.207	0.221	0.170	0.210	0.248	0.248
-7	0.086	0.086	0.101	0.106	0.109	0.155	0.168	0.146	0.187	0.225	0.225
-6	0.050	0.050	0.062	0.070	0.081	0.094	0.109	0.122	0.163	0.202	0.202
-5	0.031	0.031	0.034	0.038	0.045	0.060	0.085	0.099	0.139	0.177	0.177
-4	0.018	0.018	0.013	0.024	0.025	0.044	0.060	0.075	0.115	0.152	0.152
-3	0.011	0.011	0.010	0.015	0.017	0.027	0.035	0.042	0.091	0.135	0.135
-1	0.010	0.010	0.008	0.009	0.009	0.010	0.012	0.026	0.063	0.109	0.109
0	0.009	0.009	0.008	0.008	0.008	0.010	0.014	0.025	0.060	0.100	0.100
1	0.009	0.009	0.008	0.008	0.008	0.012	0.024	0.042	0.078	0.118	0.118
2	0.010	0.010	0.009	0.008	0.010	0.025	0.048	0.070	0.100	0.136	0.136
3	0.010	0.010	0.009	0.009	0.016	0.048	0.071	0.089	0.119	0.153	0.153
4	0.010	0.010	0.010	0.010	0.025	0.070	0.095	0.108	0.138	0.170	0.170
5	0.011	0.011	0.010	0.011	0.038	0.093	0.115	0.128	0.160	0.193	0.193
6	0.011	0.011	0.011	0.018	0.060	0.115	0.134	0.148	0.182	0.215	0.215
7	0.012	0.012	0.013	0.027	0.086	0.138	0.152	0.167	0.202	0.235	0.235
8	0.012	0.012	0.015	0.044	0.112	0.160	0.173	0.185	0.221	0.255	0.255
9	0.013	0.013	0.018	0.078	0.137	0.183	0.195	0.208	0.242	0.277	0.277
10	0.014	0.014	0.027	0.111	0.163	0.206	0.218	0.230	0.262	0.298	0.298
15	0.114	0.114	0.230	0.280	0.300	0.320	0.330	0.343	0.374	0.408	0.390
30	0.630	0.630	0.630	0.630	0.630	0.630	0.630	0.630	0.630	0.630	0.630
65	1.880	1.880	1.880	1.880	1.880	1.880	1.880	1.880	1.880	1.880	1.880
90	1.516	1.516	1.516	1.516	1.516	1.516	1.516	1.516	1.516	1.516	1.516
150	0.642	0.642	0.642	0.642	0.642	0.642	0.642	0.642	0.642	0.642	0.642
172	0.110	0.110	0.110	0.110	0.110	0.110	0.110	0.110	0.110	0.110	0.110
175	0.065	0.065	0.065	0.065	0.065	0.065	0.065	0.065	0.065	0.065	0.065
179	0.029	0.029	0.029	0.029	0.029	0.029	0.029	0.029	0.029	0.029	0.029
180	0.020	0.020	0.020	0.020	0.020	0.020	0.020	0.020	0.020	0.020	0.020